

University of Warwick institutional repository: <http://go.warwick.ac.uk/wrap>

A Thesis Submitted for the Degree of PhD at the University of Warwick

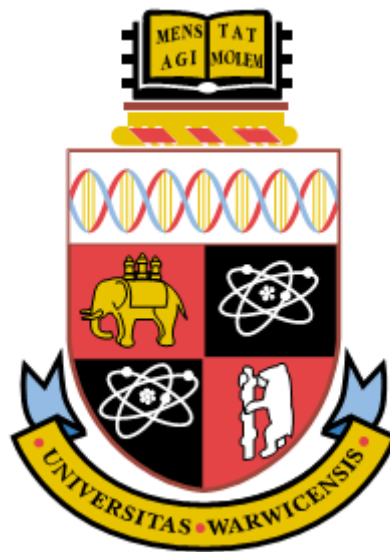
<http://go.warwick.ac.uk/wrap/67680>

This thesis is made available online and is protected by original copyright.

Please scroll down to view the document itself.

Please refer to the repository record for this item for information to help you to cite it. Our policy information is available from the repository home page.

Study on the characterization of mechanical properties of viscoelastic-plastic materials by nanoindentation



By

Lei Wang

A thesis submitted in partial fulfillment of the requirements
for the degree of Doctor of Philosophy in Engineering

School of Engineering, University of Warwick

December 2014

Abstract

The aim of this PhD work is to develop a novel and effective instrument to characterize the mechanical properties of viscoelastic material. The principle of this system is based on nanoindentation technique, which is widely used in recent years to explore the mechanical properties of various materials. However, quite a few studies demonstrated that the determination of mechanical properties of viscoelastic material by using the standard Oliver Pharr method would lead to incorrect results.

Based on this issue, a new improved tribological probe microscopy (TPM) system was established to carry out the investigation of mechanical properties of viscoelastic materials. Materials including polytetrafluoroethylene (PTFE), styrene rubber and nitrile rubber were measured under quasi-static mode of nanoindentation. The inaccurate results proved that static indentation analyzed by the Oliver Pharr method is not suitable for current work. In addition, dynamic indentation was performed to measure these samples. The results demonstrated that it is a good approach to explore time-dependent properties of polymer samples. The dynamic method offers more abundant viscous information.

Moreover, another measurement function was added in this facility to perform creep nanoindentation on viscoelastic samples. It enables to generate instant and infinite modulus as well as time constant. The comparison between the results obtained by

dynamic and creep indentation reveals that the more physical element should be considered to bridge the gap between these two approaches.

Extra works focus on the relationship between surface topography and its mechanical properties. Finite element simulation as well as actual experiments were performed to investigate the tilt effect on the results of mechanical properties. The results revealed that the standard Oliver Pharr method underestimated the contact area, which will result in overestimating the hardness and elastic modulus of engineering materials.

Above all, this study proved the ability of our home made facility to further explore the viscoelastic material. More importantly, it will pave a new way for the investigation of the relationship between the surface topography and viscous property of soft matter including various biomaterials in the near future.

Declaration

This thesis is presented in accordance with the regulations for the degree of Doctor of Philosophy by the High Degree Committee at the University of Warwick.

The thesis has been composed and written by myself based on my original work guided by PhD supervisor. Information derived from the published or unpublished work of others has been acknowledged in the text and a list of references is given. This thesis has not been submitted in any previous application for a higher degree.

Signature

.....

Date

.....

Acknowledgements

First of all, I wish to express my best gratitude to my supervisor Dr. Xianping Liu for the continuous support of my PhD study and research over the years, for her patience, motivation, enthusiasm, and immense knowledge. Without her encouragement and guidance throughout my studies, I would not have been able to produce this piece of work.

Thanks go to all the members of the Metrology Laboratory in the School of Engineering, University of Warwick for the daily support and advice. Special thanks to Mr. Dave Robinson, Mr. Martin Davis and Mr. Frank Courtney for their skillful technical supports.

Finally, I would like to thank my family members, including my parents and especially my wife for her general support, patience and understanding during the period of my PhD life.

Publications arising from this work

Journals

- Lei Wang and Xianping Liu. (2014). Characterization of viscoelastic materials by quasi-static and dynamic indentation, *Measurement Science and Technology*, 25, 064017.
- Lei Wang and Xianping Liu. Correlation analysis of surface tilt effect on its mechanical properties by nanoindentation, (Under revision with *Precision Engineering*).
- Lei Wang and Xianping Liu. Characterization of viscoelastic materials based on spherical indentation of creep-load control by Tribological Probe Microscopy, (Submitted to *Wear*).

Conferences

- Lei Wang and Xianping Liu. Characterization of viscoelastic materials by quasi-static and dynamic indentation. The 11th International Symposium on Measurement Technology and Intelligent Instruments. Aachen, Germany. July 2013.
- Lei Wang and Xianping Liu. The comparison of measurement of mechanical properties of viscoelastic material by dynamic and creep nano-indentation with

spherical tip. The 4th International Conference on Manipulation, Manufacturing and Measurement on the Nanoscale. Taipei. Taiwan. October 2014.

Table of contents

Abstract	I
Declaration	III
Acknowledgements	IV
Publications arising from this work	V
Table of contents	VII
List of figures	XIII
List of tables	XVIII
List of Symbols	XIX
Chapter 1 Introduction	1
1.1 State of the problem	1
1.2 Materials background	3
1.3 Nanoindentation background.....	7
1.4 Aim and objectives	9
1.5 Thesis structure.....	9
Chapter 2 Literature Review	12

2.1 Nanoindentation	12
2.1.1 Nanoindentation procedures	12
2.1.2 Indenter geometry	16
2.1.3 Frame compliance	21
2.1.4 Pile-up and sink-in behaviour	22
2.1.5 Load function	24
2.2 Elastic and plastic contact	26
2.2.1 Elastic contact	26
2.2.2 Elastic-plastic deformation	28
2.3 Instrumentation for indentation experiment	30
2.3.1 Instrumented indentation testing facility (nanoindenter)	30
2.3.2 Atomic force microscopy	33
2.4 Viscoelastic contacts	36
2.4.1 Viscoelastic material	36
2.4.2 Viscoelastic mechanics	37
2.4.3 Viscoelastic models	38
2.5 Summary	42
Chapter 3 An improved home-made facility for characterizing the mechanical properties of viscoelastic materials	43

3.1 Introduction	43
3.2 Designed details of improved system for mechanical properties of viscoelastic material study	44
3.2.1 Scheme of the system	44
3.2.2 Design details of the sensing probe	47
3.2.3 Indenter tip selection.....	49
3.2.4 Voltage-controlled current (U-I) driver	50
3.2.5 Operating software.....	53
3.3 Calibration of TPM system	55
3.3.1 Calibration the capacitive sensor	55
3.3.2 Calibration of force actuator	56
3.3.3 Calibration of cross beam cantilever stiffness	57
3.3.4 Natural frequency of the cross beam	58
3.4 Quasi-static nanoindentation of the viscoelastic materials.....	59
3.4.1 Material and method	60
3.4.2 Results and discussion	61
3.5 Summary	64
Chapter 4 Dynamic nanoindentation to characterize the mechanical properties of viscoelastic materials	66

4.1 Introduction	66
4.2 Theory	67
4.3 Experiment Method	72
4.4 Results and discussions	75
4.5 Summary	78
Chapter 5 Characterization of viscoelastic materials based on spherical indentation of creep-load control.....	80
5.1 Introduction	80
5.2 Theoretical approach of creep indentation	83
5.3 Experiment and materials	88
5.4 Results	90
5.5 Discussions	97
5.6 Summary	101
Chapter 6 Correlation analysis of surface tilt effect on its mechanical properties by nano-indentation.....	103
6.1 Introduction	103
6.2 Error sources of nano-indentation	105
6.3 Geometry study of related Berkovich tip	109
6.4 Nano-indentation on tilt sample	113

6.4.1 Finite element simulation.....	113
6.4.2 Nano-indentation experiment on fused silica sample	115
6.5 Nano-indentation on the sample with sinusoidal surface	116
6.5.1 Finite element simulation.....	116
6.5.2 Experiment on standard sinusoidal specimen	117
6.6 Result and discussions	118
6.7 Summary	127
Chapter 7 Conclusions and recommendations for further work	129
7.1 Conclusions	129
7.2 Recommendations for future work	131
References	133
Appendices	145
Appendix A Matlab program.....	145
A1 Hardness calculation	145
A2 Lag phase angle calculation	150
A3 Tilt angle effect	150
A4 Power spectrum density	152
Appendix B Abaqus .inp file	153
B1 Flat surface 0 degree simulation	153

B2 Sinusoidal surface 0 degree simulation.....	161
Appendix C Labview Program for creep indentation	171

List of figures

Figure 1.1 Rough equivalent hardness conversion chart for various standard hardness tests to Berkovich hardness	4
Figure 1.2 Uniaxial tension testing geometry (left) original sample; (right) stretched sample.	5
Figure 1.3 Uniaxial stress-strain curves for loading and unloading of three material types: (a) linear elastic, (b) nonlinear elastic, and (c) nonlinear, inelastic	5
Figure 1.4 Uniaxial stress-strain response of aluminum under tensile test. The response is initially linear with the slope of the elastic modulus (E) but transitions to a plastic deformation.....	7
Figure 1.5 Mechanical characterization of the relevant length scales involved in mechanical testing and the types of testing available	8
Figure 2.1 Force – displacement curve obtained from an indentation test on metal. ...	13
Figure 2.2 Schematic representation of a section through the peak of a conical indent with relevant quantities labeled.....	14
Figure 2.3 Schematic demonstrations of cylindrical, spherical and conical or pyramidal indenter geometries.	17
Figure 2.4 Schematic illustrating the concept of effective indenter shape resulting from the pressure distribution under the indenter	18
Figure 2.5 Schematic of a) an elastic and b) an elastic-plastic spherical indentation ..	19
Figure 2.6 Surface contours and plastic zones predicted FEM for materials with different values of E_r / σ_y . Non-work hardening materials ($\eta = 0$) are	

represented by solid lines h_f / h_{\max} and work-hardening materials ($\eta = 10\sigma_y$) by broken lines	23
Figure 2.7 Schematic showing the definition of plastic, elastic and total work of indentation.....	24
Figure 2.8 Applied force-time profiles for (a) a simple load-unload cycle under triangular loading, (b) a trapezoidal load-hold-unload profile in which creep can be measured during the holding period, and (c) exponential loading.	25
Figure 2.9 Load-displacement (P-h) curve of perfectly elastic (Hertzian) contact on glass	27
Figure 2.10 Elastic-plastic indentation responses for a sphere on fused silica glass and aluminium	29
Figure 2.11 Schematic of an instrumented indentation testing apparatus. The spring and tip comprise a probe. An indenter environment imposes and measures load, displacement to the system.	32
Figure 2.12 Schematic demonstration of an AFM contact testing apparatus. The cantilever spring and tip comprise a probe, which together with a sample test surface comprise a simple mechanical thermodynamic system.....	34
Figure 2.13 AFM cantilever deflection is not linear over a wide range of operating voltages	36
Figure 2.14 Viscoelastic models: (a) Kelvin Model; (b) Maxwell Model.	38
Figure 2.15 The creep and relaxation of Kelvin model	39
Figure 2.16 The creep and relaxation of Maxwell model	40
Figure 2.17 Three-parameter model.....	41
Figure 2.18 Creep phase (a) and relaxation phase (b) of three-parameter model	42
Figure 3.1 Schematic of TPM system.	45

Figure 3.2 Photo of TPM system.	45
Figure 3.3 Schematic of mechanical probe.	47
Figure 3.4 Schematic diagram of magnet-coil force actuator	48
Figure 3.5 Circuit scheme of Voltage-controlled current driver	51
Figure 3.6 PCB circuit of voltage-current driver.	52
Figure 3.7 The voltage-current drive calibration.	53
Figure 3.8 Front panel and block diagram of Labview program.	55
Figure 3.9 Calibration of cross beam cantilever.....	56
Figure 3.10 Calibration of force actuator.	57
Figure 3.11 Calibration the cross beam cantilever stiffness.....	58
Figure 3.12 The vibration displacement of the cross beam.	59
Figure 3.13 Frequency spectrum of the vibration response.	59
Figure 3.14 P-h curves obtained in quasi-static indentation (a) PTFE (b) polystyrene (c) Nitrile rubber.....	62
Figure 3.15 Load size effect of quasi-static indentation	64
Figure 4.1 Simple-harmonic oscillator model.....	69
Figure 4.2 Model accommodates both instrument and sample in contact	71
Figure 4.3 The phase angle as a function of frequency, measured with indenter tip hanging in free space.....	73
Figure 4.4 Dynamic stiffness and damping of indentation system as a function of frequency measured in free space	74
Figure 4.5 The displacement and force modulation in dynamic indentation.....	75
Figure 4.6 Storage and loss modulus as a function of frequency (a) PTFE (b) Styrene rubber (c) Nitrile Rubber.....	77
Figure 4.7 Loss factor as a function of frequency.....	78

Figure 5.1 Schematic of Voigt model.....	86
Figure 5.2 The schematic of TPM system.....	89
Figure 5.3 The displacement-depth curve of PTFE under creep indentation.....	90
Figure 5.4 Creep experiment data curve fitting for PTFE under different peak load. ..	92
Figure 5.5 Creep experiment data curve fitting for styrene rubber under different peak load.....	94
Figure 5.6 The value of E_0 and E_∞ of PTFE as a function of peak load level.	96
Figure 5.7 The value of E_0 and E_∞ of styrene rubber as a function of peak load level.....	97
Figure 5.8 The ratio E_∞ and E_0 of two samples as a function of peak load level. ..	97
Figure 6.1 Geometry model of Berkovich tip	110
Figure 6.2 Percentage errors of projected area for Berkovich tip as the function of tilt angle range between -1 to 1 degree.....	111
Figure 6.3 Percentage errors of projected area for Berkovich tip as the function of tilt angle range between -2 to 2 degree.....	112
Figure 6.4 Percentage errors of projected area for Berkovich tip as the function of tilt angle range between -3 to 3 degree.....	112
Figure 6.5 Percentage errors of projected area for Berkovich tip as the function of tilt angle range between -4 to 4 degree.....	113
Figure 6.6 Percentage errors of projected area for Berkovich tip as the function of tilt angle range between -5 to 5 degree.....	113
Figure 6.7 Model of tilt indentation on a flat sample in FEA.....	114
Figure 6.8 Mesh of the indentation sample.....	115
Figure 6.9 FEM simulation of indentation on a sinusoidal surface sample.	117

Figure 6.10 FEA simulation result of P-h curves under different tilted degree.	118
Figure 6.11 P-h curves of nano-indentation experiment on the fused silica sample...	119
Figure 6.12 The variation of the contact area due to tilting by both O-P method and FEA simulation.	121
Figure 6.13 Comparison of E and H values from FEA and O-P method at different tilt angles.....	121
Figure 6.14 P-h curves obtained at different position of the sinusoidal surface from FEA as illustrated in Figure 6.9: (a) Positions 1 to 4; (b) Positions 4 to 7.....	123
Figure 6.15 Comparison of E and H obtained by the O-P method and FEA correction for indentation at different positions of a sinusoidal surface.	124
Figure 6.16 Mapping results of mechanical properties by TPM: (a) topography; (b) hardness; (c) elastic modulus.	125
Figure 6.17 Averaged topography, hardness before and after correction for the sinusoidal sample.	126

List of tables

Table 2-1 Geometry parameter for indenters used in indentation	16
Table 3-1 Parameters of magnetic coil.....	49
Table 5-1 Viscoelastic parameter of PTFE.....	95
Table 5-2 Viscoelastic parameter of styrene rubber	95
Table 5-3 The comparison of the storage and loss modulus of PTFE.....	99
Table 5-4 The comparison of the storage and loss modulus of styrene rubber	100
Table 6-1 Surface parameters of sinusoidal sample measured by WYKO and TPM .	124

List of Symbols

A_0	Contact area
a	Radius of projected area
a_1	Internal radius of the coil
a_2	External radius of the coil
b	Half length of the diagonal line
C_F	Frame compliance
C_S	Sample compliance
C_T	Total compliance
D	Damping
D_i	Damping from capacitive plate
D_c	Contact damping
E	Elastic modulus
E'	Storage modulus
E''	Loss modulus
E_i	Elastic modulus of indenter
E_0	Instantaneous modulus
E_∞	Infinite modulus
E_r	Reduced modulus
F	Force
G	Shear modulus

H	Hardness
h	Depth
h_c	Contact depth
h_e	Penetration depth for elastic deformation
h_f	Residual depth
h_{\max}	Maximum depth
I	Current
J	Creep compliance
k	Stiffness
K_i	Spring stiffness
K_c	Contact stiffness
l	Length
l_0	Original length
Δl	Change of length
m	Mass
m_i	Mass of indenter
P	Force
R	Radius
R_i	Radius of spherical tip
S	Contact stiffness
t	Time
t_R	Rising time
U_{in}	Input voltage

U_{out}	Output voltage
W_p	Plastic work
W_{total}	Total work of indentation
W_u	Elastic recovery work
z	Displacement
ε	Strain
ε_i	Strain rate
ε_x	Axial strain
ε_y	Transverse strain
η	Viscosity coefficient
ν	Poisson ratio
σ	Stress
σ_y	Yield stress
τ	Time constant
φ	Contact angle
ϕ	Phase angle
Φ	Function of creep compliance
ψ	Function of relaxation
ω	Frequency

Chapter 1 Introduction

1.1 State of the problem

The traditional techniques for characterizing the mechanical properties are tension or compression, bending or cyclic tests [1]. Commonly, they have the following features. First of all, the dimensions of the specimens are macro-scale at least several millimeters [2]. Secondly, the resolution of the applied force is in millinewton range. In addition, the measurements are time consuming because the test automation is limited [3]. In contrast, the industrial development and research in this area prefers to miniaturization and automation. Therefore, characterization of the material in the sub-millimeter range is necessary. The mechanical properties play a vital part in the product performance and their lifetime, not only in engineering components, but also for the functional parts for medical or biological applications [4-6]. Moreover, the investigation of the mechanical properties of thin films is essential for electronic products [7]. With the development in the industrial of viscoelastic materials, which exhibit an important application in many fields. For instance, viscoelastic materials are widely used in the automotive and aerospace industries to reduce the noise and vibration level [8]. In addition, some polymers are widely used in the medical applications to act as bone cements [9]. Consequently, there is obvious motivation to investigate their mechanical properties under different conditions which may result in failure incidents.

The mechanical properties of the material can be determined by the means of nano indentation, which has become more and more popular in recent years due to its miniaturization, automation and convenience [10]. This technique commonly examines the material at sub-micrometre scale. The general principle of this method is a small tip pressed into the surface of the specimen [11]. The applied force and depth of penetration are recorded continuously and simultaneously. Based on the relationship between the force and displacement recorded, the mechanical properties of the sample can be calculated. This technique has successfully studied the mechanical behavior of a variety of different engineering materials [12-14]. Some of the studies are beyond the capability of conventional tools. Bedoui et al [15] studied the phenomenon of force discontinues in the crystalline polymers by nanoindentation. A standard developed by Karapanagiotis was able to predict the defects on thin polystyrene films on silicon substrate via nanoindentation [16]. In recent years, there is a growing interest in the implementation of the nanoindentation technique in soft matter [17]. The investigation of this type of material is not feasible on the macro scale instrument.

However, most commercial nanoindentation instruments are still designed for stiff material and by using these facilities the results of soft material are not accurate and reliable [18]. As a consequence, it is imperative and necessary to put the effort in the area of development the technique for viscoelastic materials.

In the last decade, Metrology Lab in the University of Warwick has developed a unique Tribological Probe Microscopy (TPM), which is designed as a low-cost, multifunction facility used for characterizing the surface properties, such as friction,

elastic modulus, nanohardness and topography, for traditional hard samples [19]. It has successfully investigated the mechanical properties of metals and ceramics [20]. In addition, the application of this facility was transferred to the interior surface panel of car to explore the potential relationship between the surface properties and customers' preferences [21]. However, it is a challenge when facing the viscoelastic sample to characterize their properties by the original facility of TPM.

1.2 Materials background

The first hardness measurement was performed by Mohs in 1812 by scratching various minerals to other soft mineral samples to observe the impression at the macroscale [22]. Nowadays, the technique has been further developed to use the miniaturized automatic system to probe to sample at nanoscale. During this period quite a few standard tests have been claimed and developed use in the industrial and research (Figure 1.1). The hardness test is a motivating force to characterize the mechanical properties of the materials

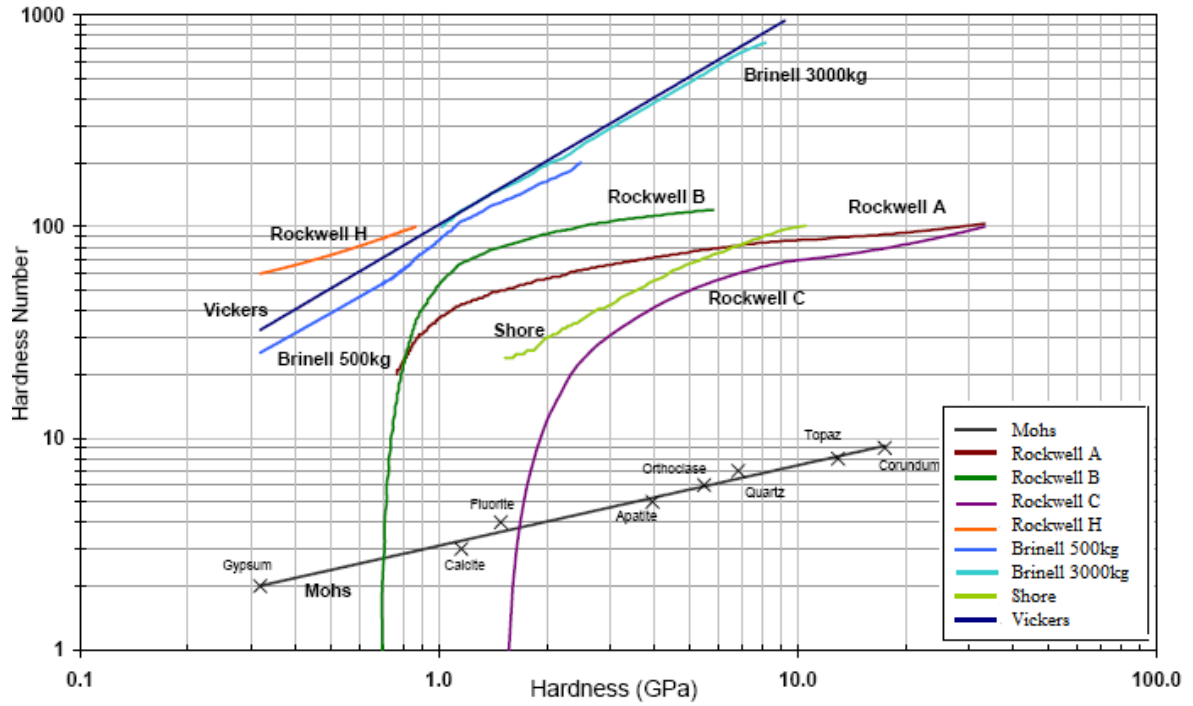


Figure 1.1 Rough equivalent hardness conversion chart for various standard hardness tests to Berkovich hardness [23].

The engineering mechanics is related to the study of the response of materials to applied load. The most common and simple test is a dog bone shape tensile test. The fundamental parameters used in this study are stressed σ , and strain ε :

$$\sigma = \frac{P}{A_0} \quad (1-1)$$

$$\varepsilon = \frac{\Delta l}{l_0} \quad (1-2)$$

where P is the applied force, A_0 is the cross section area, l_0 is the original length of the specimen (Figure 1.2). The change of the length is $\Delta l = l - l_0$.

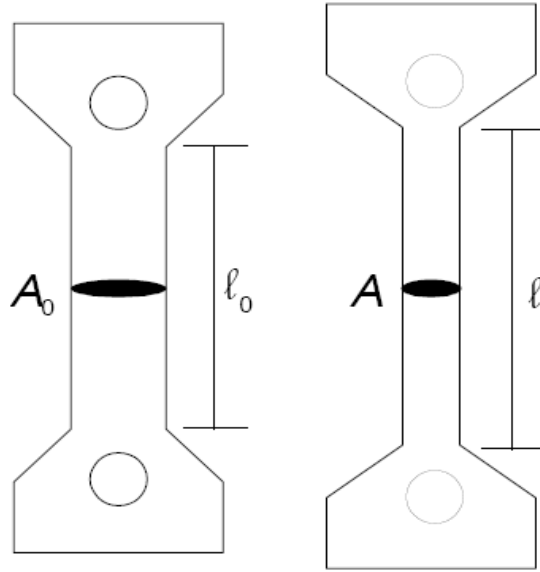


Figure 1.2 Uniaxial tension testing geometry (left) original sample; (right) stretched sample.

The fundamental response of the material under applied force is elastic. The different elastic responses are shown in Figure 1.3. The slope of linear relationship is elastic modulus. The stiffness (k) is the slope of the force displacement curve and depends on the elastic modulus, $k = EA / l_0$.

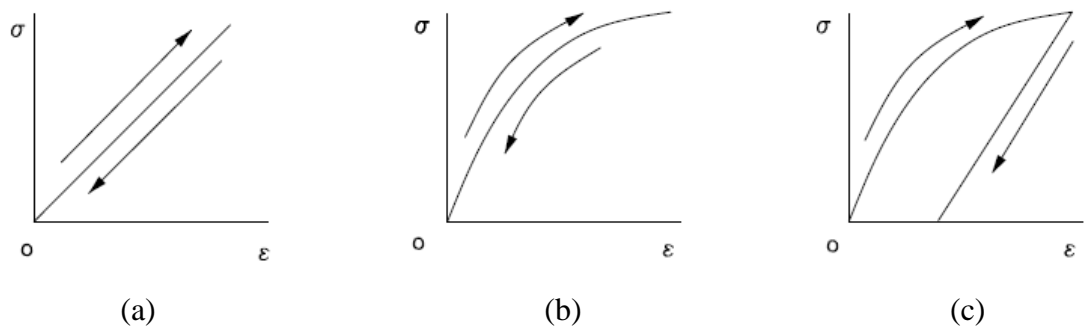


Figure 1.3 Uniaxial stress-strain curves for loading and unloading of three material types: (a) linear elastic, (b) nonlinear elastic, and (c) nonlinear, inelastic [24].

A homogeneous material can be described by two parameters, elastic modulus E and Poisson ratio ν , which represents the degree of transverse contraction under an axial strain ε_x , therefore

$$\nu = -\frac{\varepsilon_y}{\varepsilon_x} \quad (1-3)$$

where ε_y is the transverse strain. The direction of these two strains is opposite, thus the value of Poisson rate is positive between 0 and 0.5 for most solid materials. The elastic property is time-independent.

After an initial stage of linear elastic deformation, there is an exhibition of permanent deformation observed in the tensile experiment, which is shown in Figure 1.4. Generally, the elastic deformation range of metal is very small at 1%, while the permanent deformation is larger, which is named plastic. Plastic property is commonly time-independent as well.

The behavior of viscoelastic material is different from previous examples. Polymers are typical viscoelastic material, which exhibits time dependent deformation. The detailed description for this property will be presented in Chapter 2. Here is a brief illustration to time-dependant behavior. The plastic deformation is irreversible with permanent deformation of the sample, while the viscoelastic deformation is reversible.

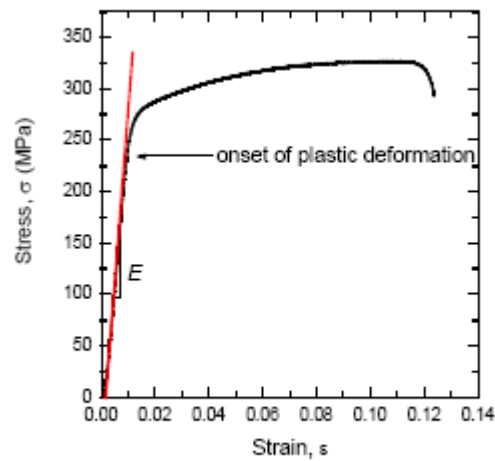


Figure 1.4 Uniaxial stress-strain response of aluminum under tensile test. The response is initially linear with the slope of the elastic modulus (E) but transitions to a plastic deformation.

1.3 Nanoindentation background

There has been a growing interest in the characterization of mechanical properties of instrumental probing systems in recent two decades. The length scale of different techniques is varied from micro to atomic, which are shown in Figure 1.5.

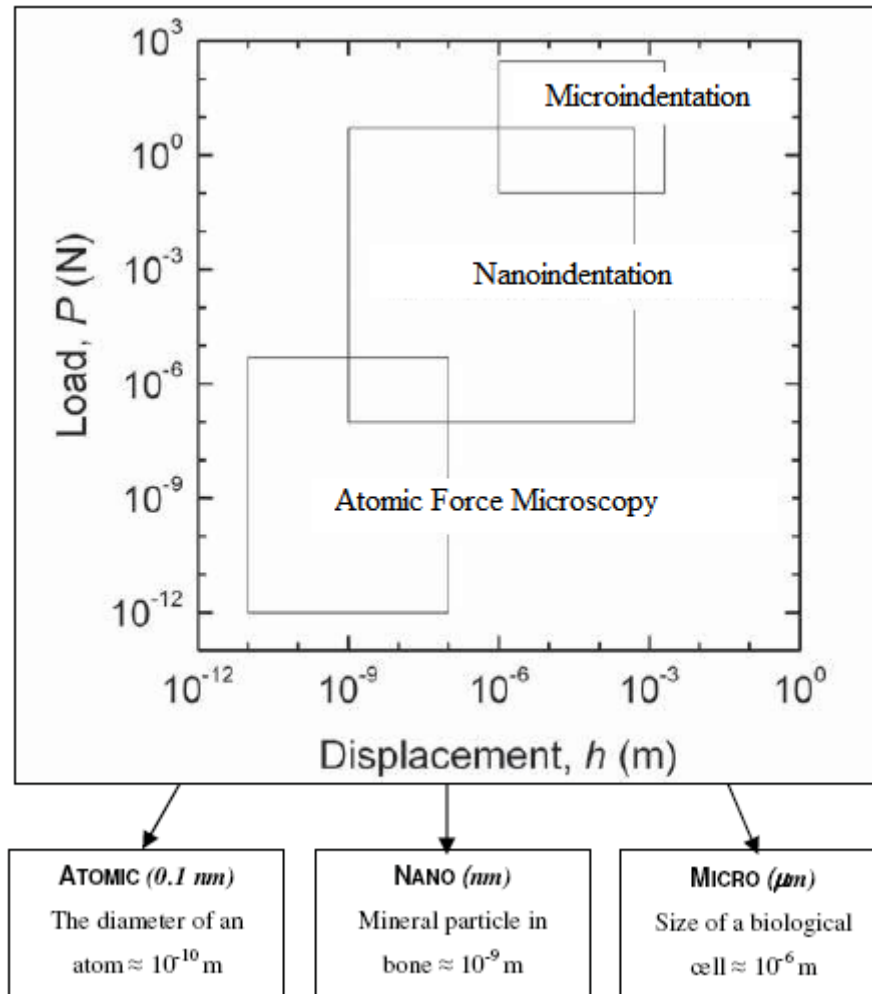


Figure 1.5 Mechanical characterization of the relevant length scales involved in mechanical testing and the types of testing available [25].

Among them, nanoindentation is recognized as a leading method to characterize the engineering material. It has the capability of investigate the mechanical properties of engineering materials and thin film coating samples. In addition, it is an emerging technique for the study of biological and biomimetic materials. The traditional tensile test only obtains the average value of mechanical properties over a whole range of the sample. In contrast, the nanoindentation method is able to examine the local information on mechanical behaviour. Other advantages of a nanoindentation

technique are that it is suitable for thin-film and small volume sample, which is not applicable under tensile test. In addition, nanoindentation technique is also suitable for investigating the heterogeneity in natural materials and mapping the local information of mechanical properties at small scale. More detailed about this technique will be reviewed in Chapter 2.

1.4 Aim and objectives

The aim of this work is developing a homemade facility to characterize the mechanical properties of viscoelastic materials. Under this aim, several objectives are generated within the project. First of all, it is necessary to redevelop the original facility, TPM, which can be used in this project. Based on that, the establishment work of the system demonstrates a new generation of facility for studying and exploring soft matters. Second objective is adding new test options onto TPM system and make it suitable for viscoelastic materials. These test options include dynamic method and creep method. Another objective is investigating the relationship between surface topography and mechanical properties.

1.5 Thesis structure

This thesis consists of seven chapters and each chapter is divided into several different sections, which are listed in the table of contents. The first chapter begins with the state of the problem in the characterization of mechanical properties of viscoelastic materials. In addition, a brief introduction about the material mechanics and nanoindentation background are mentioned. Moreover, the roadmap of this thesis

is shown in chapter one as well.

The second chapter is the literature review of this thesis. It focuses on the nanoindentation technique and solid contact mechanics. More importantly, the reviewed of instrumentation including nanoindentation and the AFM is demonstrated here followed by the theory of viscoelastic contact.

Chapters 3 to 6 are the main part of this thesis and demonstrate details of the experiment, results and discussions. In Chapter 3, a unique system exclusively for characterizing the viscoelastic properties is developed. The establishment and calibration of this system are included as well. In addition, quasi-static indentation was performed on viscoelastic sample. While the results revealed that traditional Oliver-Pharr method is not suitable for this type of sample.

In Chapter 4, dynamic nanoindentation was performed to measure the viscoelastic properties of material based on the system mentioned in Chapter 3. The experimentation results show that dynamic nanoindentation is a suitable technique for exploring the time dependent properties of these materials. It is an experiment evidence that this system is able to extend its application for elastic-plastic samples to viscoelastic ones.

Chapter 5 focuses on another method to obtain the viscoelastic properties compared to dynamic indentation. It was performed by creep indentation at constant load after a ramp loading profile to derive the instant and infinite elastic modulus of the sample. The results from creep method can be converted to complex modulus, which are available for the comparison to the dynamic results. The comparison between them

indicated that it is necessary to establish a more complex model to fill the gap between these two methods.

In Chapter 6, the work focuses on the effect of tilt angle on the results of nanoindentation on stiff sample. It comprises geometry studies, finite element simulation work and experiment studies. Flat and sinusoidal samples are applied in the simulation and actual experiment. The relationship between the surface topography and its mechanical properties is discussed.

The last chapter summarizes the conclusions of this research work as well as presents the recommendation for future research topics in this area.

Chapter 2 Literature Review

2.1 Nanoindentation

2.1.1 Nanoindentation procedures

The nanoindentation technique is performed under the applied force from micro to millinewton range, with the penetration depth at the scale of nanometre to micrometer [26]. Generally, a relative hard tip is used to probe the specimen. Figure 2.1 shows a typical force displacement (P-h) curve for nanoindentation experiment on metal. This curve is different from the stress-strain curve obtained from a tensile test, which can be used to derive the mechanical properties straightforward [27]. This is due to the loading part of the loading - displacement curve, includes elastic and plastic deformation mechanisms. It is important to note that the unloading part of the curve comprises mainly pure elastic recovery. It is not uncommon to observe deviation phenomenon such as pop-in or pop-out displacement in some types of materials including aluminium and silicon [28, 29]. The mechanical properties such as hardness and elastic mechanical properties can be determined by analysis of unloading part of the curve.

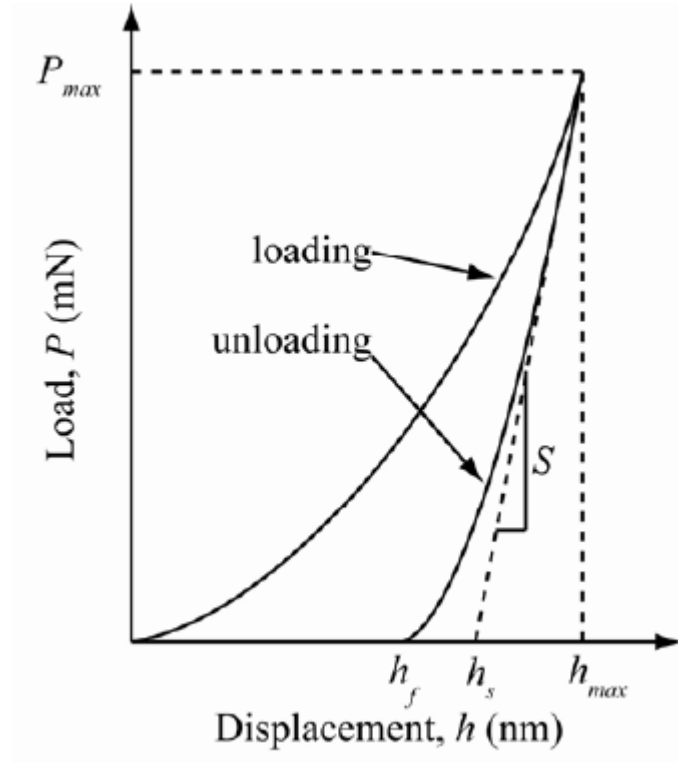


Figure 2.1 Force – displacement curve obtained from an indentation test on metal.

There are a variety of analyses used for explaining the force-displacement curve obtained in nanoindentation experiment [30, 31]. Among of them, the most widely used method was raised by Oliver and Pharr [31]. This method works well to determine the hardness and elastic modulus for different samples. It is built on the foundation on a power law relation as below:

$$P = l(h - h_f)^m \quad (2-1)$$

The derivative of P , dP/dh , is the stiffness of the elastic contact S , which can be calculated at the maximum load and depth (P_{\max} and h_{\max}). When the indenter is a flat end tip, the contact stiffness can be used to work out the surface displacement directly, which is demonstrated in Figure 2.1. If the tip is a pyramid or spherical profile, the calculation of h_s has to be adjusted by a correction factor β to interpret

the effect of different geometry.

$$h_{\max} - h_s = \beta \frac{P_{\max}}{S} \quad (2-2)$$

The value of β is between 0.72 to 0.75. Detail information about the value of β for different type of tip is listed in Table 2.1 in section 2.1.2. If there is no phenomenon of sink in and pile up, the relationship between the maximum depth and the contact depth can express as:

$$h_{\max} = h_c + h_s \quad (2-3)$$

The schematic illustration of conical indentation is demonstrated in Figure 2.2.

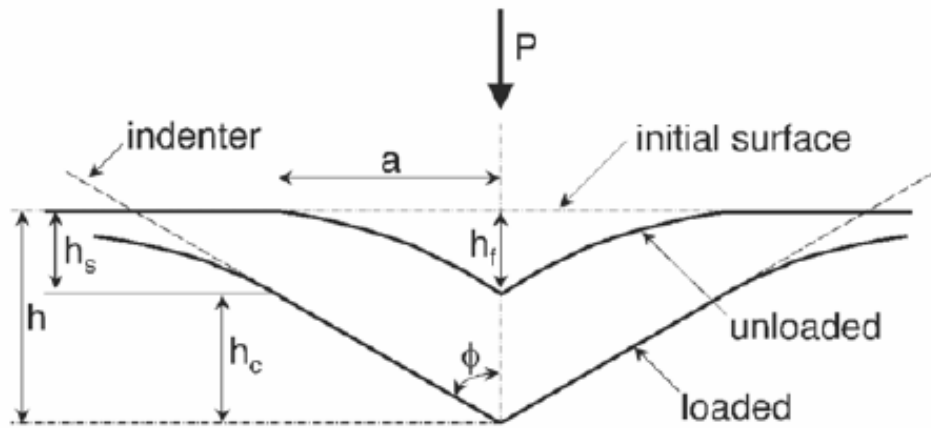


Figure 2.2 Schematic representation of a section through the peak of a conical indent with relevant quantities labeled.

The projected area depends on the geometry of the tip when the contact depth is constant.

$$A = F(h_c) \quad (2-4)$$

Where F is the function between projected area and the penetration depth. The definition of projected area is the cross section area of the tip, which has a physical

relationship to the stress induced through the indentation. Consequently, the projected area is commonly used rather than the surface area in contact.

These functions for different types of indenters have well-defined. In addition, it is common to use this function to calculate the projected area. The results are more reliable in large depth indentation, while the variation of the result is inevitable due to the manufacture of indenter. Therefore, it is important to determine the shape function for each indenter prior to the experiment.

The definition of hardness is the ratio between the applied load and the corresponding support project contact area.

$$H = \frac{P}{A} \quad (2-5)$$

The hardness value is dependent on other properties including work hardening parameter and yield strength. When it comes to the elastic modulus of the sample, it requires further consideration. Although the commonly used tip is made of diamond, it is not perfectly rigid without being deformed, especially measuring extremely hard specimen. Therefore, it is reasonable to account for the deformation of the tip; the term ‘reduce’ modulus is defined as

$$E_r = \frac{1-\nu^2}{E} + \frac{1-\nu_i^2}{E_i} \quad (2-6)$$

The reduced modulus can be calculated by contact stiffness and the projected area:

$$E_r = \frac{\sqrt{\pi}}{2\gamma} \frac{S}{\sqrt{A}} \quad (2-7)$$

Another factor γ is introduced here, which is due to the axial variation in stress induced by non-axisymmetric. The values of γ for different types of indenter can be

found in Table 2.1.

2.1.2 Indenter geometry

There are various types of indenter used in indentation. Among them, Brinell spherical, Rockwell conospherical and Vicker pyramid are often used in macro-indentation [32]. In addition, for micro and nano-scale indentation, Berkovich tip and cube corner indenter are more suitable due to they can be made extremely sharp. The parameter of these indenters are shown in Table 2-1.

Table 2-1 Geometry parameter for indenters used in indentation [33].

Indenter tip	Projected Area	Face angle	Equivalent Cone Angle	Intercept Factor, β	Correction Factor, γ
Sphere	$\pi(2Rh_c - h_c^2)$	-	-	0.75	1
Cone	$\pi h_c \tan(\varphi)^2$	φ	φ	0.72	1
Berkovich	$24.562h_c^2$	65.3°	70.32°	0.75	1.05
Cube Corner	$2.598h_c^2$	35.26°	42.28°	0.75	1.034
Vickers	$24.504h_c^2$	68°	70.2996°	0.75	1.012
Knoop	$65.438h_c^2$	86.25° & 65°	-	0.75	1.012

Pyramidal indenters are often modelled as conical ones with an equivalent angle in order to simplify the calculation. In nano-scale indentation, spherical tip is commonly manufactured as a conospheroids. There is a maximum depth of this type of tip to be calculated as a spherical one.

The geometry of the probe plays an essential role in the deformation profiles in the indentation experiments. There are different types of tips used for indentation. The geometry of popular used types of tip is shown in Figure 2.3. The cylindrical tip with a flat end is convenient to use because of its cross area is constant, which simplified the analysis process [34]. While there can be induced stress concentration along the edge of the tip. It is important to acknowledge that in the small scale nanoindentation experiment, it is difficult to align the flat surface and parallel to the sample surface. Consequently, other types of probes (spherical, conical or pyramid) are much more widely used in small scale testing rather than flat one.

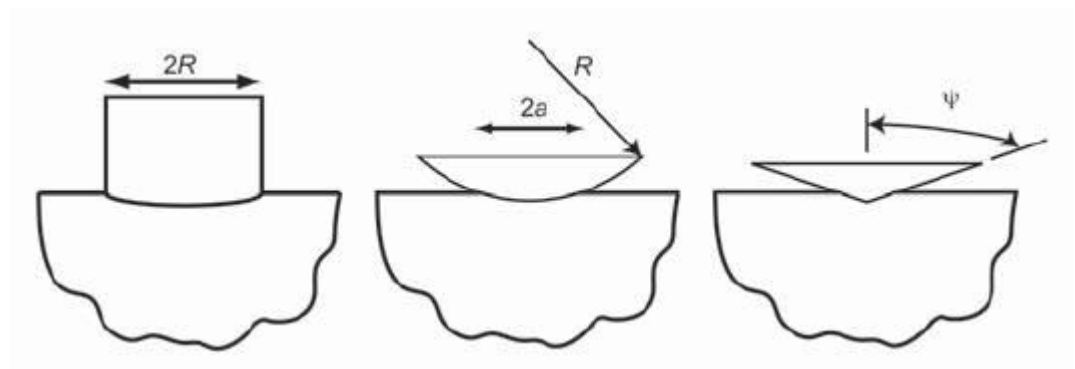


Figure 2.3 Schematic demonstrations of cylindrical, spherical and conical or pyramidal indenter geometries.

The benefits of spherical indenter are that they are always pure elastic deformation at the beginning stage of indentation, while the pyramid or conical one exhibit different phenomenon that plastic and elastic deformation occur immediately after the contact even at the small depth indentation [35]. The advantage of conical or pyramid tip is that there is no obvious depth-size effect, which indicates the deformation profile at large force can be scaled down equals to small force indentation. However, the

relationship between the applied load and displacement is not linear when using spherical or conical tips [36]. The linear function is obvious in the homogeneous tensile test and indentation experiment with flat tip. The contact area between the spherical or conical tips changes with the probe pressed into the sample.

In spherical nanoindentation, the strain field is normally uniform and radially symmetric. The conical and pyramidal indentation can be thought as a special condition of spherical indentation. In the beginning stage of indentation using a sharp Berkovich tip equals to using a cone spherical indentation with an infinite radius tip. The contact area against the depth of penetration for Berkovich tip and cone spherical tip with different radius is shown in Figure 2.4. It reveals that Berkovich tip equals to conospherical tip with the increasing depth.

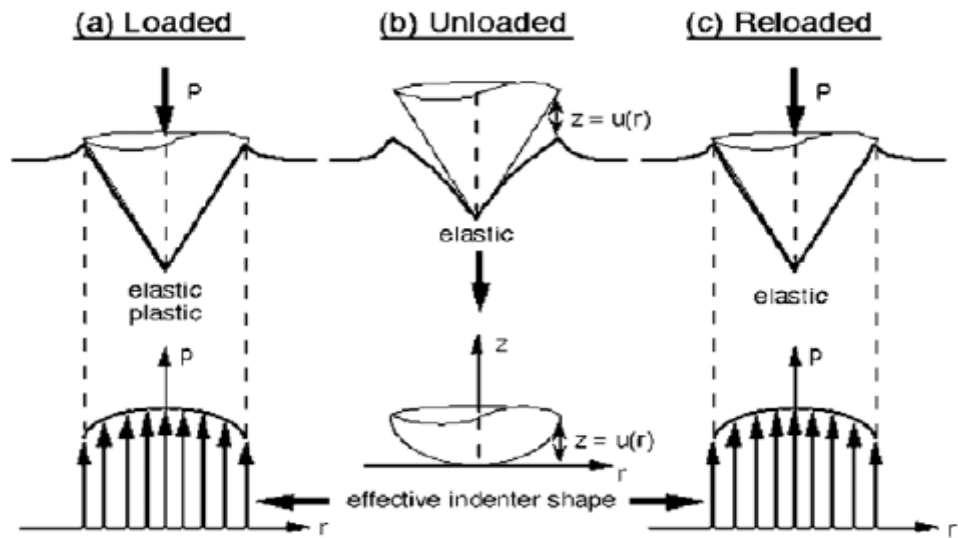


Figure 2.4 Schematic illustrating the concept of effective indenter shape resulting from the pressure distribution under the indenter [37].

Traditionally, spherical tip was more commonly used due to its convenience to

analysis. When the research interests moved to the scale of micro- and nano-indentation, pyramid type of tip was more frequently used, since its effectiveness in a small range of scale and easy to manufacture. The available of cone-spherical tip can be made with a radius at around 100nm. The analysis of nanoindentation is based on Hertz Equation:

$$P = \frac{3}{4} E_r R^{1/2} h_e^{3/2} \quad (2-8)$$

where R is the radius, P is the applied force, E_r is reduced modulus and h_e is the displacement of elastic deformation. The schematic illustration of spherical indentation is shown in Figure 2.5.

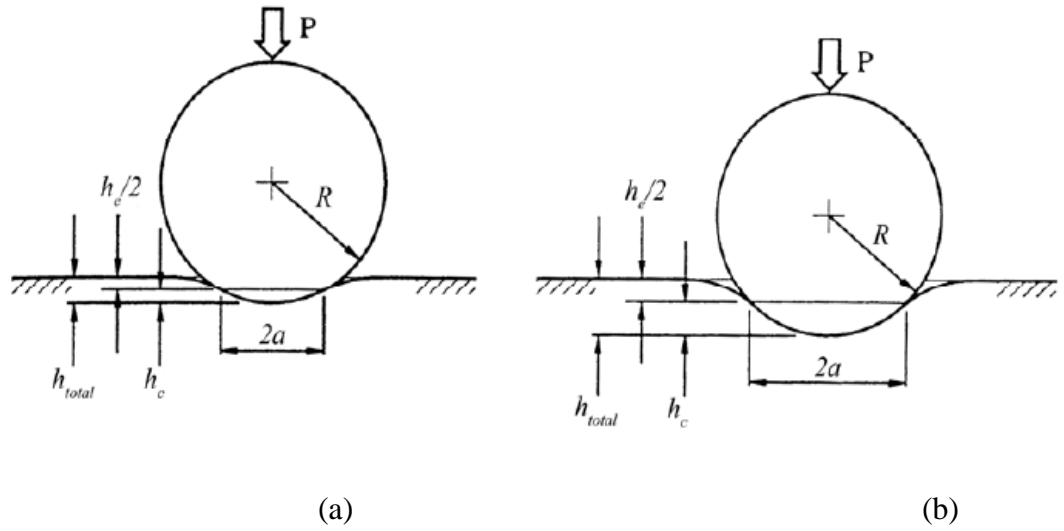


Figure 2.5 Schematic of a) an elastic and b) an elastic-plastic spherical indentation [30].

For the elastic deformation condition, there is no impression left after unloading the applied force, Sneddon claimed that [38]

$$h_e = h_{total} = \frac{a^2}{R} \quad (2-9)$$

Where a is the radius of the projected contact area. The Hertz equation is differentiated by the depth h and substituted by the differential equation. It can derive that

$$P = \frac{2}{3} \frac{dP}{dh} h_e \quad (2-10)$$

dP/dh equals to the contact stiffness S . Therefore, Equation (2-10) will be

$$h_e = \frac{3}{2} \frac{P}{S} \quad (2-11)$$

If h_e is determined, it can be used to derive the contact area according to Equation (2-9). The reduced modulus can be worked out by

$$E_r = \frac{S}{2a} \quad (2-12)$$

For the elastic-plastic condition, where there is an impression left when the applied force total unloaded. It means that h_f is larger than zero. The analysis of this situation is similar to the Oliver-Pharr method, which is used in Berkovich tip. The contact stiffness and depth can be determined by the loading-unloading curve. The contact depth h_c is given by

$$h_c \approx h_{total} - \frac{h_e}{2} \quad (2-13)$$

Substituting (2-11) to (2-13) yields

$$h_c = h_{total} - \frac{3}{4} \frac{P}{S} \quad (2-14)$$

Where indicates using the value of factors $\beta = 0.75$ for spherical tip.

For small spheres with the diameter less than $2\mu\text{m}$, the perfect spherical profile is difficult achieve, it uses a reference sample with known property to determine area function. For the diameter of sphere more than $2\mu\text{m}$, the contact is under the function of contact depth and radius:

$$A = \pi(2Rh_c - h_c^2) \quad (2-15)$$

When the contact area is determined, it can be used to work out the hardness and elastic modulus based on Equation (2-5) and (2-7).

2.1.3 Frame compliance

In nanoindentation system, it is important to acknowledge that not only the tip and specimen are elastic element, but the frame compliance should be considered as elastic element [39].

$$C_T = C_S + C_F \quad (2-16)$$

where C_T is the total compliance, which is observed in the experiment, the compliance of the sample is C_S and the last one C_F is frame compliance. Because the sample compliance can be obtained by the inverse of contact stiffness, Equation (2-16) can be transferred as

$$C_T = \frac{\sqrt{\pi}}{2\gamma E_r} + C_F \quad (2-17)$$

Consequently, it is necessary to determine the compliance of the frame prior to the experiment. Sometimes, the frame compliance is unknown. Generally, an iterative method is used to approach accurate approximation of the result.

Another method of determining the frame compliance can be performed without knowledge the area function. It was based on the regulation that the value of H / E^2 is independent of contact area

$$\frac{P}{S^2} = \frac{\pi}{2\gamma} \frac{H}{E_r^2} = PC_s^2 \quad (2-18)$$

Based on Equation (2-18) to substitute C_S in Equation (2-16) yields

$$\sqrt{P}C_0 = \frac{\sqrt{\pi}}{2\gamma} \frac{\sqrt{H}}{E_r} + \sqrt{P}C_F \quad (2-19)$$

This equation demonstrates that the relationship between $\sqrt{P}C_0$ and \sqrt{P} is linear with a gradient of C_F . Based on that, the compliance of the frame can be worked out. Another method is for the known hardness and reduced modulus value, which can be substituted into Equation (2-18) to directly determine the value of frame compliance.

2.1.4 Pile-up and sink-in behaviour

It is assumed that during the indentation process, the material around the contact area deforms elastically. While there is also plastic deformation occurs around the contact area. Bolshakov and Pharr studied this behaviour impact on the results of mechanical properties through finite element method [40]. They established the indenter as a rigid conical tip and there was no consideration in friction between the sample and tip. It was found that the surrounding of material piled up and increased the contact area when the material with a high value of E_r / σ_y . Conversely, the material with lower value of E_r / σ_y exhibited the surrounding of the indent sink-in behaviour and thus reduced the contact area. In addition, work hardening also contributes to sink-in behaviour. Consequently, both pile up and sink in phenomena resulted in variation in the measured contact area. Figure 2.6 demonstrates these behaviours and the surface contour with plastic zones obtained by finite element methods.

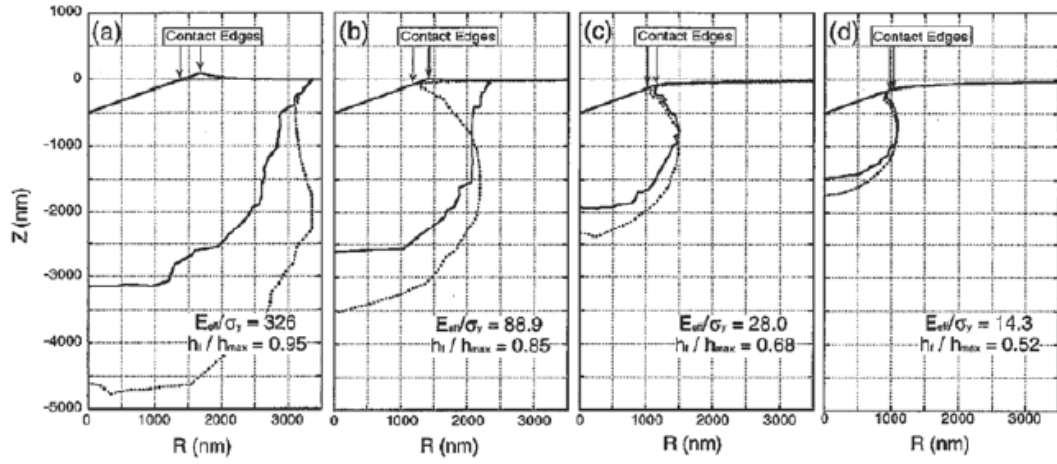


Figure 2.6 Surface contours and plastic zones predicted FEM for materials with different values of E_r / σ_y . Non-work hardening materials ($\eta = 0$) are represented by solid lines h_f / h_{\max} and work-hardening materials ($\eta = 10\sigma_y$) by broken lines [40].

Another indicator for pile-up phenomenon is the elastic recovery ratio, h_f / h_{\max} . When the value of E_r / σ_y is more than 0.7, it mthe pile-up phenomenonree of pile-up phenomenon occurs. It is difficult to correct the errors induced by these behaviours except for acknowledging the mechanical properties of E_r , σ_y and work hardening information about the sample. Another solution for this problem is determining the contact area by taking an image under optical microscopy [41].

The relationship between the ratio of H / E_r and the work of indentation is independent of the pile-up behaviour, claimed by Cheng and Cheng [42], who implemented the dimensional analysis and finite element method. Oliver and Pharr [43] demonstrated the relationship as

$$\frac{W_{tot} - W_u}{W_{tot}} \approx 1 - 5 \frac{H}{E_r} \quad (2-20)$$

Where W_{tot} is the total work of indentation and the elastic recovery work is W_u , which is shown in Figure 2.7. It has found that this method is suitable for the material with high elastic recovery.

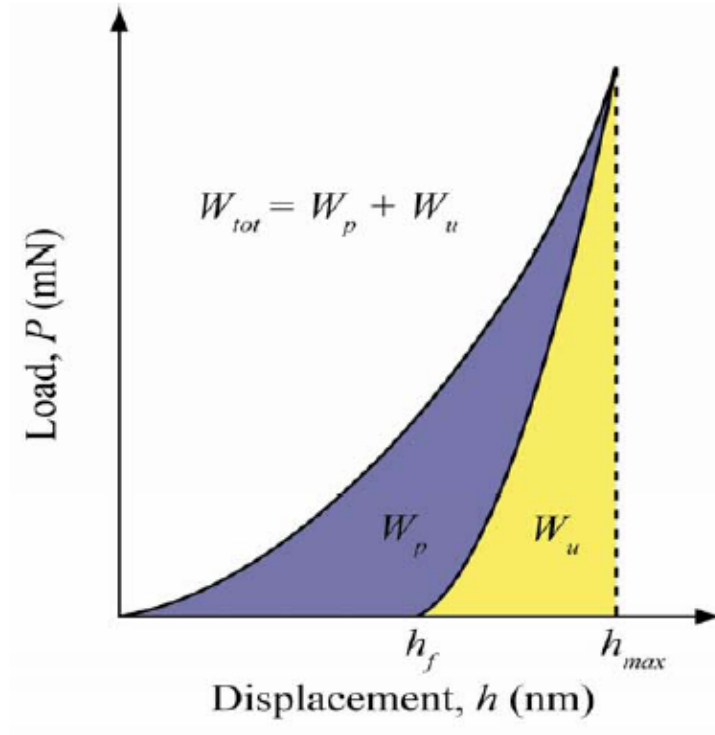


Figure 2.7 Schematic showing the definition of plastic, elastic and total work of indentation.

2.1.5 Load function

The input loading profile also plays a vital part in the nanoindentation experimental [44]. Most of commercial facilities are able to carry on load-control mode compared to the displacement-control mode in the servo-hydraulic test facility. Due to the indenter is pressed into the material and then unloaded. The loading-unloading profile is commonly considered as load control. Standard loading profiles include (1) ramping and retracting under constant loading rate, (2) increasing to a peak value and keeping

for a period time prior to unloading, (3) loading at exponentially without holding period:

$$P(t) = P_0 \exp(rt) \quad (2-21)$$

Where P_0 is a small load at the beginning stage and r is the strain rate. These three loading profiles are demonstrated in Figure 2.8. The loading profile in Figure 2.8 (c) is able to offer a constant strain-rate in the nanoindentation experiment. In addition, the displacement control function is equipped with some indentation facilities. Similarly, the displacement can be controlled to ramp, hold and retract to original position.

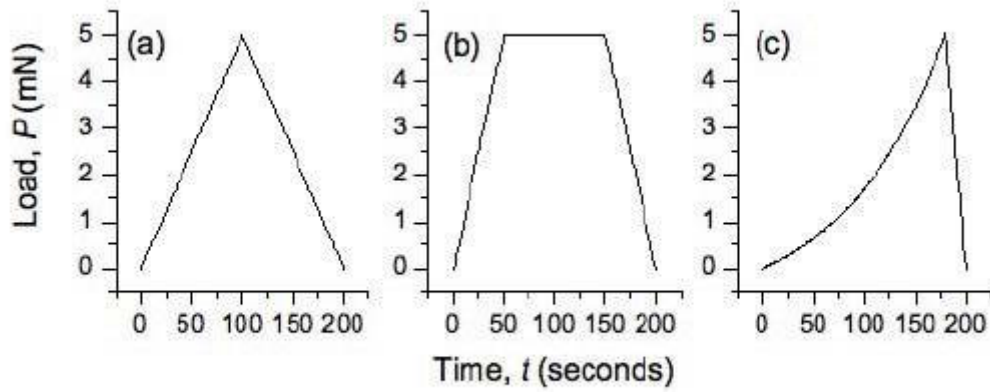


Figure 2.8 Applied force-time profiles for (a) a simple load-unload cycle under triangular loading, (b) a trapezoidal load-hold-unload profile in which creep can be measured during the holding period, and (c) exponential loading.

2.2 Elastic and plastic contact

2.2.1 Elastic contact

The basic theory of elastic contact is originated from the Hertz contact theory [45]. Moreover the theory was reviewed by Johnson. This theory modelled the contact of two spherical parts with radius R_1 and R_2 .

For the spherical indentation, the model of Hertz contact can be converted to a spherical tip press on an unlimited half space. The radius of the project area a is smaller than the radius of the probe, and there function is

$$a = \sqrt{R / h} \quad (2-22)$$

The relationship between the load (p) and displacement (h) for spherical indentation (Hertzian contact) is:

$$p = \frac{4\sqrt{R}}{3} \frac{E}{1-\nu^2} h^{3/2} \quad (2-23)$$

By using this equation, it indicates that the tip is much harder than the sample. The load-displacement curve for a perfect elastic spherical indentation is shown in Figure 2.9.

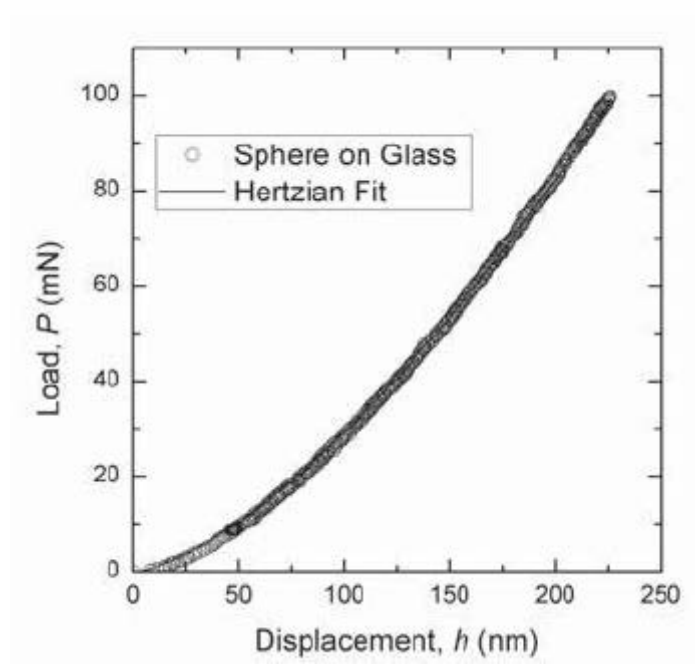


Figure 2.9 Load-displacement (P-h) curve of perfectly elastic (Hertzian) contact on glass [25].

The strain of the indentation can be used to determine whether the contact is perfectly elastic deformation or not:

$$\varepsilon_i = 0.2\left(\frac{a}{R}\right) = 0.2\left(\frac{h}{R}\right)^{1/2} \quad (2-24)$$

The contact is perfectly elastic at shallow indentation with small strain, when the yield stress has not been achieved [46]. The load-displacement curve will shift, because of plastic deformation under the condition of yield stress reached.

Despite the flat tip not commonly used in probing hard sample, it is one of suitable choice for investigation extremely soft samples including hydrogel and biological tissues [47]. The relationship between the applied force and displacement under a cylindrical tip with radius R is:

$$P = 2R \frac{E}{1-\nu^2} h \quad (2-25)$$

According to the above equation, the relationship between the applied force and displacement is linear.

The sharp indenter is the most widely used tip, including conical or pyramid in nanoindentation [48]. The three-sided pyramid, named ‘Berkovich’ was designed for nanoindentation to replace of the four-sided Vicker tip, which is often used in traditional macro or micro scale indentation. The solution for conical indentation under perfect elastic deformation is:

$$P = \frac{\pi \tan \gamma}{2} \frac{E}{1-\nu^2} h^2 \quad (2-26)$$

2.2.2 Elastic-plastic deformation

The plastic information in an indentation test is measured by hardness, which exhibits the resistance to plastic deformation. In traditional microindentation, the impression after an indentation process is measured by optical microscopy [49]. Then, hardness can be calculated based on the ratio between peak force and the projected area:

$$H = \frac{P_{\max}}{2b^2} = \frac{P_{\max}}{\pi a^2} \quad (2-27)$$

where b is the half length of the diagonal line of Vickers tip and a is the radius of the contact area for circle impression. For soft metals, the most of impression is due to plastic information. When it comes to ceramics, they often own both elastic and plastic elements. In most polymers there is very little plastic deformation during the indentation process [50].

To analysis the elastic-plastic deformation in the indentation test, it commonly separates elastic and plastic deformation to work out the elastic modulus and hardness effectively. The initial contribution in this field was made by Doerner and Nix [51] prior to the milestone work of Oliver and Pharr, which is most widely used for conical and pyramid nanoindentation. The deviation of elastic information from elastic-plastic material under ranoindentation will be reviewed in this section.

For spherical indentation, the relationship between load and displacement would change from $P \propto h^{3/2}$ to $P \propto h$ when the deformation varies from elastic to plastic. According to Figure 2.10, the indentation curve of aluminium plotted on a log-graph paper clearly shows the relationship between force and displacement shifts to $P \propto h$. However, the result of glass sample remains under elastic function.

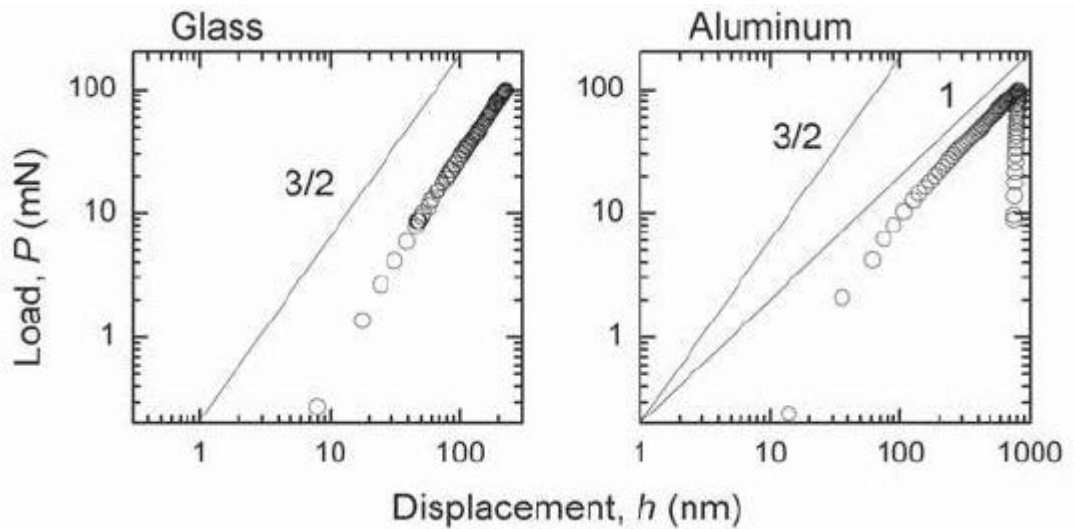


Figure 2.10 Elastic-plastic indentation responses for a sphere on fused silica glass and aluminium [25].

To separate the elastic and plastic deformation in the spherical indentation response, it uses a correction of the Hertz contact function by assumption the elastic unloading

process.

$$E_R = \frac{3}{4} \frac{P}{h_e^{3/2}} \left(\frac{1}{R} - \frac{1}{R'} \right)^{1/2} \quad (2-29)$$

where h_e is the penetration depth for elastic deformation and $(1/R - 1/R')$ is the correlative curvature between the tip and the impression on the sample.

The use of sharp indenters, including conical or pyramid tip is commonly used for investigating the elastic-plastic sample. The relationship between the force and displacement is $P \propto h^2$ for both conical and pyramid indenter used for elastic-plastic deformation. It is impossible to separate the elastic and plastic information as the same method as spherical indenter. The approach for separating elastic and plastic information in Oliver and Pharr method is assumed that the unloading process is pure elastic deformation with the relationship between reduced modulus and contact stiffness.

$$E_R = \frac{S\sqrt{\pi}}{2\sqrt{A}} \quad (2-30)$$

While in actual experiment, the indenter will become wear and blunt. Therefore, the contact area function is often shown as a summed polynomial equation:

$$A_c(h_c) = C_0 h_c^2 + \sum_{k=1} C_k h_c^{1/2^{(k-1)}} \quad (2-31)$$

where the coefficient C_i will be determined in the calibration.

2.3 Instrumentation for indentation experiment

2.3.1 Instrumented indentation testing facility (nanoindenter)

Instrumented indentation testing (IIT), also known as depth-sensing indentation

(DSI), is able to perform the nanoindentation experiment by measuring the load and depth during the probe contact with the specimen. The deformation of the testing system is much smaller than the elastic and plastic deformation occurred in the sample. The indentation depth is usually a few micrometers or less with nanometer resolution. This type of facility is very suitable to investigate the contact response at sub-micro scale and normally named as 'nanoindenter'.

The typical structure of nanoindenter is shown in Figure 2.11. There is a pretty stiff frame to support the probe to carry out the experiment on an anti-vibration platform [52]. The indentation axis is defined perpendicular to the platform. The position of the probe is controlled by the indentation system along the axis. It is important to note that the applied force and the displacement of the probe are measured remotely from the contact, where the tip pressed into the sample. The remote measured displacement is not equivalent to the displacement of indenter to the sample surface due to the deformation of the apparatus frame [53]. Therefore, the displacement of the tip is related to the stiffness of the facility frame and the probe-surface interaction. The indentation frame is often considered as a linear elastic element with one spring stiffness.

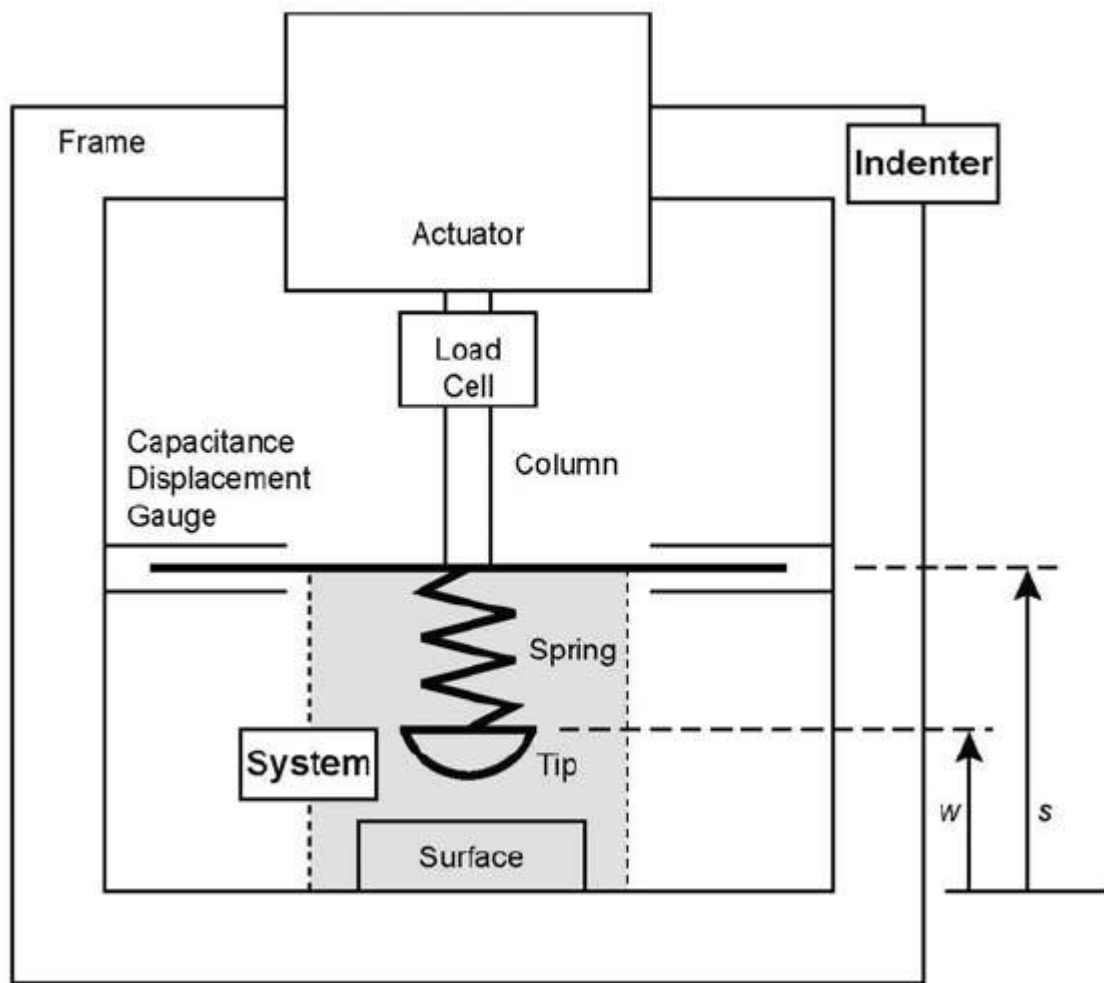


Figure 2.11 Schematic of an instrumented indentation testing apparatus. The spring and tip comprise a probe. An indenter environment imposes and measures load, displacement to the system.

Generally, the output force and displacement signals are voltages. It is commonly used in most commercial instrumented indentation testing facility that there is a linear relationship between the voltage signal and the value of output [54].

Currently, most of commercial instrumented indentation systems are designed to explore the mechanical properties of metals, ceramic, glass, which are relatively stiff material. It is important to note that the resolution and range of such nanoindenter is

whether or not suitable for polymers, which exhibit viscosity properties. In addition, for the compliant sample, under the same applied force, the displacement is larger than the stiff sample. Therefore, the deformation of compliant material can go beyond the capacity of the displacement sensor. More importantly, it is necessary to reflect the viscosity in these kinds of materials rather than simple Oliver - Pharr method, which is used to investigate elastic-plastic samples.

2.3.2 Atomic force microscopy

Atomic force microscopy is another type of facility, which is able to explore the contact behaviour at the nano or sub-nano scale. Similar to nanoindenter, AFM has the ability to press a probe onto the surface and measure the force and displacement of this process [55]. However, the resistance of the tip to the deformation is not bigger than that to the surface. Therefore, it is commonly used to measure the adhesive force. The advantage of AFM is that it can measure less than 100 nanometer displacement with 0.1 nano resolution [56]. Consequently, AFM is suitable to measure at an extremely small displacement and force. It is also can be used as a microscopy to image the topography of the surface. While, the image function is not considered here.

The ability of contact measurement of AFM is analogous to nanoindenter, which is able to generate P-h curve used for analysis the mechanical properties of the sample. The obvious difference between AFM and nanoindenter is the stiff of the probe, which enables AFM to better explore the adhesion phenomenon during the contact.

The schematic of a typical AFM is shown in Figure 2.12. The system consists of an

extremely stiff frame to support the probe and platform for fixing the sample. In the measurement probe, there is a cantilever beam which is clamped at one end with another freehold end. The fixed end is connected to a displacement actuator; another end is equipped with the tip, which is used to probe the sample. The interaction between the tip and surface will impose a force on the cantilever, where deformation occurs due to a bending moment. This bending moment will lead to the cantilever deflect to the end of the actuator. From the back of the cantilever, there is a beam of laser reflected and collected by a photodiode detector. The deflection caused by the interaction between the tip and sample will move the spot of laser on the detector [57]. Therefore, the tip-surface interaction can be investigated through the output of the photodiode

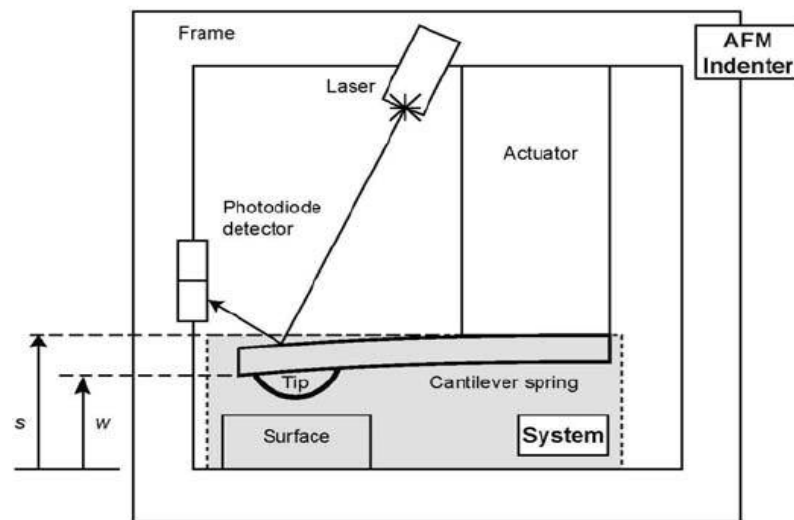


Figure 2.12 Schematic demonstration of an AFM contact testing apparatus. The cantilever spring and tip comprise a probe, which together with a sample test surface comprise a simple mechanical thermodynamic system.

Nanoindenter is designed to minimize the compliance of the sample and capture the load and the displacement signal via separate sensor. In contrast, AFM acquires the contact force through the deflection of the cantilever. Generally, the cantilevers used in the AFM are made from silicon or silicon nitride through microelectronic lithography. The dimension of the cantilever is varied to obtain a range of stiffness between 10 N/m and 0.001 N/m [58]. The shape of the cantilever is rectangular or triangular. The latter type is suitable for low stiffness measurement, which can reduce the deformation of the cantilever in the experiment.

The force sensor has to be calibrated before use. There is a limitation of the position sensitive detector in the linearity of the signal. When the bending of the cantilever beyonds its linear scope, there will be nonlinear error in the response of loading and displacement. This problem can be solved by a direct process to linearize this signal over the whole range of the cantilever. The most detailed of this method is shown in Figure 2.13, which indicates there is a reduction of 5% to 50% errors in the results of elastic modulus.

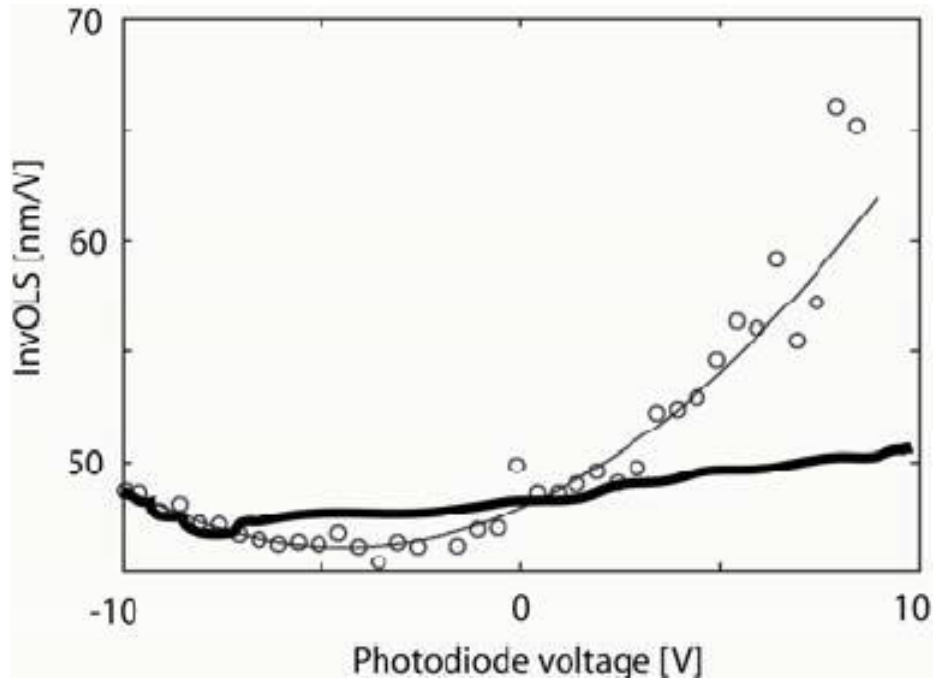


Figure 2.13 AFM cantilever deflection is not linear over a wide range of operating voltages [59].

2.4 Viscoelastic contacts

2.4.1 Viscoelastic material

With the advent of polymers used in real life and manufactured in the industry, there is a growing interest in characterizing the mechanical properties in such material with viscoelastic property. The materials with almost elasticity have the capability to store the energy. While the viscoelastic materials exhibit not only store the energy, but also dissipate it simultaneously. When the material is under pressed suddenly without impact which will result in dynamic response, the elastic one will deform instantaneously with the increased force to the peak value. However, the response of

viscoelastic sample is different that the deformation may not synchronize with the applied force. In addition, the respond is time dependent, for instance, if the stress is constant, the strain will vary with the time.

2.4.2 Viscoelastic mechanics

The mechanical behaviour of viscoelastic material often represents the combination of elastic element of linearity spring:

$$\sigma = E\varepsilon \quad (2-32)$$

and linearly viscous ‘dashpot’ element

$$\sigma = \eta \frac{d\varepsilon}{dt} \quad (2-33)$$

Ting et al [60] studied the indentation of the linear viscoelastic material, the stress and strain can be expressed as

$$\sigma(t) = \int_0^t \psi(t-\tau) \frac{\partial \varepsilon(\tau)}{\partial \tau} d\tau \quad (2-34)$$

$$\varepsilon(t) = \int_0^t \Phi(t-\tau) \frac{\partial \sigma(\tau)}{\partial \tau} d\tau \quad (2-35)$$

Where $\psi(t)$ is the function of relaxation, which represents the response of the stress to a change of strain, $\Phi(t)$ is the function of creep compliance. Based on the Hertz contact theory, the relationship between the radius of contact area and the force is:

$$a^3(t) = \frac{3R}{4} \int_0^t \Phi(t-\tau) \frac{dP(\tau)}{d\tau} d\tau \quad (2-36)$$

If the applied force is a single step force

$$P(t) = \begin{cases} 0 & t < 0 \\ P_0 & t \geq 0 \end{cases} \quad (2-37)$$

Equation (2-36) transfers to

$$a^3(t) = \frac{3}{4}RP_0\Phi(t), \quad t > 0 \quad (2-38)$$

2.4.3 Viscoelastic models

There are different models for analysis the viscoelastic material, the solutions for different model will summarize in the following sections.

2.4.3.1 Kelvin model and Maxwell model

Kevin model and Maxwell model are two simple models used for viscoelastic material. Kelvin model consists of a spring and a dashpot in parallel, whereas the Maxwell model represents a spring and a dashpot in the series (Figure 2.14).

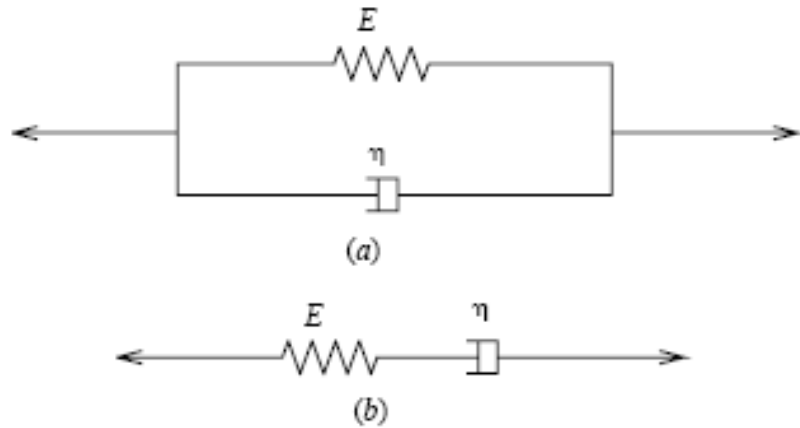


Figure 2.14 Viscoelastic models: (a) Kelvin Model; (b) Maxwell Model.

For Kelvin model, the total stress equals to the combination of the stress in the element of spring and dashpot.

$$\sigma(t) = \sigma_s + \sigma_d = E\varepsilon(t) + \eta\dot{\varepsilon}(t) \quad (2-39)$$

where E is the spring constant and η is the viscosity coefficient.

The solution under a given stress history is:

$$\varepsilon(t) = \frac{1}{\eta} \int_{\tau_0}^t \sigma(\tau) e^{-\lambda(t-\tau)} d\tau \quad (2-40)$$

where t is the relaxation time, $t = \frac{\eta}{E}$.

Therefore,

$$\Phi(t-\tau) = \frac{1}{E} \{1 - e^{-\lambda(t-\tau)}\} \quad (2-41)$$

$$\Psi(t-\tau) = E\Delta(t-\tau) + \eta\delta(t-\tau) \quad (2-42)$$

where

$$\Delta(t) = \begin{cases} 0, & t < 0 \\ 1, & t \geq 0 \end{cases} \quad (2-43)$$

$$\delta(t) = \dot{\Delta}(t) \quad (2-44)$$

The results of creep and relaxation test are shown in Figure 2.15.

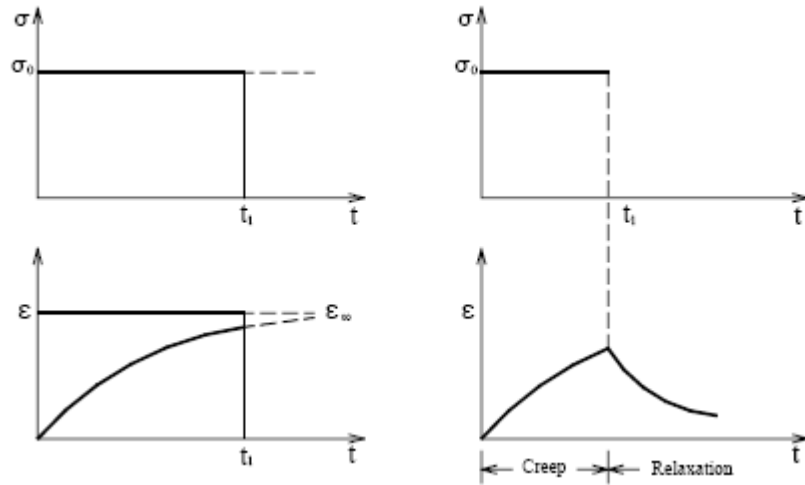


Figure 2.15 The creep and relaxation of Kelvin model

Substituting Equation (2-41) to (2-38) yields

$$a^3(t) = \frac{3}{4E} RP_0 \{1 - e^{-\lambda t}\} \quad (2-45)$$

For the Maxwell model, the total strain equals to the sum of each element:

$$\dot{\varepsilon}(t) = \frac{\dot{\sigma}(t)}{E} + \frac{\sigma(t)}{\eta} \quad (2-46)$$

The solution for the Equation (2-46) is

$$\varepsilon(t) = \frac{\sigma(t)}{E} + \frac{1}{\eta} \int_{\tau_0}^t \sigma(\tau) d\tau \quad (2-47)$$

When $\sigma(t)$ is known

$$\sigma(t) = E \int_{\tau_0}^t e^{-\lambda(t-\tau)} \dot{\varepsilon}(\tau) d\tau \quad (2-48)$$

When $\varepsilon(t)$ is known

Therefore, the creep and relaxation function are

$$\Phi(t-\tau) = \frac{1}{E} + \frac{t-\tau}{\eta} \quad (2-49)$$

$$\Psi(t-\tau) = E e^{-\lambda(t-\tau)} \quad (2-50)$$

The results of creep and relaxation tests are shown in Figure 2.16

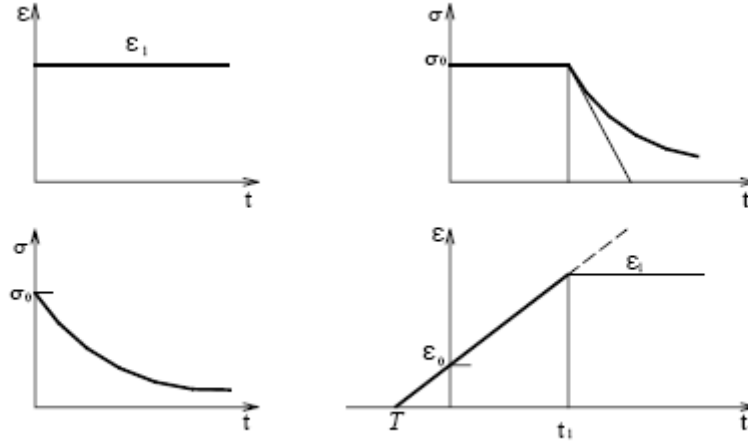


Figure 2.16 The creep and relaxation of Maxwell model

Based on the Equation (2-49) and (2-38), the contact radius is

$$a^3(t) = \frac{3}{4} R P_0 \left\{ \frac{1}{E} + \frac{t}{\eta} \right\} \quad (2-51)$$

2.4.3.2 Standard linear solid model

The standard linear solid model includes three elements: a Kelvin model in the series with a spring, the schematic of this model is shown in Figure 2.17.

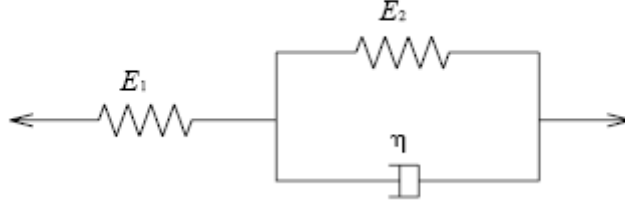


Figure 2.17 Three-parameter model

The governing relationship in this model is

$$E_1 \eta \dot{\varepsilon} + E_1 E_2 \varepsilon = \sigma(E_1 + E_2) + \eta \dot{\sigma} \quad (2-52)$$

The solution for Equation (2-52) is

$$\varepsilon(t) = \frac{\sigma_0}{E_1} + \frac{\sigma_0}{E_2} \{1 - \exp[-E_2(t - t_0) / \eta]\} \Delta(t - t_0) \quad (2-53)$$

$$\sigma(t) = \varepsilon_0 \{E_\infty + (E_1 - E_\infty) \exp[-(E_1 + E_2)(t - t_0) / \eta]\} \quad (2-54)$$

where $E_\infty = E_1 E_2 / (E_1 + E_2)$.

Therefore, the creep and relaxation function are (Figure 2.18)

$$\Phi(t) = \frac{1}{E_1} + \frac{1}{E_2} \{1 - \exp(-t / T_1)\} \quad (2-55)$$

$$\Psi(t) = \frac{E_1}{E_1 + E_2} \{E_2 + E_1 \exp(-t / T_2)\} \quad (2-56)$$

where $T_1 = \eta / E_2$, $T_2 = \eta / (E_1 + E_2)$.

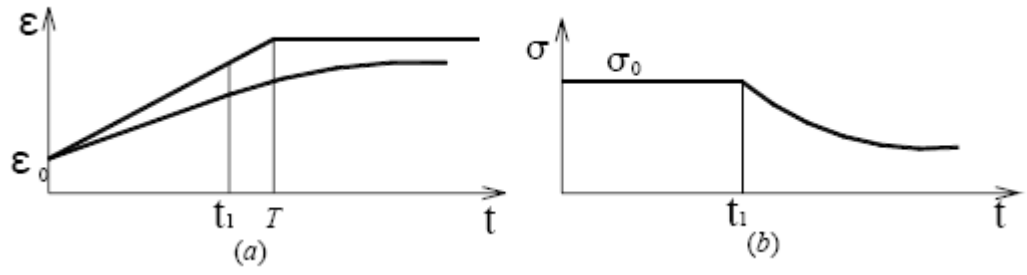


Figure 2.18 Creep phase (a) and relaxation phase (b) of three-parameter model

The contact radius for spherical indentation based on this model is

$$a^3(t) = \frac{3}{4} RP_0 \left\{ \frac{1}{E_1} + \frac{1}{E_2} \exp(-t/T) \right\} \quad (2-57)$$

2.5 Summary

With the wider application of nanoindentation techniques, it is necessary to explore viscoelastic material by this method. Consequently, nanoindentation technique is reviewed including basic procedures, indenter geometry, frame compliance as well as behavior of pile-up and sink-in. Moreover, the contact theory of elastic-plastic and viscoelastic material are reviewed as well. Additionally, two types of facilities, nanoindenter and AFM are introduced. Both exhibit limitation of characterization of viscoelastic material. Therefore, it is worth investing effort into this area to innovate next generation instrument.

Chapter 3 An improved home-made facility for characterizing the mechanical properties of viscoelastic materials

3.1 Introduction

There are very few materials with atom level flatness and most of materials have an undulation topography, which has an impact on its performance of mechanical properties [61]. Therefore, it is important and worthwhile to investigate the relationship among surface topography and its mechanical properties.

The indentation experiment is a widely used method to characterize the mechanical properties of different materials. When performing the indentation test at small scale, this technique has been referred to “nano-indentation”. Traditionally, it had successfully characterized stiff or hard materials, such as glasses, metals and ceramics [33]. In recent two decades, it was able to measure the mechanical properties of small volume samples including thin-films and microstructure samples, which are difficult or impossible to be measured under tensile or compression test.

In recent years, there is a growing attention in the characterizing the mechanical properties of soft material, such as polymers, hydrogels and biomaterials [62]. However, these compliant materials are capable of storing and dissipating energy contemporaneously. During the nano-indentation process, the response is more difficult to interpret for soft materials when compared to the traditional engineering

materials due to their viscoelastic properties [63]. Thus, the application of nano-indentation technique in these materials a major challenge to explore and resolve.

The commercial nano-indentation testing facility is suitable for a small range of engineering materials of elastic modulus between 1 GPa to hundreds of GPa, and these conventional tests are performed under mN and nm range [64]. When it comes to soft matters with MPa or even lower in elastic modulus, the range of force and depth will be altered to μN - μm or mm. This is an instrumentation challenge when performing on soft materials.

In the previous work, our research group developed a unique instrument, the multi-function tribological probe microscopy (TPM) [19], which is able to map four properties of traditional hard materials: topography, hardness, elastic modulus and friction force. To study the viscoelastic material and expand the application of the previous instrument, a new improved measuring system was developed. This chapter includes the establishment and calibration of this system, which is able to demonstrate a new generation of instrument to investigate the relationship between the surface topography and viscous properties of soft matter.

3.2 Designed details of improved system for mechanical properties of viscoelastic material study

3.2.1 Scheme of the system

The schematic and photos of the testing system are shown in Figure 3.1 and Figure

3.2, respectively. A PI X-Y stage is installed to perform the scanning range of 250×250 mm² with a resolution of 1 μ m. This linear position stage is fixed on a Newport vibration isolation platform to prevent the impact of surrounding vibrations. A PZT (piezoelectric transducer) based linear position translator (PI Nextline) is equipped in the vertical direction to provide 20mm travel range with 5nm resolution for the probe.

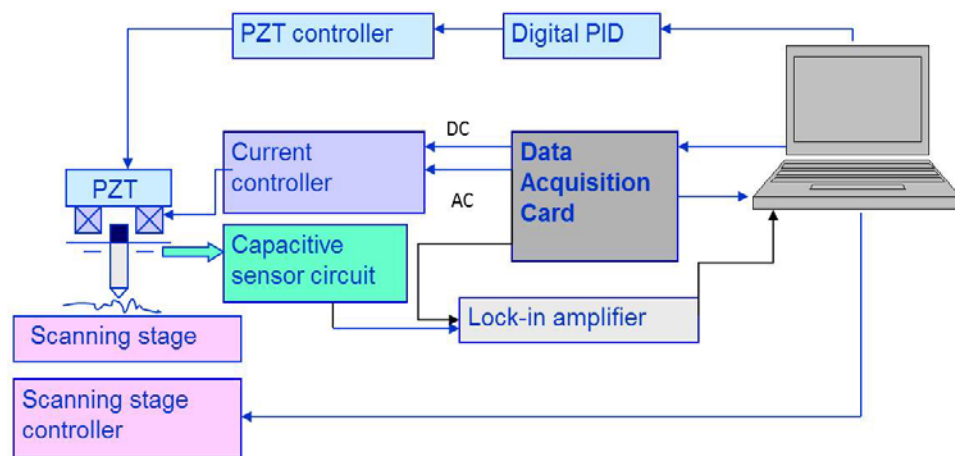


Figure 3.1 Schematic of TPM system.

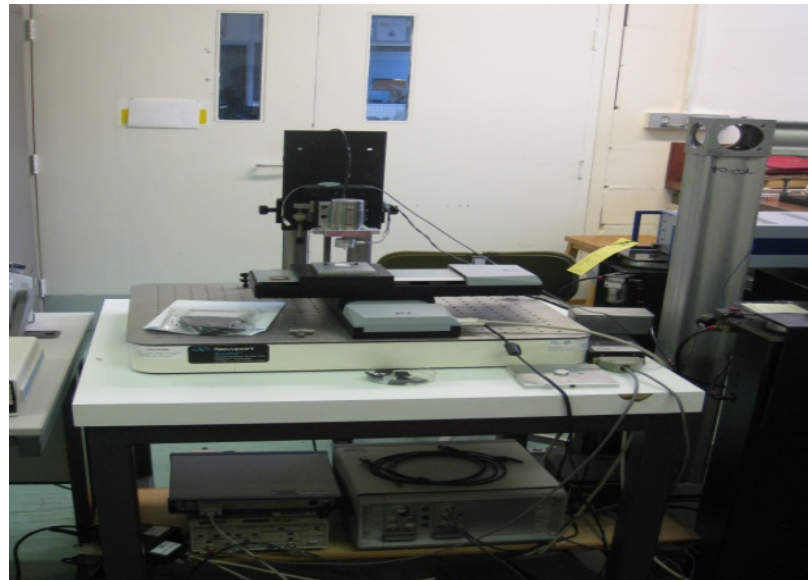


Figure 3.2 Photo of TPM system.

For the displacement sensor in the probe, there are different selections in the scope of several micrometres with nanometer resolution. The option of inductive sensor could provide a good linearity with a large measurement range with accurate sub-nanometer resolution. However, the disadvantage of this type of sensor is that by using this technique, the size and weight of the probe would decrease the natural frequency of the system, which would not be suitable for characterizing the viscoelastic material. Another option is optical sensor, which is widely used is SPM (Surface Probe Microscopy) system. The challenge of using this type of sensor is that it needs large space for equipping the optical system. As a consequence, a capacitive sensor is formed in the probe, which is very compact and suitable for dynamic testing. A cross beam cantilever with a fixed electric end is designated to act as the displacement sensor.

When it comes to the force sensor in this system, there are also different selections including piezo force actuator, electrostatic force actuator and magnetic force actuator. Although the piezo force actuator can be formed very small and compact, because of its nonlinearity with hysteresis and creep, it is not considered in this study. The electrostatic force actuator is able to apply the force at the range of millinewton. If the probe is built very small, it is difficult to prevent two electrodes coming into contact, which would result in damaging the electrode. Therefore, the magnetic coil force actuator is used in this system. This technique has a perfect linearity and easy to control. The current passes through the magnetic coil, the indenter is actuated by the magnetic force.

This system utilizes an NI 6289 data acquisition card (DAQ) to output the voltage to control the current passing through the magnetic coil. In addition, this DAQ card is able to collect the signals from the capacitive sensor which indicates the displacement of the tips. The merit of this system is using a lock-in amplifier to measure the phase lag between the applied load and the corresponding displacement in dynamic nanoindentation.

3.2.2 Design details of the sensing probe

In this section, the mechanical structure of the probe will be described including the magnet coil and capacitive sensor design. The probe is the core part of the testing system. The detailed structure of the probe is shown in Figure 3.3.

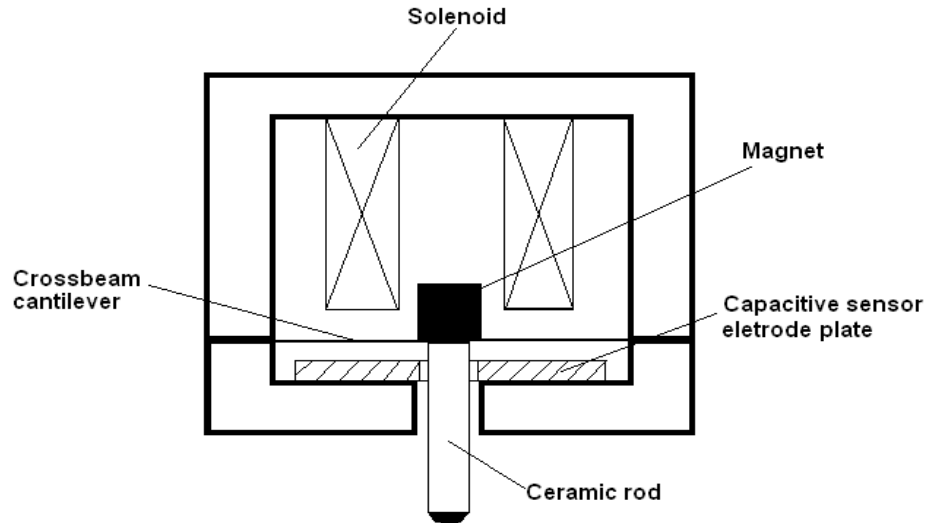


Figure 3.3 Schematic of mechanical probe.

A crossbeam cantilever made from beryllium copper is used to act as a flexible electrode with a permanent magnet glued on the centre top and a ceramic rod attached

at the central bottom. The magnet is surrounded by a coil, which is mounted inside the chamber and controlled by passing through current to apply force on the tip.

The essential part in this probe is crossbeam cantilever, which determine the stiffness of testing probe. The electrodes of the capacitive sensor are 25 μm thickness and a 100 μm thickness plastic film are used to insulate two electrodes from each other and the housing probe.

The magnet is a saturated permanent magnet of Neodymium-boron-iron (NdBFe). There is no contact between the magnet and the solenoid coil. The actuated force is linear with the current and independent of small beam deflection resulted from the magnetic field. A simple magnetic coil structure is shown in Figure 3.4. A circular cylindrical coil is mounted in the probe and the magnet is assembled in the center of the circular cylinder. The magnetic force is dependent on the structure parameters including the length of the coil L , the inside and outside radius of coil a_1 and a_2 .

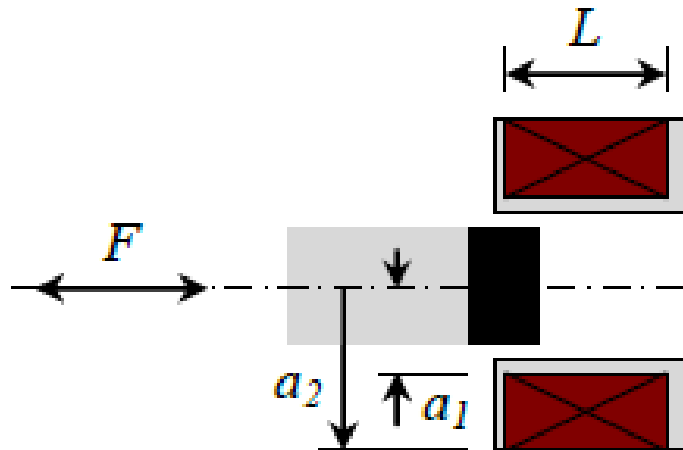


Figure 3.4 Schematic diagram of magnet-coil force actuator

According to the previous work [19], the optimum position for magnetic is ranged

between $0.5L$ and L from the coil center axis. The optimum geometry of the coil is $L=a_2=2a_1$. The parameters of the coil design are listed in Table 3-1.

Table 3-1 Parameters of magnetic coil

Parameters	Dimensions
Number of coil turns	400
Internal radius of the coil (a_1)	4mm
External radius of the coil (a_2)	8mm
Length of the coil (L)	8mm
Diameter of the magnet	3mm
Thickness of the magnet	2mm

The length of the coil equals to the external diameter and twice as the inner diameter. The coil is formed with 400 turns of copper wire with 0.12 mm diameter with 20Ω . The coil is fixed to the body of the probe by three screws. The sensitivity of the magnetic actuator will be discussed in section 3.3.

3.2.3 Indenter tip selection

The selection of the indentation tip has a direct impact on the result of the experiment, especially for characterizing the viscoelastic sample. In addition, different types of tips have their own particular advantages and disadvantage for different samples.

The common used tip for nanoindentation experiment is known as Berkovich tip,

which has three sides geometry. Normally, this type of tip is made by diamond, which is machined three sides to a single point. This would result in the sharpest tip compared to other geometry. As a consequent, Berkovich tip is commonly used for probing hard, bulk materials or thin film samples. However, it was claimed by Tweedie et al [66] that using Berkovich tip for characterizing the viscoelastic properties of polymers was unsuccessful.

Another widely used type of tip is flat ended one. The advantage of flat end tip is that the contact area will not change during the loading and unloading process. While the disadvantage is unavoidable that it is not able to mount perfectly parallel to the surface of the sample. There always exists a small angle between the flat tip and the surface of the sample. In addition, the flat geometry is likely to result in stress concentration along the circle edge of the contact.

According to the above discussion, it is concluded that the spherical tip is most suitable for characterizing the viscoelastic material. Consequently, a spherical sapphire tip with 500 μm radius is used as the tip, which is glued on the end of the ceramic rod in the bottom of the probe.

3.2.4 Voltage-controlled current (U-I) driver

A home-made voltage-controlled current source is used to drive the magnetic coil force actuator. The circuit diagram of this driver is shown in Figure 3.5. It can be controlled by manual input or by direct current to alternative current (D/A) input through the computer. SW_1 is act as the switcher to alter between these two modes.

The current output from LOAD is independent of the resistance of LOAD, due to

Where U_{out} is the output voltage and R is a pair of reference resistances in parallel. R equals to 10Ω in this circuit. The relationship between input and output voltage is

51

Where $R_3 = 5k\Omega$. Hence, the relationship between input voltage and current is

$$\frac{I}{U_{in}} = \frac{2R_3}{10k\Omega \cdot R} = 100mA/V \quad (3-3)$$

The photo of PCB circuit is shown in Figure 3.6.

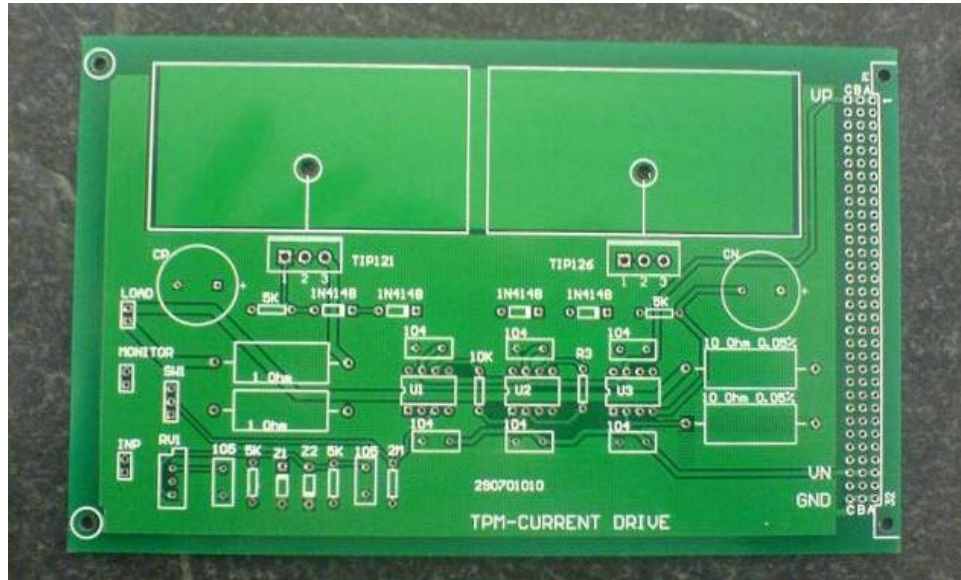


Figure 3.6 PCB circuit of voltage-current driver.

The calibration of the sensitivity has been performed for the voltage control current drive, by inputting a series from 0V to +5V through a 10Ω resistant. The calibration result is shown in Figure 3.7. It is found that the relationship between input voltage and output current is linearity at 100mA/V.

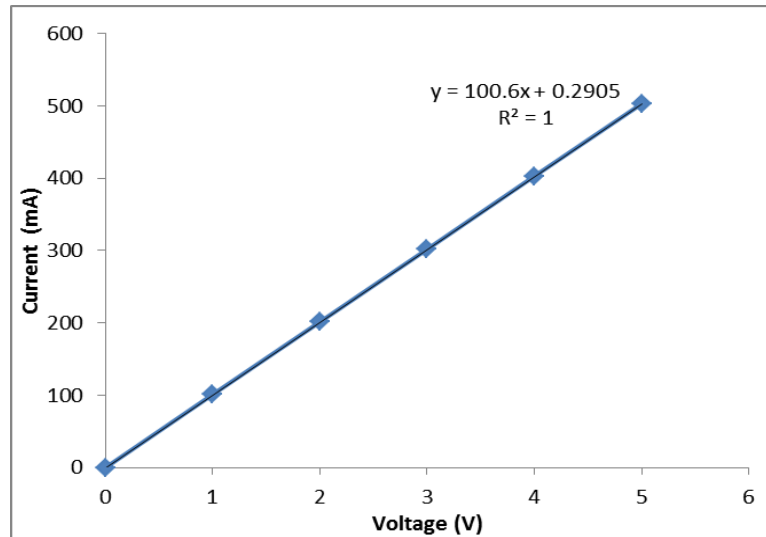


Figure 3.7 The voltage-current drive calibration.

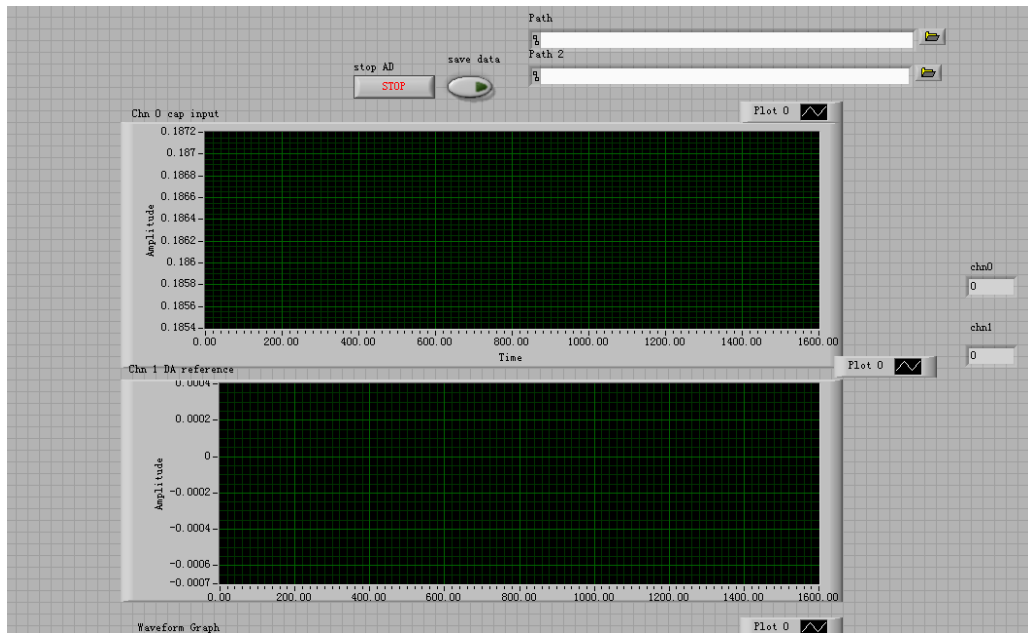
3.2.5 Operating software

The process of control the input and output signal if the system is operated by a computer through an NI 6289 DAQ card. The operating program in PC is based on Labview software package, which is self-designated to offer real-time data measurement. The front panel and block diagram of Labview is shown in Figure 3.8.

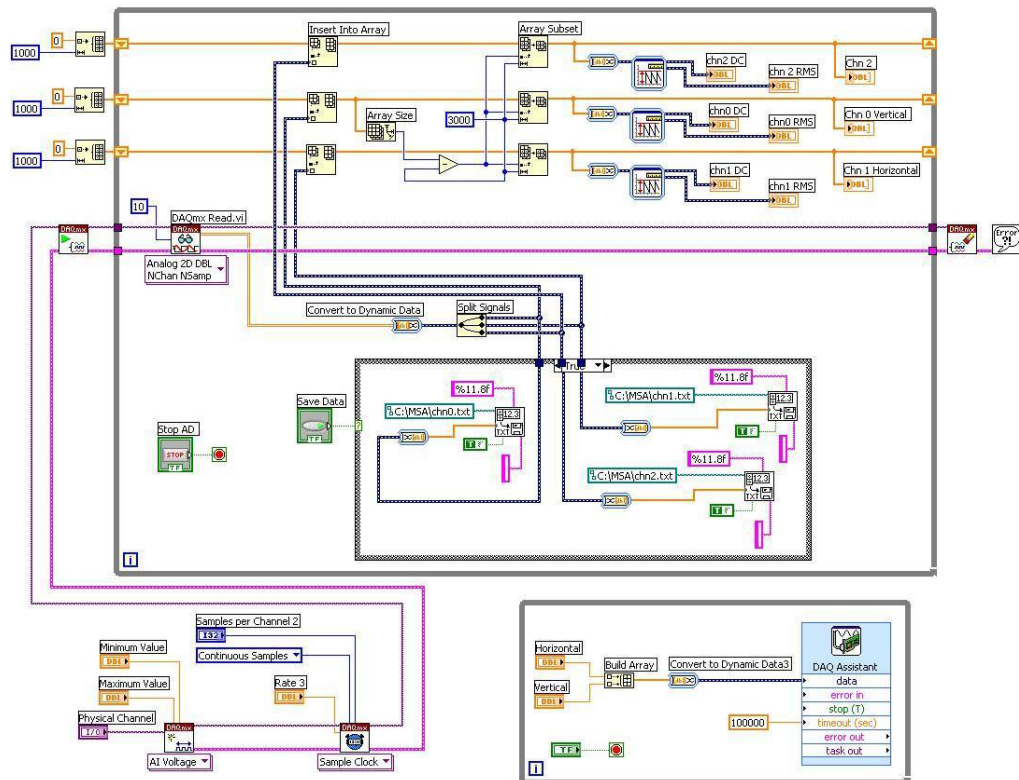
This operation program includes several functions. Firstly, the sampling rate, physical channel, minimum, maximum voltage and buffer size can be set manually before the commencement of the measurement. Secondly, the input voltage signal and the displacement of the cantilever can be displayed in real time graph. It is a valuable function for setting up the initial contact position and checking up the stability of the system.

Furthermore, by pressing “save data” button, the direct memory allocation is triggered to save the real time data, which is ready for further analysis. Finally,

obtained raw data can be analysis in self-developed Matlab program.



(a) Front panel



(b) Block diagram

Figure 3.8 Front panel and block diagram of Labview program.

3.3 Calibration of TPM system

The calibration of this system is important before using in any measurement. Failure to do this will result in unreliable outcome. The calibration of the system includes capacitive displacement sensor, force actuator and cross beam cantilever stiffness. In addition, the natural frequency of the sensing probe is investigated as well.

3.3.1 Calibration the capacitive sensor

The capacitive sensor calibration is based on loading the tip onto a digital piezo translator (AX100, Queensgate Instruments Ltd). The DPT is able to record the displacement of the tip in 1 nm resolution, meanwhile the voltage output of the capacitive is recorded as well. Consequently, the relationship between the displacement and the capacitive sensor output can be demonstrated in Figure 3.9. According to the calibration result, the sensitivity of the sensor is 148nm/mV and the R^2 value is nearly 1.

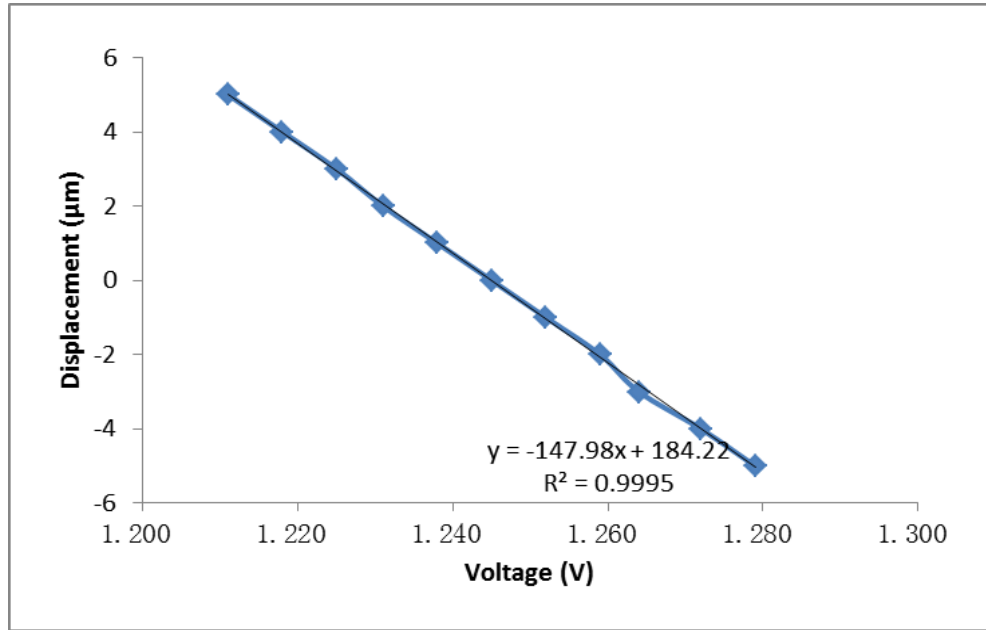


Figure 3.9 Calibration of cross beam cantilever.

3.3.2 Calibration of force actuator

The calibration of the force actuator is based on a 10g load cell (Maywood Load Beam type 49034), which has a resolution equals to 10uN. The current passed through the coil was controlled by DAQ card and increased step by step. The load cell recorded the contact force at the same time. The relationship between the voltage applied to the magnet coil and the contact force is shown in Figure 3.10. It is a perfect linear relationship with the ratio of 1.485mN/V.

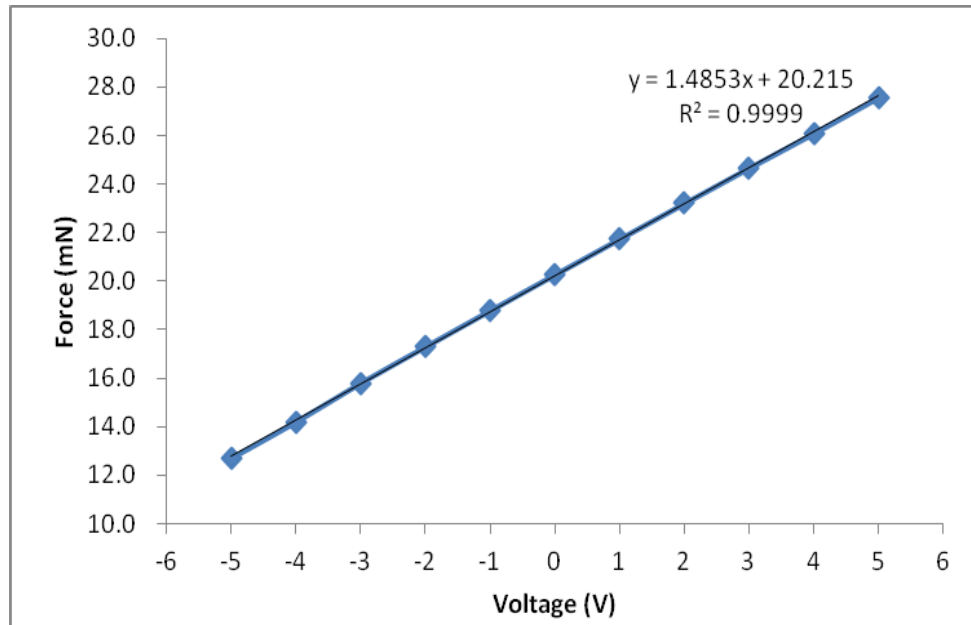


Figure 3.10 Calibration of force actuator.

3.3.3 Calibration of cross beam cantilever stiffness

The stiffness of crossbeam was calibrated based on the load cell under the tip of the probe. The calibration processes include making the probe suspended above the load cell, adjusting the coarse position screw to make the tip contact with the transducer slightly, driving the Nextline piezo down by 1 micrometer intervals and recording the contact force. A linear fit was carried on between the displacement and force. The calibration curve is shown in Figure 3.11 with a gradient of 320N/m.

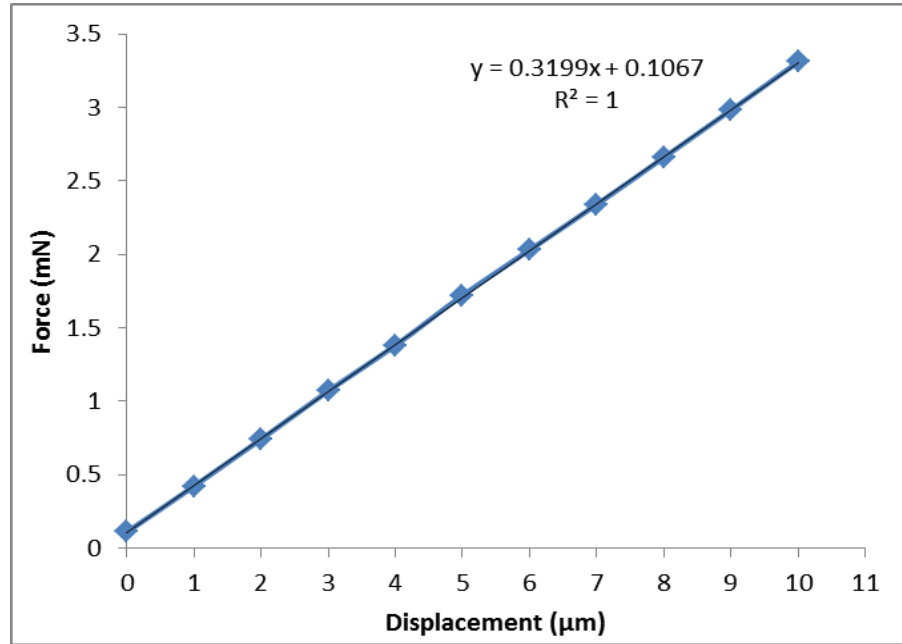


Figure 3.11 Calibration the cross beam cantilever stiffness.

3.3.4 Natural frequency of the cross beam

It is important to investigate the dynamic response of the probe, therefore, the natural frequency of the cross beam was derived in this calibration. By a hammer test of the probe the cross cantilever will impulse and vibrate from neutral position. The response of the vibration is recorded through the capacitive sensor output. The relationship between the vibration amplitude against time is shown in Figure 3.12. The corresponding power spectrum was obtained by using Fast Fourier Transform routines within Matlab. It is demonstrated that the natural frequency of the cross beam is at 158Hz.

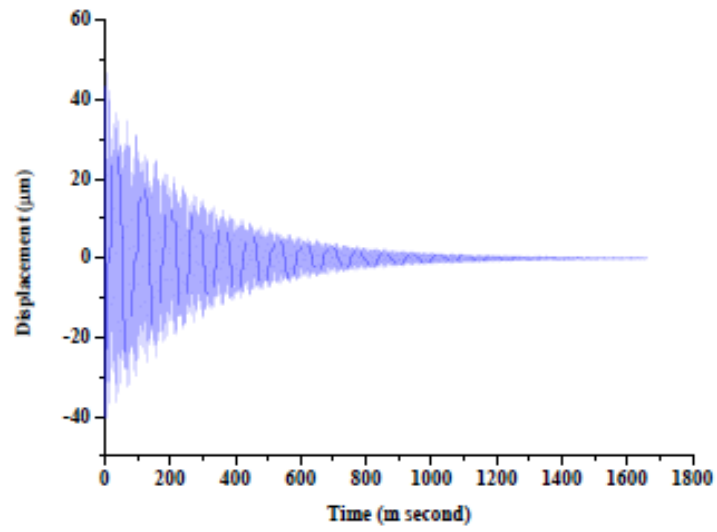


Figure 3.12 The vibration displacement of the cross beam.

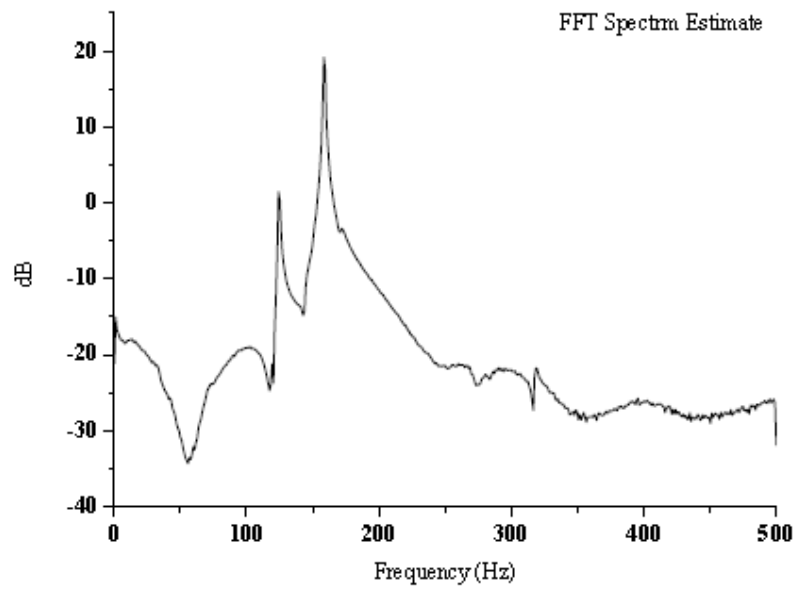


Figure 3.13 Frequency spectrum of the vibration response.

3.4 Quasi-static nanoindentation of the viscoelastic materials

The study of characterization of viscoelastic material is based on the new built TPM

facility. First of all, the samples were measured based on the traditional Oliver-Pharr method. In this part, the quasi-state nano-indentation experiment was performed. The result reveals that such method is not suitable for viscoelastic sample. As a consequence, it is necessary to characterize the viscoelastic sample through other methods.

3.4.1 Material and method

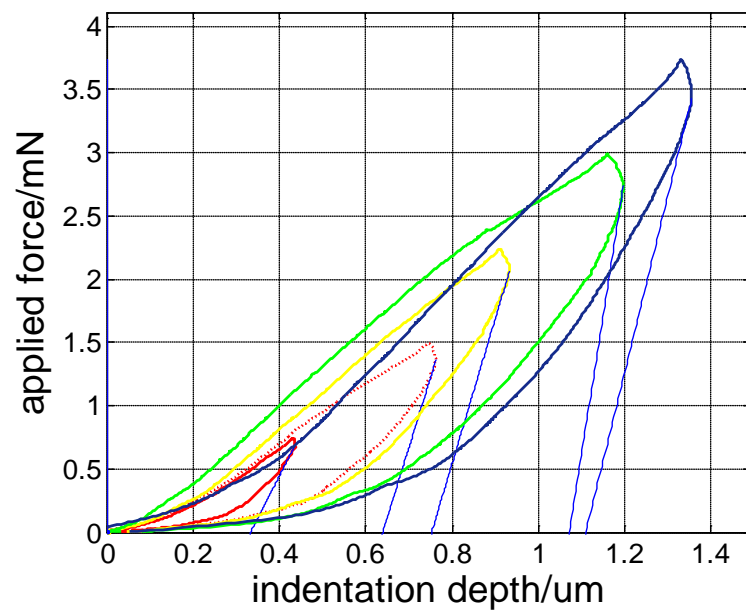
The samples of this experiment are polytetrafluoroethylene (PTFE), styrene rubber and Nitrile rubber. The preparation of these samples is minimal due to nanoindentation experiment only require the surface is smooth compared to the indentation depth. The entire size of styrene rubber samples is $150 \times 90 \text{ mm}^2$ square sheet with 5mm thickness. A $20 \times 20 \text{ mm}^2$ square was cut from the entire sheet. PTFE and Nitrile rubber were in the size of 20mm square with 5mm thickness.

To obtain the benefit of the high sensitivity and resolution of this system, the experiment environment should be avoided from any interference. It is generally believed that disturbances mainly come from two sources. First interference is from the vibration in the surroundings and another factor is temperature variation, which would result in thermal deformation of the sample and errors in the system resolution. To get a more reliable result and eliminate any potential error, the system is placed on a solid, quiet room (on the ground floor) and fixed on an anti-vibration platform. In addition, the testing system is placed in an isolated cabinet, which is constant in temperature within 1°C .

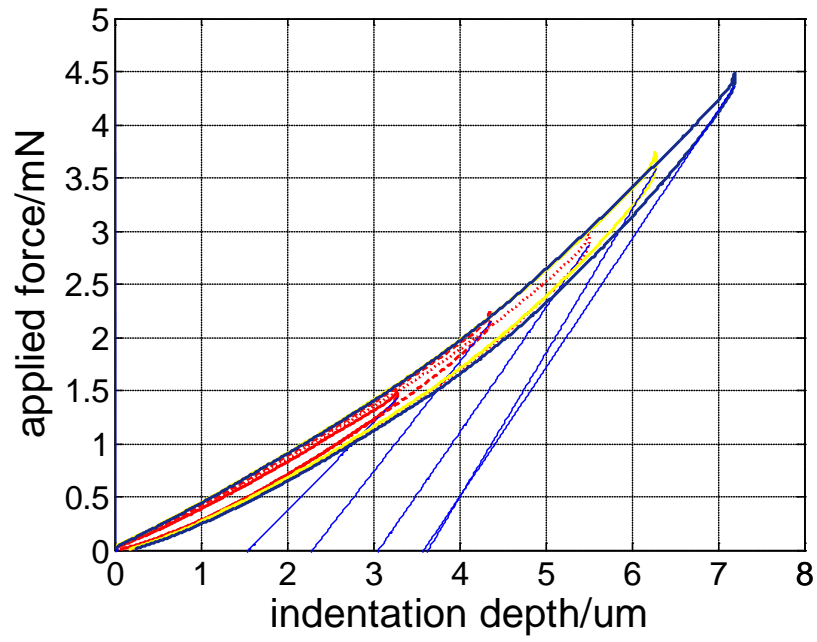
The state nanoindentation experiment was performed under different peak load ranged between 0.5 and 5mN. The loading and unloading rate of the nano-indentation is the same as $100 \mu\text{N S}^{-1}$. For each sample, the measurements were performed at five different points on its surface to ensure the widely dispersed.

3.4.2 Results and discussion

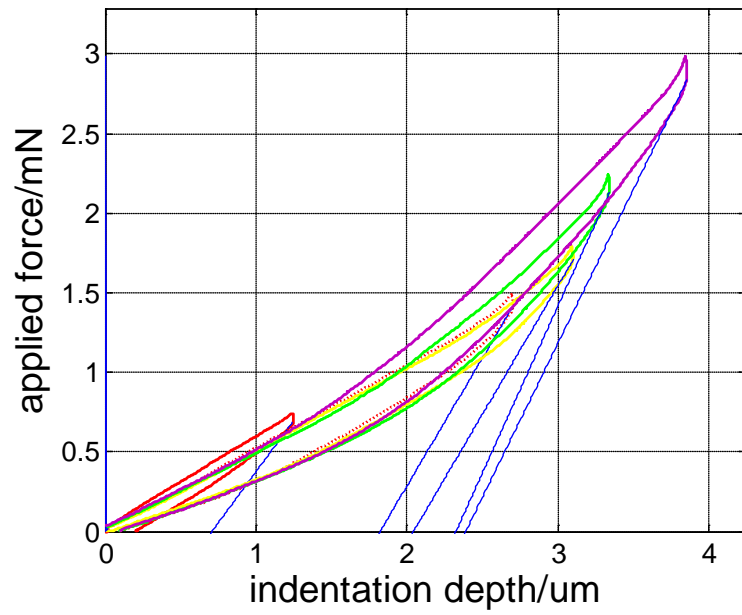
Figure 3.14 demonstrates the result of quasi-static indentation experiment. The relationship between the applied force and displacement illustrates that with the increasing of the peak force of indentation, the corresponding depth increases as well. The viscosity in these materials has a direct impact on the form of the nanoindentation curves. During the loading stage, the depth goes deeper with the increasing force. After the force reaches at the maximum value and then decreasing to zero, the depth of penetration still increases for a while. This phenomenon is most obvious in PTFE sample, the other two materials also exhibit similar respond.



(a) PTFE



(b) Styrene rubber

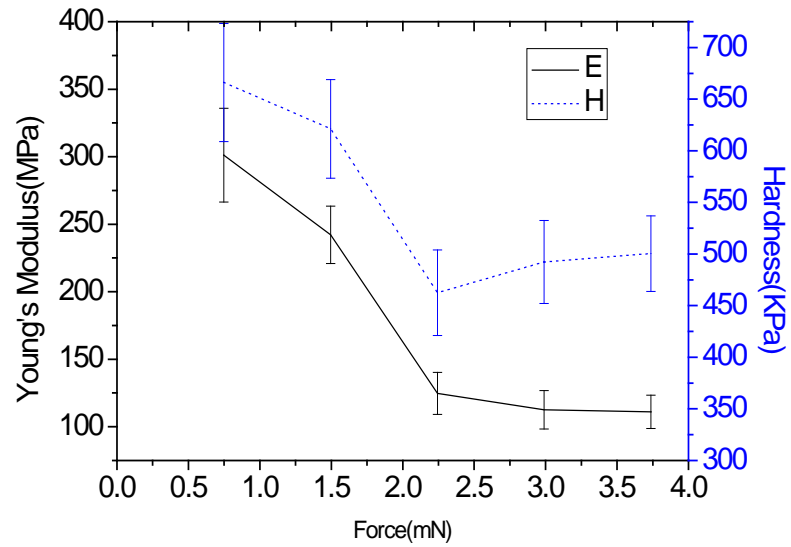


(c) Nitrile rubber

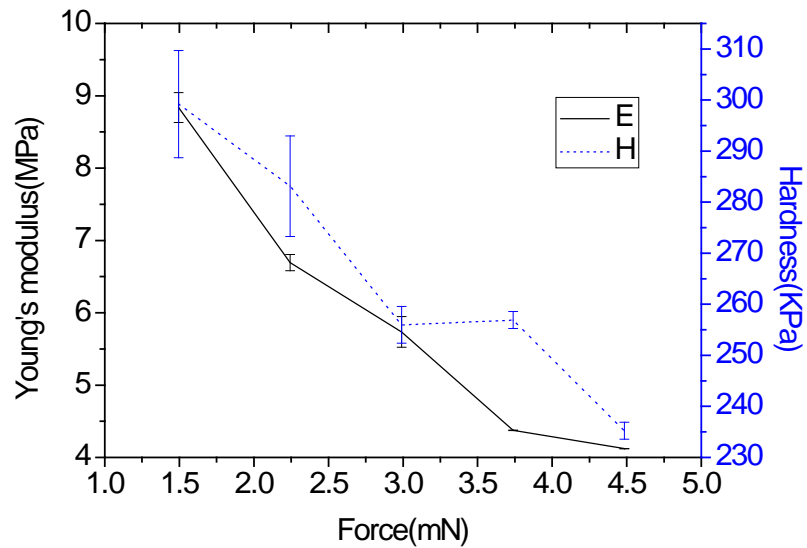
Figure 3.14 P-h curves obtained in quasi-static indentation (a) PTFE (b) Styrene rubber (c) Nitrile rubber

It is obviously in Figure 3.14 that all the P-h curves exhibit a 'nose-like' at the

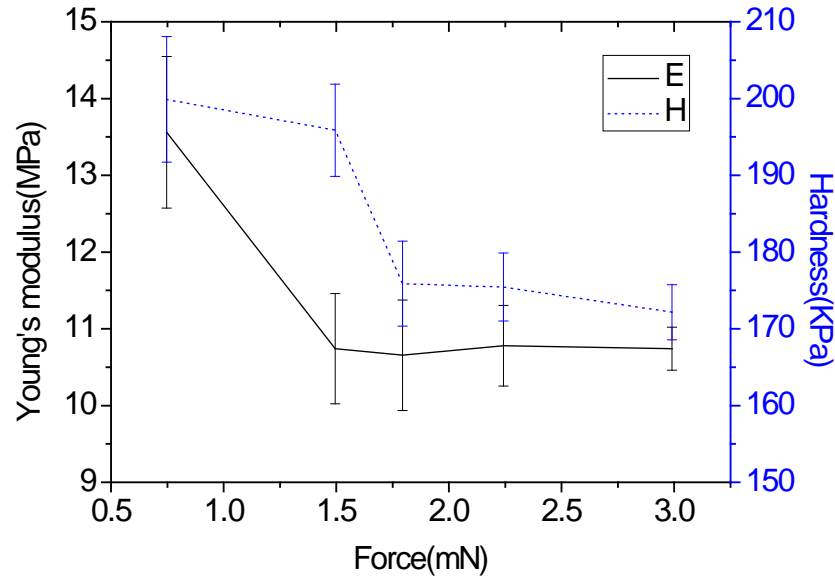
beginning of unloading profile, which will undoubtedly result in errors in deriving the mechanical properties based on the O-P method [31]. Furthermore, under the different peak force, the variable contact stiffness ($S=dP/dh$) would definitely lead to results with large error.



(a) PTFE



(b) Styrene rubber



(c) Nitrile rubber

Figure 3.15 Load size effect of quasi-static indentation (a) PTFE (b) Styrene rubber (c) Nitrile rubber

Based on the P-h curve the mechanical properties of these samples can be derived by the O-P method. These results are shown in Figure 3.15. It is found that the load size effect is significant in all three samples. The uncertainty of the result is higher at the lower depth due to the limitation to accurately determinate the area function of the indentations. Large variation in Hardness and elastic modulus of these materials are observed in Figure 3.15. Above all, it is proved that the quasi-static indentation based on the O-P method is not suitable for characterizing the viscoelastic properties of these materials. Therefore, it is necessary to pave another way to explore this issue.

3.5 Summary

In this section, an unique facility, which is designated to characterize the mechanical

properties of viscoelastic materials has been established. The detailed structure and features of this facility is shown. In addition, the calibration works has been done to guarantee the fidelity of the results. Finally, the quasi-static indentation was performed on these viscoelastic materials. The results validated the argument that standard Oliver-Pharr method is not suitable for viscoelastic samples.

Chapter 4 Dynamic nanoindentation to characterize the mechanical properties of viscoelastic materials

4.1 Introduction

Nanoindentation is one of the common techniques used for characterizing the materials' mechanical properties [67]. The general principle of testing is based on continually recording the applied force and the indentation depth during the whole stage of the process. It has successfully measured stiff and hard materials [68]. While it is still a challenge to characterize the soft material by this technique. This is due to the viscosity properties existed in these materials would impact the results of the experiment [69]. For hard materials, it is reasonable assuming that the deformation during loading and unloading is totally elastic. However, the respondent of soft material with viscosity depends not only on the applied force, but also on the loading duration, which means it is time dependent [70].

It can be approved by the work in section 3.4 that errors in mechanical properties are observed by nanoidentation experiment on viscoelastie material based on standardized test, which does not accurately describe the response of time-dependent material.

To solve this problem, nanoindentation experiment is carried out under two different schemes. The first method is within the time domain by relaxation or creep test [71].

This approach established a visco-elastic model, which is based on the viscous and elastic element in series of viscoelastic material. The loading profile is usually a trapezoidal with a holding period at peak force (creep) or depth (relaxation). Another method is using dynamic indentation within the frequency domain to measure the viscoelastic property of the material [72]. It is performed under different frequencies rather than an extended time under peak level. Generally, the dynamic method involves applying an oscillatory force to the indenter and then contact with the sample. By recording the phase lag between the applied force and corresponding response displacement. The viscous properties, such as storage modulus, loss modulus and loss factors can be obtained.

In this chapter, dynamic nanoindentation was performed to measure the viscoelastic properties of material based on the new build TPM system. It is experimental evidence that this system is able to characterize the viscoelastic material and extending its application from static indentation to dynamic mode. In addition, the success of this study pave a new way for further research about the study of the relationship between the surface topography and viscous property of bio-materials.

4.2 Theory

When the viscoelastic material is under nanoindentation experiment, the response strain of the material is not synchronized with the stress. Commonly, there exists a phase lag between the force and the corresponding response. Consequently, after the load reaches at the peak force, the deformation still increased for a while [73].

The analysis of this type of material is based on different models. The most commonly used model is a spring and a dash point element either in parallel (Voigt model) or in series (Maxwell model). Shaw and Mack might claimed that Maxwell model is more suitable for viscous fluid substance [74], while the parallel model is appropriate for the viscous solid. Therefore, in this chapter, the material is analyzed based on the Voigt model.

The elastic modulus can be divided into two sections: one is storage modulus, which shows the ability of energy storage for the material. Another one is loss modulus, which represents its capacity of dispersing the energy. Storage and loss modulus can be combined as the complex modulus (E^*). The relationship between storage and loss modulus is loss factor.

For a viscoelastic sample under an oscillation loading profile, the relationship between the stress and strain can be demonstrated as [64],

$$\sigma = \varepsilon_0 E' \sin \omega t + \varepsilon_0 E'' \cos \omega t \quad (4-1)$$

where σ is stress, ε_0 is the amplitude of strain, ω is the frequency of the oscillation force, t is the time. The storage and loss modulus can be expressed as:

$$E' = \frac{\sigma_0}{\varepsilon_0} \cos \phi \quad (4-2)$$

$$E'' = \frac{\sigma_0}{\varepsilon_0} \sin \phi \quad (4-3)$$

Where σ_0 is the amplitude of stress, ϕ is the phase lag between stress and strain.

Analysis of viscoelastic properties by writing the relationship among stress, strain and time in the forms of :

$$\sigma = \sigma_0 e^{i\omega t} \quad (4-4)$$

$$\varepsilon = \varepsilon_0 e^{i(\omega t + \phi)} \quad (4-5)$$

Taking the ratio between stress and strain

$$\frac{\sigma}{\varepsilon} = \frac{\sigma_0}{\varepsilon_0} e^{i\phi} = E^* \quad (4-6)$$

The schematic of a simple dynamic model of the nanoindentation facility without any sample is shown in Fig 4.1 [75], which includes three parts: spring stiffness (K), dash pot (D) and mass (m).

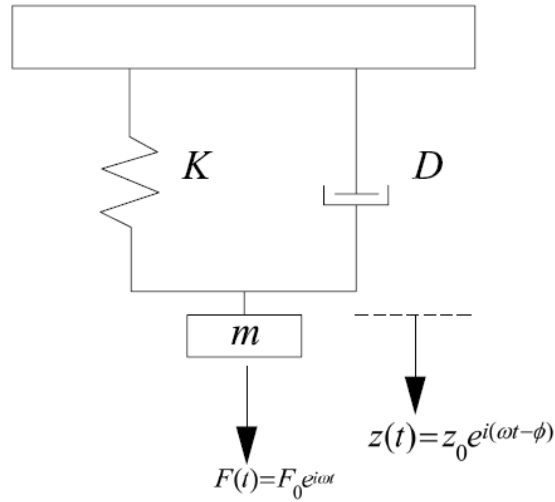


Figure 4.1 Simple-harmonic oscillator model

When the system is excited under an oscillation load $F(t) = F_0 e^{i\omega t}$, the response displacement should be $z(t) = z_0 e^{i(\omega t - \phi)}$, which means the vibration of the mass is under the same frequency ω , while lag by a phase angle ϕ .

The relationship between the applied force and the displacement response can be illustrated in Equation (4-7).

$$m\ddot{z}(t) + D\dot{z}(t) + Kz(t) = F(t) \quad (4-7)$$

Taking the first and second derivation of $z(t)$ to get z' and z'' , substitute z , z' , z'' and F to Equation (4-7):

$$-m\omega^2 + iD\omega + K = \frac{F_0}{z_0} e^{i\phi} = \frac{F_0}{z_0} (\cos \phi + i \sin \phi) \quad (4-8)$$

Equating the real and imaginary parts of (4-8) yields:

$$K - m\omega^2 = \frac{F_0}{z_0} \cos \phi \quad (4-9)$$

$$D\omega = \frac{F_0}{z_0} \sin \phi \quad (4-10)$$

Consequently, the phase angle ϕ is under the function of other parameters:

$$\tan \phi = \frac{D\omega}{K - m\omega^2} \quad (4-11)$$

When there is no sample fixed in the test, the components of the model are:

$K = K_i$, $m = m_i$ and $D = D_i$. K_i is the spring stiffness supporting the indenter. The majority contribution to D_i is from the capacitive plate. m_i is the weight of indenter shaft. By combination Equation (4-9) and (4-10), it can derive:

$$K_i - m_i\omega^2 = \frac{F_0}{z_0} \cos \phi \Big|_{free-hanging} \quad (4-12)$$

$$D_i\omega = \frac{F_0}{z_0} \sin \phi \Big|_{free-hanging} \quad (4-13)$$

When the tip is in contact with the specimen, the schematic of the model is illustrated in Figure 4.2. K_c and D_c represent the contact stiffness and damping, respectively. The stiffness of the system in Figure 4.2 can be expressed by two springs in parallel:

$$(K_i + K_c) - m\omega^2 = \frac{F_0}{z_0} \cos \phi \Big|_{contact} \quad (4-14)$$

Similarly, the damping is established:

$$(D_i + D_c)\omega = \frac{F_0}{z_0} \sin \phi|_{\text{contact}} \quad (4-15)$$

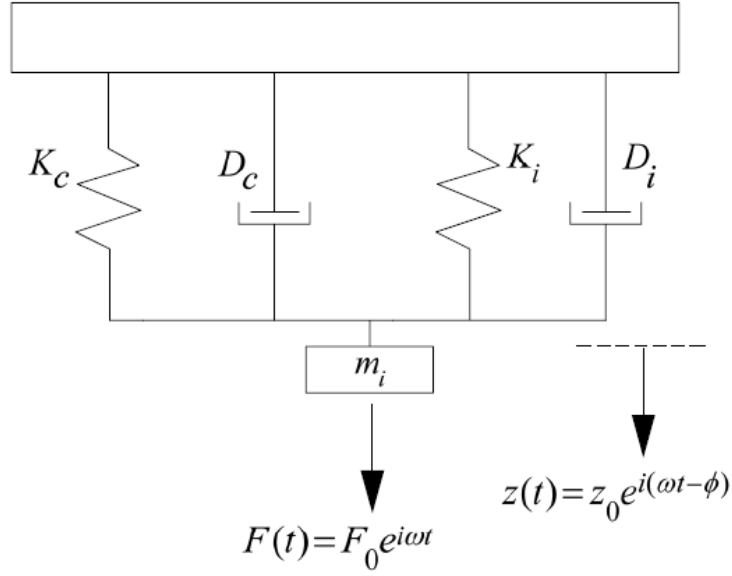


Figure 4.2 Model accommodates both instrument and sample in contact

Consequently, subtract Equation (4-12) from (4-14), (4-13) from (4-15), it can obtain:

$$K_c = \frac{F_0}{z_0} \cos \phi|_{\text{contact}} - \frac{F_0}{z_0} \cos \phi|_{\text{free-hanging}} \quad (4-16)$$

$$D_c \omega = \frac{F_0}{z_0} \sin \phi|_{\text{contact}} - \frac{F_0}{z_0} \sin \phi|_{\text{free-hanging}} \quad (4-17)$$

From the Equation (4-16) and (4-17), it is obvious that the contact stiffness and damping are independent of the mass of the tip. It is necessary to accurately assess the dynamic response of the system prior to the dynamic nanoindentation experiment.

The storage modulus E' , loss modulus E'' and loss factor $\tan \delta$ can be calculated as the functions below:

$$E' = \frac{\sqrt{\pi}}{2} \frac{K_c}{\sqrt{A}} \quad (4-18)$$

$$E'' = \frac{\sqrt{\pi}}{2} \frac{\omega D_c}{\sqrt{A}} \quad (4-19)$$

$$\tan \delta = \frac{E''}{E'} = \frac{\omega D_c}{K_c} \quad (4-20)$$

Where A is the contact area, which is calculated based on the geometry of the spherical tip:

$$A = \pi(2R_i h_c - h_c^2) \approx 2\pi R_i h_c \quad (4-21)$$

Where h_c is the depth of the equilibrium position, R_i is the radius of the spherical tip.

4.3 Experiment Method

The dynamic nanoindentation experiment is performed on the system, which is detailed introduced in Chapter 3. The sample selection is the same as the quasi-static indentation experiment in Section 3.4. More specifically, in the dynamic test, an oscillating force with constant amplitude and frequency was applied to the sample, and the depth of penetration was recorded at the same time. The objective of this study is to get the storage modulus, loss modulus and loss factor under different frequency. It is important to emphasize that the reliable result of dynamic nanoindentation depends on accurately determine the response of the instrumentation under or close to the same condition. Therefore, it is necessary to measure the phase angle and instrument stiffness K_i and D_i damping against the frequency without sample under investigation.

The relationship between the phase angle against a set of frequency is shown in Figure 4.3. The result is plotted according to the average value of five measurements, and standard deviation is exhibited by the error bar in the graph. From the result, it is obvious that the phase angle increases with the frequency from 1 to 10 Hz.

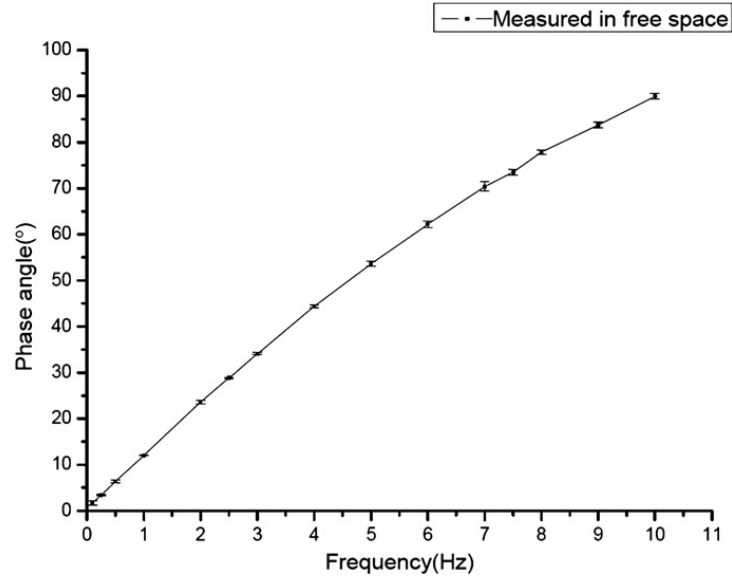


Figure 4.3 The phase angle as a function of frequency, measured with indenter tip hanging in free space

By positioning the tip at the location, which the main experiment will take place, the instrument stiffness K_i and damping D_i were obtained based on the known phase angle using Equation (4-12) and (4-13). The calculated stiffness and damping of the system under frequency of 1, 3, 5, 7.5 and 10 Hz will be used to characterize the viscoelastic properties of the sample.

The result in Figure 4.4 demonstrates that the stiffness decreases against the frequency from 1 to 10 Hz, while the damping of the system increases under the same frequency range.

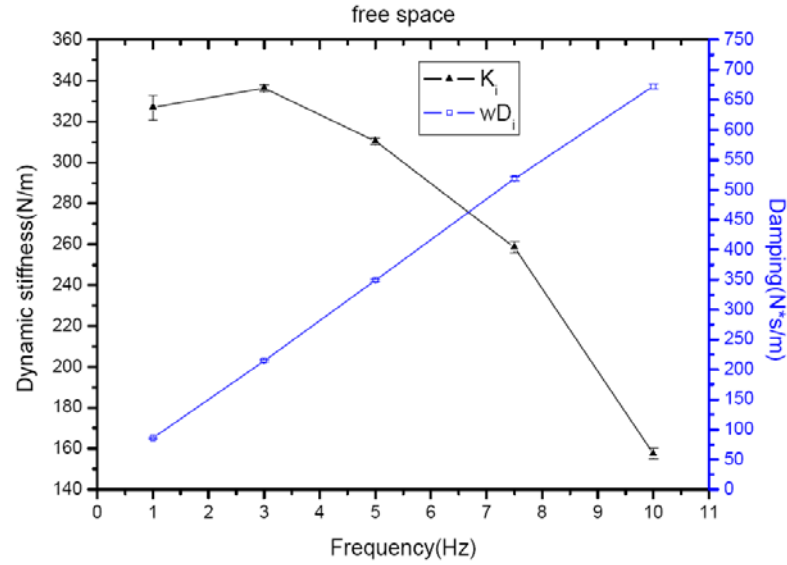


Figure 4.4 Dynamic stiffness and damping of indentation system as a function of frequency measured in free space

At the beginning of the dynamic nanoindentation, the sample is fixed on the platform and the spherical tip is controlled moving down to the surface until it contacts with the sample's surface. After that, a static force of 1 mN is loaded on the tip and kept at this level. Then, a small sinusoidal force with 1uN amplitude is added to the static force under a specific frequency between 1 and 10 Hz. The applied force and the corresponding displacement are recorded at the same time by the system. The response of displacement is the combined contributions from the instrument and the sample. As a consequent, the contribution of the system has eliminated from the aggregate result. The dynamic parameters of the system are obtained and the values are shown in Figures 4.3 and 4.4. Under each frequency, five indentations were carried out to eliminate the potential errors. The storage, loss modulus and loss factor can be worked out based on equations (4-16) to (4-20).

4.4 Results and discussions

The applied oscillation force and the corresponding displacement against time is shown in Figure 4.5. It is obvious that although the force and depth is under the same frequency, there is a phase lag between them. Based on the theory in section 4.2, the complex modulus can be calculated. Storage modulus represents the capability of viscoelastic material to store energy. Loss modulus exhibits the ability of dissipating energy. The behavior of viscoelastic material is indicated by the ratio between loss modulus and storage modulus. When the loss factor is zero, it reveals that the material is pure elastic with no viscous element. The higher loss factor value, the more viscous factor exists in the material. In addition, it is interesting to note that these three parameters are independent of the contact area between the tip and sample.

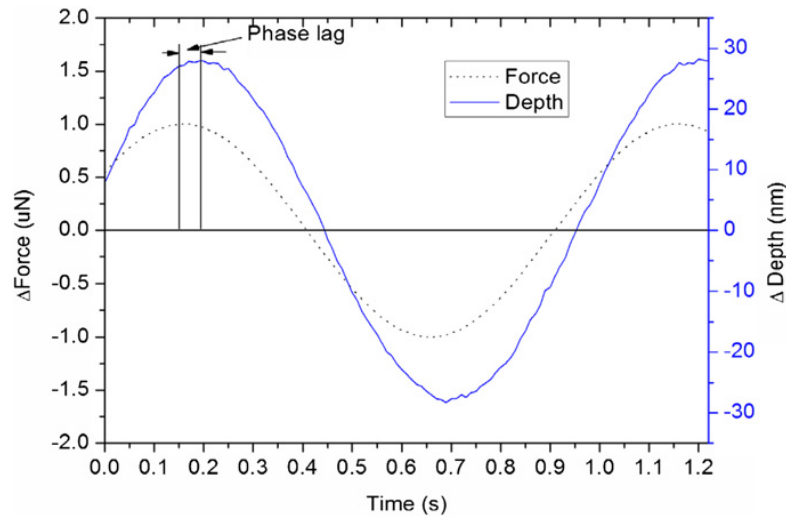
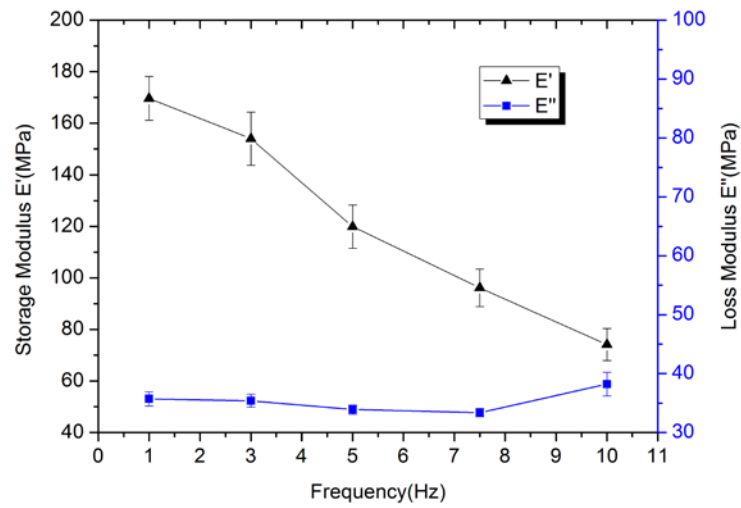


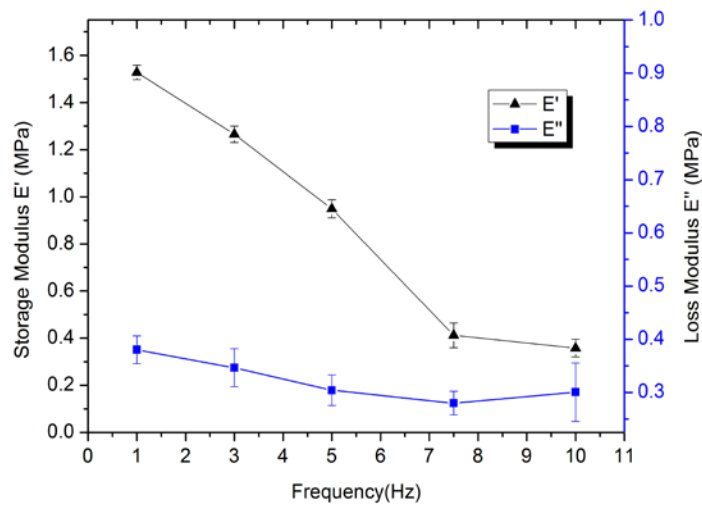
Figure 4.5 The displacement and force modulation in dynamic indentation

The relationship between storage modulus, loss modulus and frequency of all three samples are shown in Figure 4.6. The standard deviation is indicated by the error bar

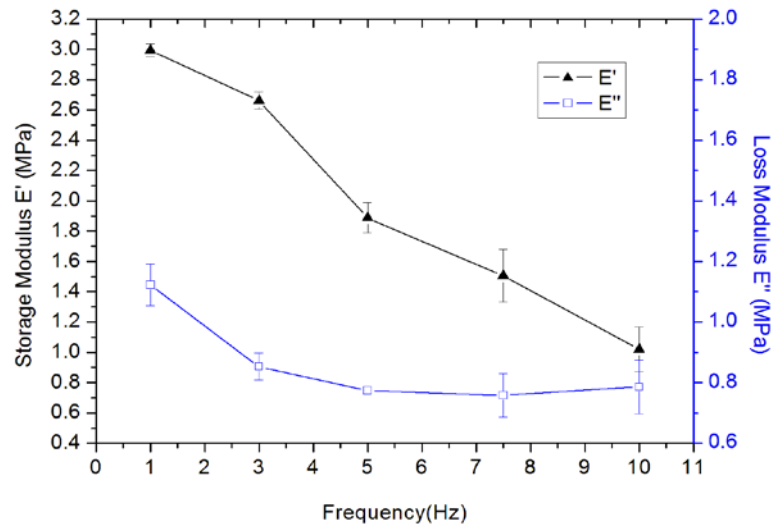
in the graph. It is found that storage modulus decrease over the frequency from 1 to 10 Hz. While the loss modulus is less dependent on the frequency than storage modulus. The small fluctuation in loss modulus indicates a variation of damping capacity of the material in this domain. The regulation of storage and loss modulus of viscoelastic material is similar to other researchers' work [64], which demonstrate the storage modulus decrease against the frequency from 1 to 10 Hz, while the value of loss modulus do not fluctuate very much.



(a) PTFE



(b) Styrene rubber



(c) Nitrile rubber

Figure 4.6 Storage and loss modulus as a function of frequency (a) PTFE (b) Styrene rubber (c) Nitrile rubber

Figure 4.7 demonstrates the relationship between the loss factor and the frequency for all three samples. Approaching peak values in loss factor indicate phase transition will happen in the material. In figure 4.7, it shows that the loss factor increases with the frequency between 1 to 10 Hz, which means the samples are approaching the softening of the amorphous phase.

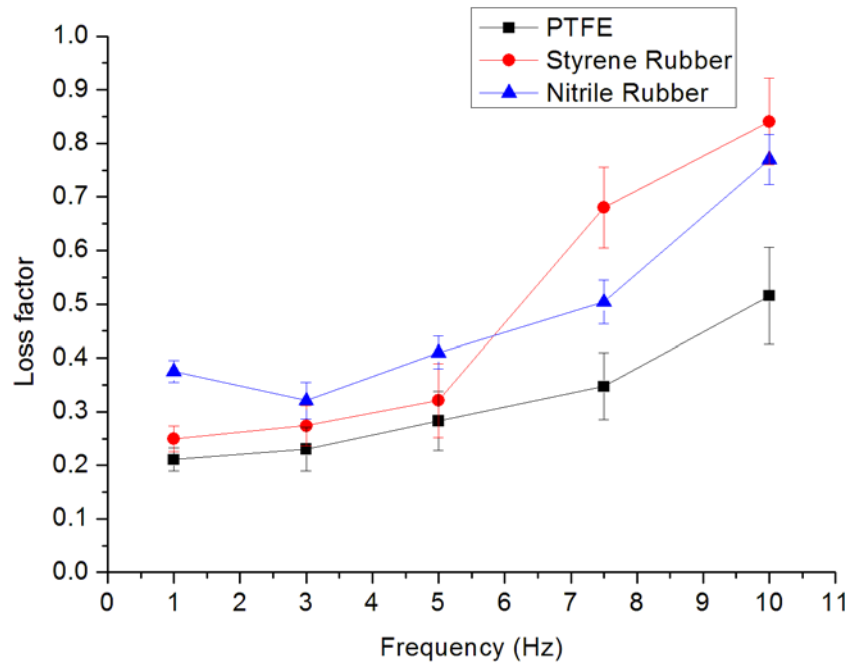


Figure 4.7 Loss factor as a function of frequency

Compared to the quasi-static nanoindentation study in Section 3.4, dynamic indentation is more suitable for characterizing viscoelastic material and offers more viscous information. Moreover, this study shows the capability of TPM to measure the complex modulus of viscoelastic material. The technique presented here can be implemented in other viscoelastic materials such as nature biomaterial or biomimetic materials.

4.5 Summary

The mechanical properties of viscoelastic materials were obtained by dynamic indentation based on home made facility. Experiments were carried out on the materials of PTFE, styrene rubber and nitrile rubber. The experimentation results show

that dynamic nanoindentation is a suitable technique for exploring the time dependent properties of these materials. The viscoelastic properties including storage, loss modulus and loss factor were derived. The results revealed that these three parameters do not independent of the loading frequency. The variation of the loading frequency would result in significant changes in the measured result. Compared to the results obtained from quasi-static indentation dynamic approach is able to offer more rich-full viscous information. Overall, we have demonstrated the capability of our home-made facility to characterize the viscoelastic materials via dynamic indentation.

Chapter 5 Characterization of viscoelastic materials based on spherical indentation of creep-load control

5.1 Introduction

Nanoindentation, also known as depth-sensing indentation (DSI), is a modern test method that is able to measure some important mechanical properties [76]. Stemming from traditional contact testing techniques, nanoindentation is not only suitable for measuring bulk metals in macro dimension, but capable of exploring a variety types of materials measuring in small volumes and shallow depth in nanometer resolution or less [77]. In this technique, applying a function of load ranging between several micronewtons and several newtons to a relatively hard tip, which is pressed into the sample under the penetration depths between a few nanometers to millimeters, it had successfully measured the elastic-plastic material by analyzing the force-depth curve of the whole loading-unloading process [78]. The benefits of depth-sensing indentation are in two folds [79]. First of all, the high resolution in force and depth enable this method is ideal for probing the microcosm of the material property. In the second place, another advantage of nanoindentation is that the sample preparation is minimal prior to the experiment, when compared to other methods such as tensile test.

It was not uncommon that extension of the measuring properties from elastic-plastic materials to viscoelastic materials, which include polymers and

biomaterials [80]. However, the standard Oliver-Pharr method for elastic-plastic analysis is inappropriate for viscoelastic behaviors [81]. It means that more attention and effort were devoted to characterize the materials with time-dependent property. For materials with elastic-plastic properties, such as metals and ceramic, the depth of penetration occurs synchronously with the applying force. When testing the viscoelastic material, the occurrence of deformation would not be simultaneously with the loading. For instance, the deformation changes slower than indentation force [82].

Quite a few numbers of investigations have been performed to measure the time-dependent property of viscoelastic materials. To sum up, these approaches are divided into two different categories. The first type of method is based on the oscillation of the indenter to contact with sample over a range of different frequencies [83, 84]. The dynamic properties of viscoelastic material, such as storage modulus, loss modulus and loss factor can be derived from this technique. Alternatively, one can carry out the nanoindentation experiment by creep method or relaxation method, which implements a rapid force ramping prior to a constant load (creep) or displacement (relaxation) holding period to explore the time-dependent property of the sample [85, 86]. This creep or relaxation phenomenon depends on the rate and duration time of the applying force. This technique can be implemented by Boltzmann integral operators to explore the time-dependent behavior [87].

When it comes to the commercial nanoindenters, these instruments have optimized the testing method of elastic-plastic materials. However, it is obviously that such results are not accurate for polymers or biomaterials due to the potential

time-dependent properties exhibiting during the test. As a consequent, simply placing a polymer under a commercial instrument and pressing start, then waiting for the results which are automatically derived by the embedded software of the instrument would result in incorrect results with large errors [88].

There is a growing demand for characterization of polymeric materials, which often exhibit viscoelastic properties. The motivation of this study is driven by several reasons in the industry. First of all, better quality, more reliable and long life products play an important part in the successful of manufacturing industry. Secondly, it is important to control the risk of product failure or safety critical applications. Moreover, in the application of polymeric micro-moldings, it is necessary to get high resolution viscoelastic property of dispersion particle.

To make contribution in this area, a new improved facility, TPM (Tribological Probe Microscopy) has been established [88]. It owns not only the previous function of obtaining topography, hardness, elastic modulus for hard sample, but the ability to characterize the mechanical properties for viscoelastic materials. The details of establishment and calibration of this system is presented in Chapter 3.

In this chapter, after brief explanation the solutions for creep indentation at constant load after ramp loading frame, this investigation focused on the experimental technique for nano-indentation on the viscoelastic mechanical behaviors under the force control function of TPM. A direct analysis was considered for different loading conditions based on a curve fitting progress that used to work out viscoelastic parameters. According to this, it is not difficult to derive the instant and infinite elastic

modulus of the samples. The mechanical property of viscoelastic material measured by dynamic indentation method is shown in Chapter 4. The results obtained from creep nanoindentation method are compared to the dynamic results. This comparison demonstrates that it is necessary to establish more complex model to bridge the gap between these two methods.

5.2 Theoretical approach of creep indentation

During nanoindentation, the response of viscoelastic material depends not only on the value of indentation force, but also on its durations [89]. Under this circumstance, elastic modulus is not a constant value, which is varied according to time $E = E(t)$, due to the response is not simultaneous to indentation force.

The relationship between the penetration depths and other experiment parameters for viscoelastic indentation can be expressed as

$$h^m(t) = K \cdot f(F, J, t) \quad (5-1)$$

Where m and K are the function of the indenter shape. For spherical tip, $m = 1.5$, $K = 3 / (8\sqrt{R})$, for conical or Berkovich tip, $m = 2$, $K = \pi / (4 \tan \alpha)$. Here, R is the radius of spherical tip, α is the semi-angle of the indenter tip. $f(F, J, t)$ demonstrates that when the shape of the tip is confirmed, the penetration depth depends on the combined functions of the load amplitude F , creep compliance J and the loading history t .

Consequently, for spherical indentation, the governing equation is expressed as below

$$h^{3/2}(t) = \frac{3}{8\sqrt{R}} \cdot f(F, J, t) \quad (5-2)$$

The function f for the indentation of a rigid tip into a viscoelastic material can be replaced by a viscoelastic hereditary integral operator for creep [86],

$$f(F, J, t) = \int_0^t J(t-u) \frac{dF}{du} du \quad (5-3)$$

Substitution Equations. (5-3) to (5-2), it can be derived

$$h^{3/2}(t) = \frac{3}{8\sqrt{R}} \cdot \int_0^t J(t-u) \frac{dF}{du} du \quad (5-4)$$

For a ramp loading at a constant load rate, $k = dF / dt$ from zero load to F_{\max} ,

$$f(t) = k \int_0^t J(t-u) du \quad (5-5)$$

For constant force after ramping load, the relationship is

$$f(t) = F \cdot J(t) \quad (5-6)$$

Consequently, for the constant loading after ramping from 0 to F_{\max} at the loading rate $k = F_{\max} / t_R$ (t_R is rising time), the loading conditions are

$$F(t) = kt, \quad 0 \leq t \leq t_R \quad (5-7)$$

$$F(t) = F_{\max} = k \cdot t_R, \quad t \geq t_R \quad (5-8)$$

Therefore, the solution for Equations. (5-4) under the above load profile is

$$h^{3/2}(t) = \frac{3}{8\sqrt{R}} \cdot \int_0^t J(t-u) k du, \quad 0 \leq t \leq t_R \quad (5-9)$$

$$h^{3/2}(t) = \frac{3}{8\sqrt{R}} \cdot \int_0^{t_R} J(t-u) k du, \quad t \geq t_R \quad (5-10)$$

The creep function $J(t)$ of viscoelastic material is formed by a spring in series with one or more Kelvin-Voigt element. The solutions to these integral equations are

$$J(t) = C_0 - \sum_{i=1}^j C_i \exp\left(-\frac{t}{\tau_i}\right) \quad (5-11)$$

The solutions for Equations. (5-9) and (5-10) substituted by Equations. (5-11) are

$$h^{3/2}(t) = \frac{3k}{8\sqrt{R}} \left\{ C_0 t - \sum C_i \tau_i \left[1 - \exp\left(-\frac{t}{\tau_i}\right) \right] \right\}, \quad 0 \leq t \leq t_R \quad (5-12)$$

$$h^{3/2}(t) = \frac{3k}{8\sqrt{R}} \cdot \left\{ C_0 t_R - \sum C_i \tau_i \exp\left(-\frac{t}{\tau_i}\right) \left[\exp\left(\frac{t_R}{\tau_i}\right) - 1 \right] \right\}, \quad t \geq t_R \quad (5-13)$$

By fitting Eqs. (5-13) to the depth-time curve obtained during the holding period of the creep indentation, the time-dependent parameters (C_i, τ_i) can be worked out.

The general creep function is related to the shear modulus, therefore, the instantaneous shear modulus is

$$G_0 = \frac{1}{2J(0)} = \frac{1}{2(C_0 - \sum C_i)} \quad (5-14)$$

Similarly, the infinite shear modulus is

$$G_\infty = \frac{1}{2J(\infty)} = \frac{1}{2C_0} \quad (5-15)$$

The relationship among shear modulus (G), elastic modulus (E) and Poisson ratio (ν) is

$$E = 2G(1 + \nu) \quad (5-16)$$

Based on above solutions, the instantaneous (E_0) and infinite elastic modulus (E_∞) can be derived.

The dynamic parameters including storage (E') and loss modulus (E'') can be calculated according to the analysis below. One element of Voigt model used in this

chapter can be shown in Figure 5.1, which consists of a modulus of E_1^* in series with an element including a modulus E_2^* and a viscosity dashpot η in parallel.

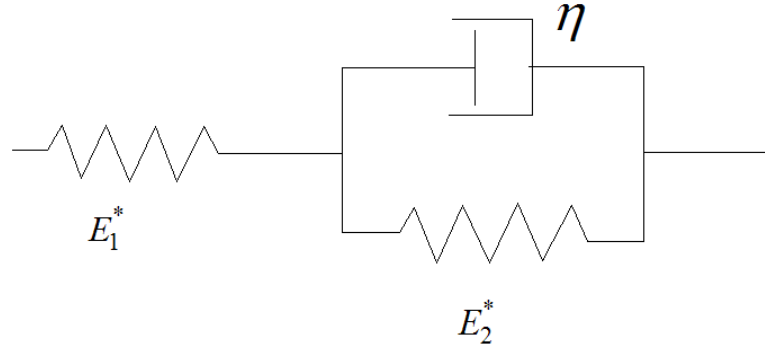


Figure 5.1 Schematic of Voigt model

When the model is under loading condition, the force in spring E_1^* is F_1 , with the corresponding displacement of x_1 . Similarly, F_2 and F_3 represent the force of E_2^* and η , respectively. The displacement of E_2^* and η are x_2 and x_3 . The combination of total force is F_T with the whole displacement of x_T . Their relationship can demonstrate as

$$F_1 = E_1^* \cdot x_1 \quad (5-17)$$

$$F_2 = E_2^* \cdot x_2 \quad (5-18)$$

$$F_3 = \eta \cdot \dot{x}_3 \quad (5-19)$$

$$F_1 = F_2 + F_3 \quad (5-20)$$

$$x_2 = x_3 \quad (5-21)$$

$$F_T = F_1 \quad (5-22)$$

$$x_T = x_1 + x_3 \quad (5-23)$$

Based on Equation (5-17) to (5-22), it can derive that

$$F_T = E_1^* \cdot x \quad (5-24)$$

$$F_T = E_2^* \cdot x_3 + \eta \cdot \dot{x}_3 \quad (5-25)$$

$$x_T = x_1 + x_3 \quad (5-26)$$

Using Equation (5-24) to eliminate x_1 gives

$$x_T = \frac{F_T}{E_1^*} + x_3 \quad (5-27)$$

Elimination in the Equation (5-25) gives

$$F_T = E_2^* \left(x_T - \frac{F_T}{E_1^*} \right) + \eta \left(\dot{x}_T - \frac{\dot{F}_T}{E_1^*} \right) \quad (5-28)$$

Equation (5-28) can be converted to

$$\left(1 + \frac{E_2^*}{E_1^*} \right) F_T + \frac{\eta}{E_1^*} \dot{F}_T = E_2^* x_T + \eta \dot{x}_T \quad (5-29)$$

To get the complex modulus with the function of the parameters of E_1^* , E_2^* when under a harmonic force, it is convenient to define several constants as below:

$$\tau = \frac{\eta}{E_1^*} \dot{F}_T \quad (5-30)$$

$$\mu = 1 + \frac{E_2^*}{E_1^*} \quad (5-31)$$

Therefore,

$$E_1^* = \frac{E_2^*}{\mu - 1} \quad (5-32)$$

$$\eta = \tau E_1^* = \frac{\tau E_2^*}{\mu - 1} \quad (5-33)$$

Substituting Equation (5-30) to (5-33) into Equation (5-29), it gets

$$\mu F_T + \tau \dot{F}_T = E_2^* x_T + \frac{\tau E_2^*}{\mu - 1} \dot{x}_T \quad (5-34)$$

If F_T and x_T undergo harmonic vibration against time under the same frequency, ω the above equation will become:

$$(\mu + i\omega\tau)F_T = (E_2^* + \frac{i\omega\tau E_2^*}{\mu - 1})x_T = \frac{E_2^*(\mu - 1) + i\omega\tau E_2^*}{\mu - 1}x_T \quad (5-35)$$

Therefore,

$$F_T = \frac{E_2^*(\mu(\mu - 1) + \omega^2\tau^2) + i\omega\tau E_2^*}{(\mu - 1)(\mu^2 + \omega^2\tau^2)}x_T \quad (5-36)$$

Consequently, the real and imaginary parts of complex modulus E' and E'' are

$$E' = \frac{E_2^*(\mu(\mu - 1) + \omega^2\tau^2)}{(\mu - 1)(\mu^2 + \omega^2\tau^2)}x_T \quad (5-37)$$

$$E'' = \frac{\omega\tau E_2^*}{(\mu - 1)(\mu^2 + \omega^2\tau^2)}x_T \quad (5-38)$$

When $t = 0$,

$$J(0) = \frac{1}{E_1^*} = C_0 - C_1 \quad (5-39)$$

When $t = \infty$,

$$J(0) = \frac{1}{E_1^*} + \frac{1}{E_2^*} = C_0 \quad (5-40)$$

Based on the above parameters of and, the storage and loss modulus can be worked out according to Equation (5-37) and (5-38).

5.3 Experiment and materials

The nanoindentation experiments for creep analysis were performed using the home-made facility TPM with a spherical tip and a high resolution X-Y-Z stage platform. The system schematic is shown in Figure 5.2.

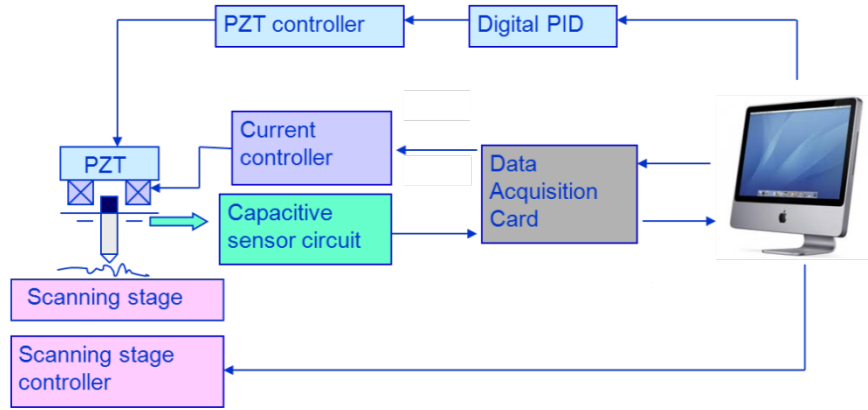


Figure 5.2 The schematic of TPM system.

The tested materials were PTFE and styrene rubber, which were purchased from the vendor in the form of a square sheet of 15 cm×9 cm with 5 mm thickness. Pieces of 20×20 mm² square sheets were cut down from the original sheet. Extra preparation prior to the experiment was minimal due to the surface condition is flat and smooth enough for measurement.

The nanoindentation experiments were performed under a three stage (loading, holding, unloading) trapezoidal loading profile. More specifically, the force-control indentation includes 20 seconds rising time (t_r) at a constant ramping rate followed by a 20 seconds holding period under constant peak force. Finally, the force decreased to 0 in 20 seconds.

Each sample was tested under different peak load level ranged from 0.75 mN to 4.5 mN. For each testing parameter, five indentations were repeated to reduce the potential errors in the result. After the test, the displacement-time creep data was fitted to the solution in Equations (5-13) using the curve fitting tool in Matlab. The parameter (C_i, τ_i) can be used to calculate the viscoelastic properties of these

samples.

5.4 Results

The load-displacement curve of PTFE indentation at 1.5 mN peak load is shown in Figure 5.3, it is obvious that sample exhibits time-dependent behaviors during the whole indentation process. In addition, the experimental depth-time curves during the holding periods are illustrated in Figure 5.4. As it can be found in this figure that the creep behavior increased obviously at the beginning stage of holding and slowly became a steady value after a while.

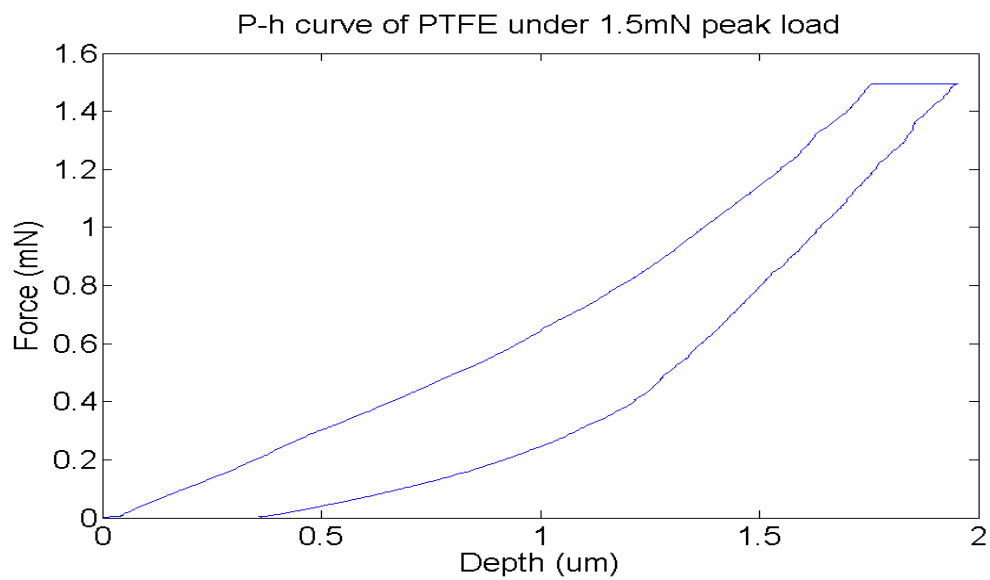
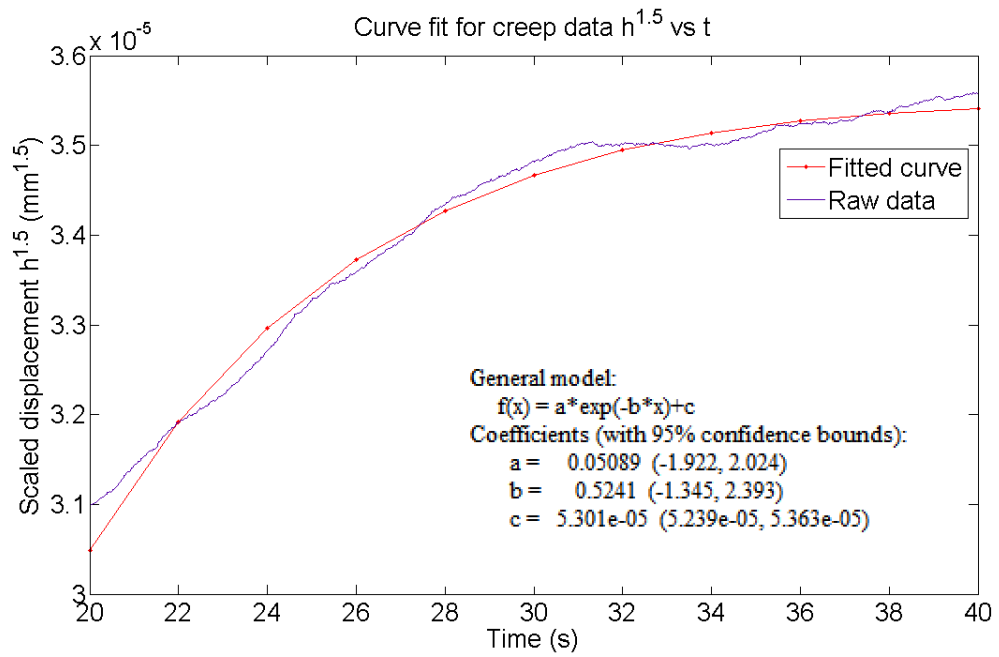
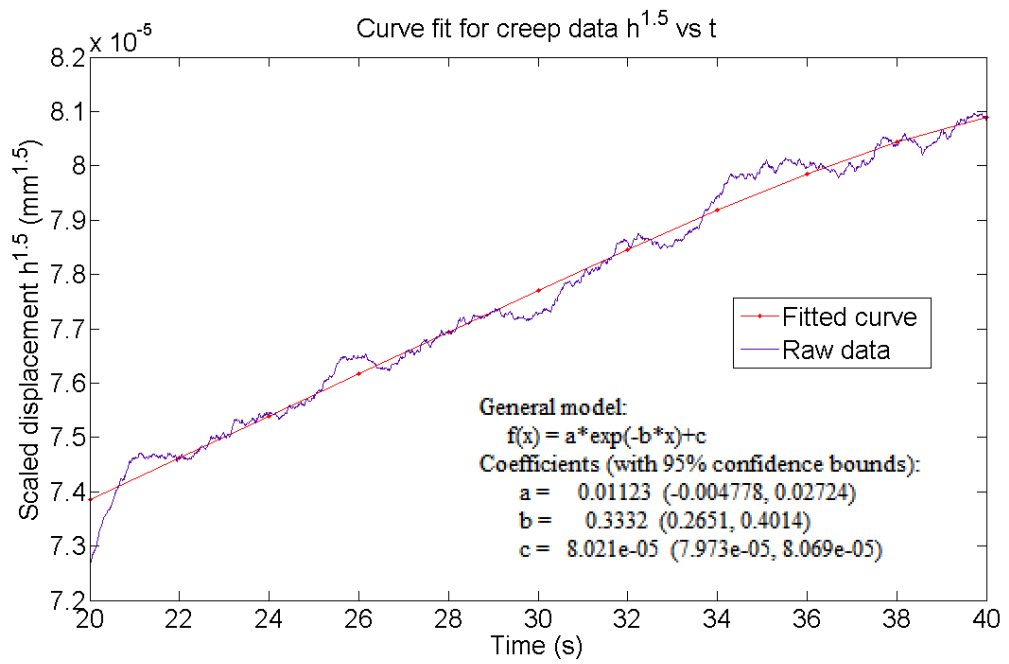


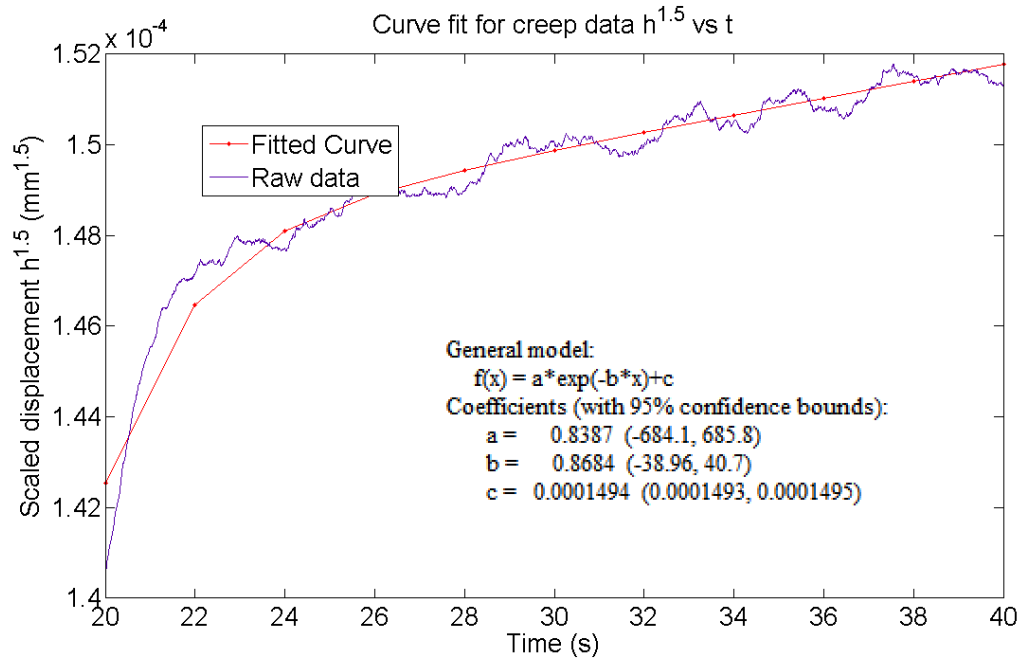
Figure 5.3 The displacement-depth curve of PTFE under creep indentation.



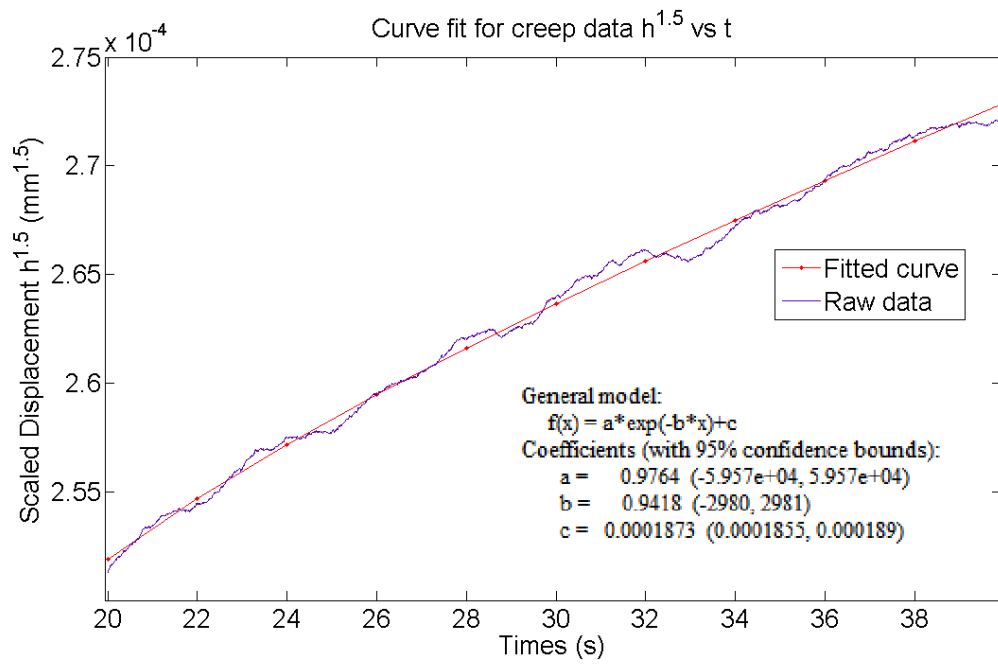
(a) 0.75mN



(b) 1.5mN

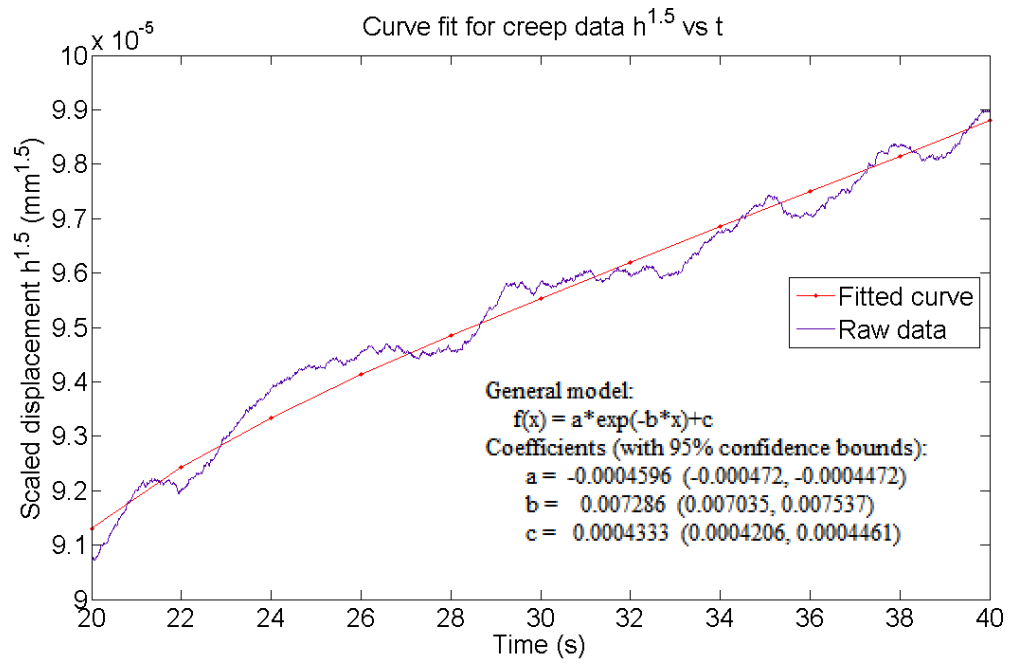


(c) 3mN

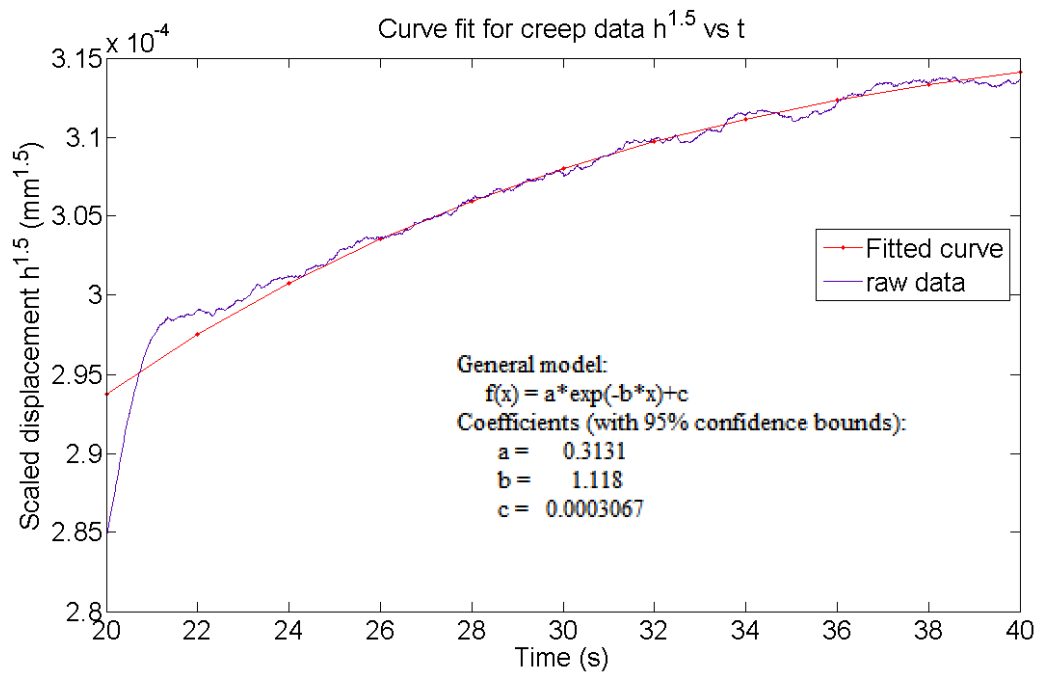


(d) 4.5mN

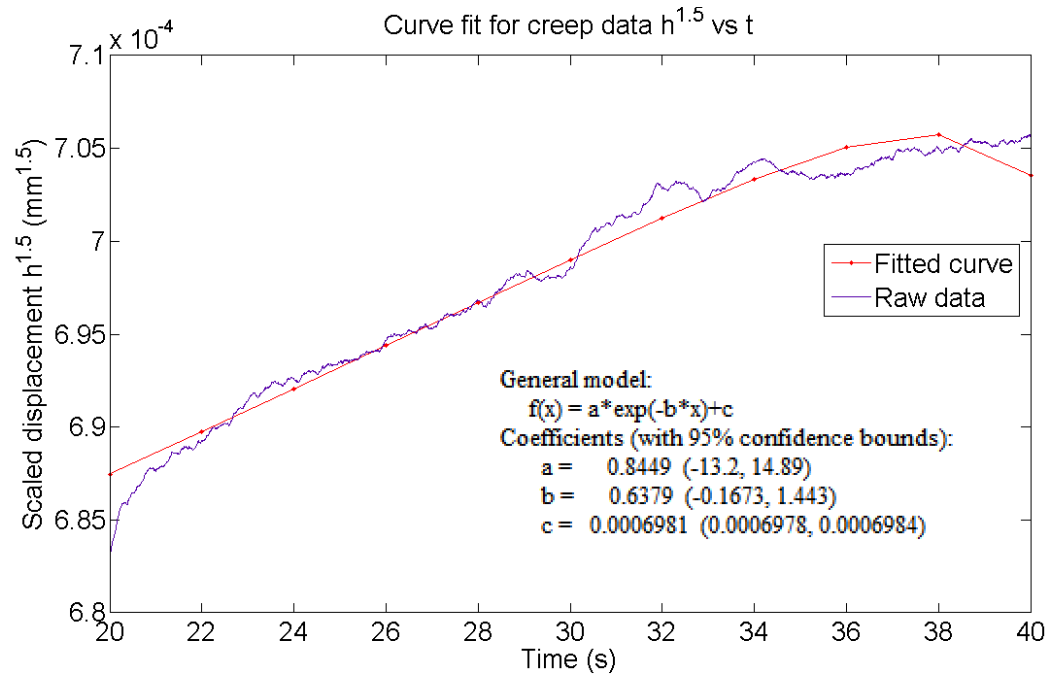
Figure 5.4 Creep experiment data curve fitting for PTFE under different peak load.



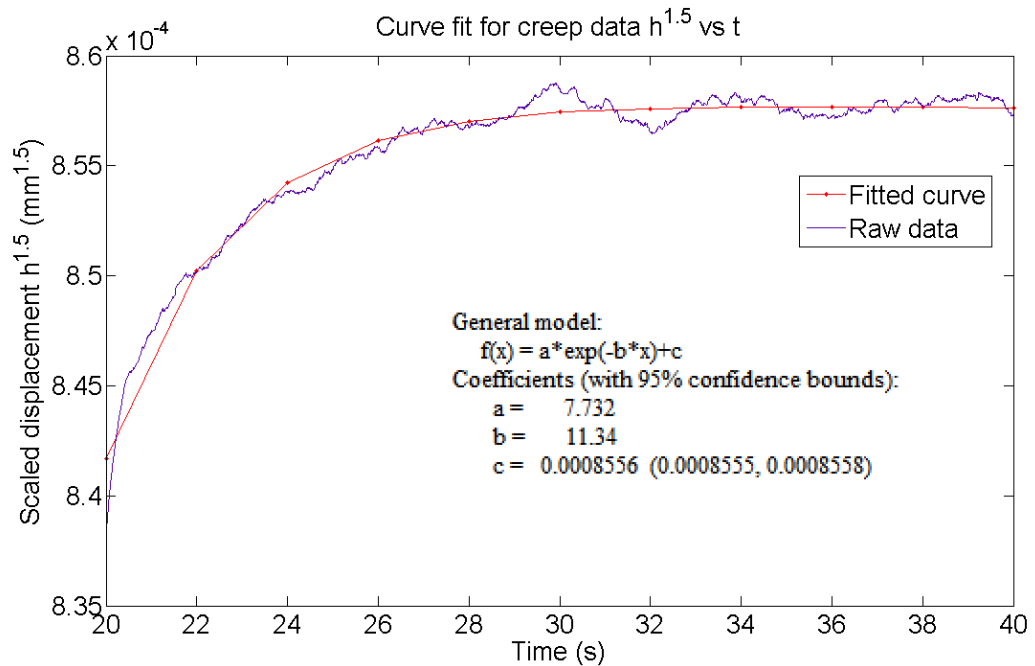
(a) 0.75mN



(b) 1.5mN



(c) 3mN



(d) 4.5mN

Figure 5.5 Creep experiment data curve fitting for styrene rubber under different peak load.

The displacement-time data during the 20 seconds holding period were fitted to

Equation (5-13) using two time constant ($i=1$). Therefore, the creep parameter (C_i, τ_i) can be derived from the curve fitting. The creep function parameters (C_i, τ_i) under different peak load were listed in Table 5-1 and 5-2.

Table 5-1 Viscoelastic parameter of PTFE

PTFE	$C_0 (\mu\text{m}^2/\text{mN})$	$C_1 (\mu\text{m}^2/\text{mN})$	$\tau_1 (\text{s})$
0.75mN	4.15	0.82	10.5
1.5mN	4.35	0.90	11.2
3mN	4.24	0.85	10.8
4.5mN	4.28	0.91	11.4

Table 5-2 Viscoelastic parameter of styrene rubber

Styrene Rubber	$C_0 (\mu\text{m}^2/\text{mN})$	$C_1 (\mu\text{m}^2/\text{mN})$	$\tau_1 (\text{s})$
0.75mN	278.2	78.4	16.2
1.5mN	288.3	80.2	17.4
3mN	285.4	81.8	16.8
4.5mN	284.5	79.3	17.0

The instantaneous modulus E_0 and long-term modulus E_∞ were calculated based on the creep parameter. These modulus values of PTFE and styrene rubber were demonstrated in Figure 5.6 and 5.7. It was found that the value of these modulus are largely independent on the peak load level. In addition, the ratio between E_∞ and E_0 represents the extent of time-dependent properties in the material. From the Figure 5.8, the ratio E_∞ and E_0 is between 0.7 and 0.65 for PTFE and 0.6-0.55 for styrene rubber, which indicates that styrene rubber exhibits more viscosity than PTFE.

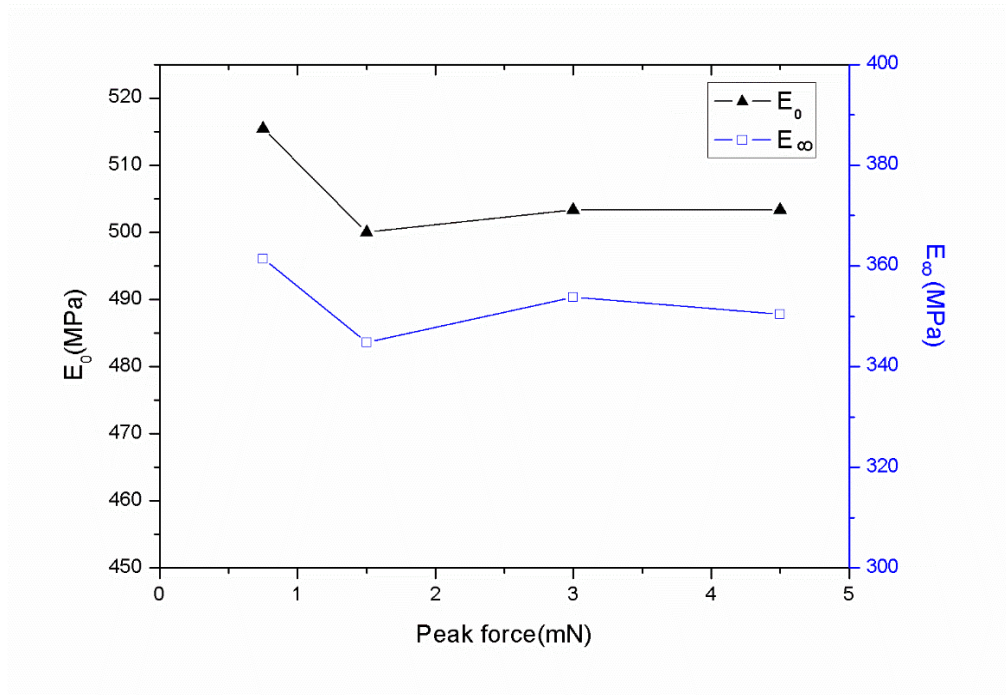


Figure 5.6 The value of E_0 and E_∞ of PTFE as a function of peak load level.

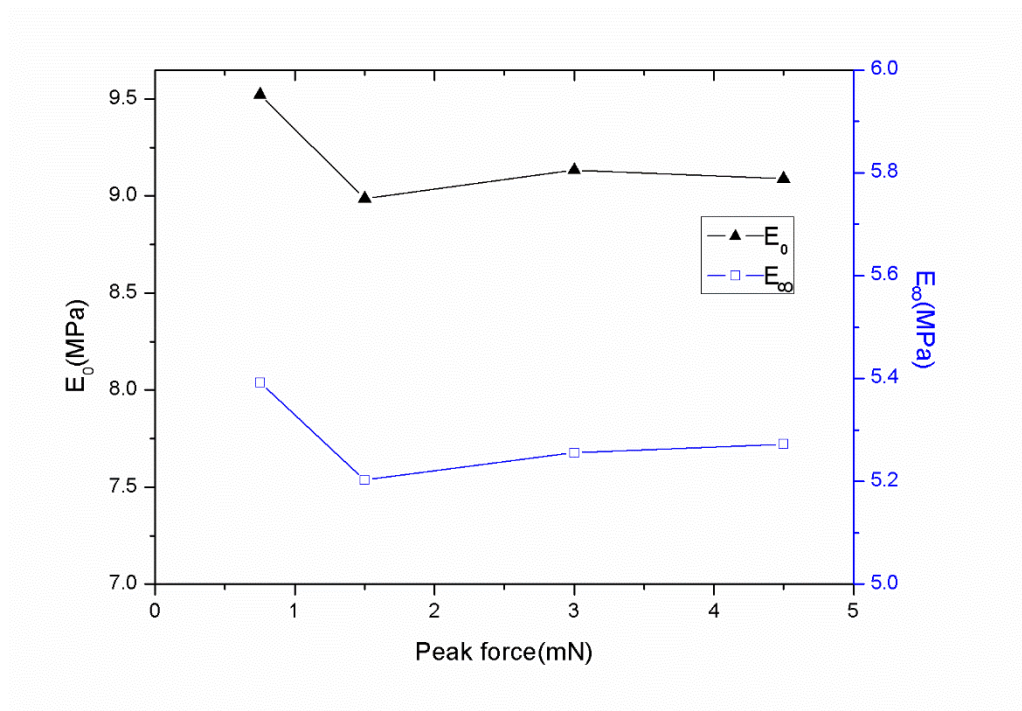


Figure 5.7 The value of E_0 and E_∞ of styrene rubber as a function of peak load level.

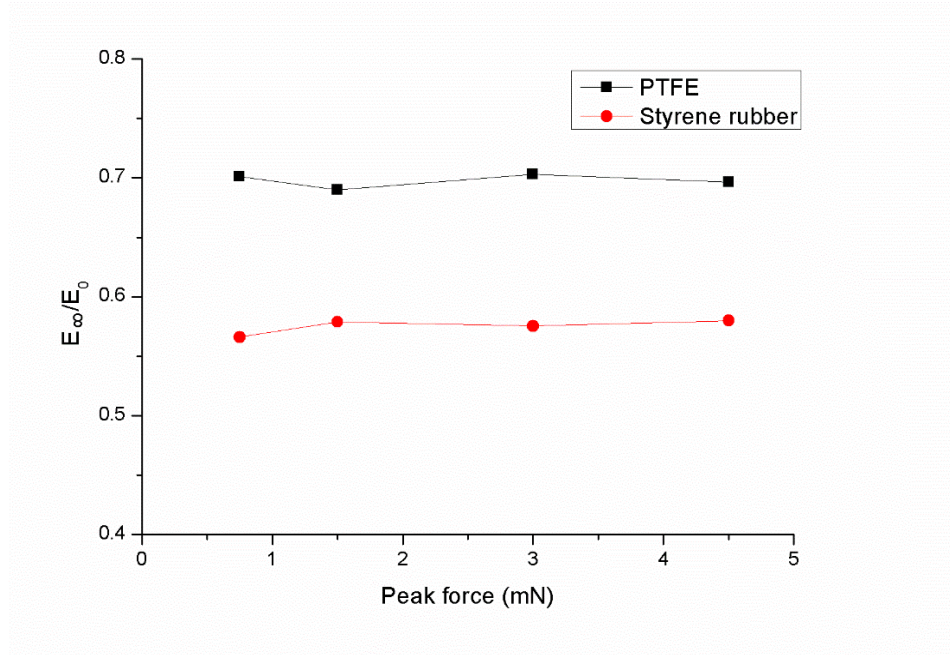


Figure 5.8 The ratio E_∞ and E_0 of two samples as a function of peak load level.

5.5 Discussions

In these two samples, the results of modulus values were not dependent on the experimental conditions. Besides, the results of elastic modulus in this study are in an acceptable agreement with previous study [82]. However, the merit of this investigation is that the testing approach implemented here can provide no single-value elastic modulus of viscoelastic material, but elastic modulus at two limited conditions E_0 and E_∞ .

Nanoindentation is a standard technique for analysis of elastic-plastic material, which already has been built into commercial facilities, while there is still no common criterion for testing viscoelastic properties in the material. Different methodologies of

exploring time-dependent properties are often aimed at two extreme circumstances and result in separately different results. For instance, creep loading profile of long term holding to exhaust the creep deformation will lead to the result approaching to (E_{∞}) value [92], whereas protocol of unloading rapidly will result in the value approaching to instantaneous elastic modulus (E_0) [93]. The benefit of the technique in this study is that in one measurement these values to both limited can be worked out. In addition, the difference between (E_{∞}) and (E_0) represents the extent of time-dependent properties in such materials. If the value of (E_{∞}) and (E_0) are comparable and close to each other, it is reasonable to use a single value to present the elastic modulus. Larger difference between (E_{∞}) and (E_0) indicates that using one term of elastic modulus is inappropriate for such material. According to the result of (E_{∞} / E_0), it demonstrated that styrene rubber exhibits more time-dependent property than PTFE. When it comes the time constant, it is important to note that for both of samples, the time-constant values are one shorter than the rising time 20s and another is longer than that. Similarly, the time-constant value of τ_1, τ_2 are independent of peak load level as well.

In this experiment, the depths of indentation ranged from tens of nanometers (for 0.75 mN on PTFE) to several micrometers (for 4.5 mN on styrene rubber). Although the stress levels varied much as well, all the indentation stress were small due to the large size of the tip generated dominantly viscoelastic deformation without plastic element involves in the experiment. The independent of the experiment results on the peak load level validated the use of a linear viscoelastic assumption for the sample is reliable. All the samples investigated in this study were bulk polymers, there was no

substrate influence due to the penetration depths were less than 1% thickness of the sheet. Therefore, further experiment would focus on applying the technique in this work to be implemented in the study of thin-film samples.

By using E_0 , E_∞ and τ , the storage and loss modulus can be worked out by Equation (5-37) and (5-38). The comparison result of these values of dynamic indentation and creep indentation were shown in Table 5-3 and 5-4.

Table 5-3 The comparison of the storage and loss modulus of PTFE

	(MPa)	Dynamic Indentation	Creep Indentation
1Hz	Storage modulus	169.6	486.5
	Loss modulus	35.7	48.6
3Hz	Storage modulus	154.0	499.4
	Loss modulus	35.4	16.7
5Hz	Storage modulus	119.9	499.8
	Loss modulus	33.9	9.99
7..5Hz	Storage modulus	96.2	499.9
	Loss modulus	33.3	6.66
10Hz	Storage modulus	74.1	500
	Loss modulus	38.2	4.99

Table 5-4 The comparison of the storage and loss modulus of styrene rubber

	(MPa)	Dynamic Indentation	Creep Indentation
1Hz	Storage modulus	1.53	7.52
	Loss modulus	0.38	0.52
3Hz	Storage modulus	1.27	8.82
	Loss modulus	0.35	0.17
5Hz	Storage modulus	0.95	8.83
	Loss modulus	0.30	0.11
7.5Hz	Storage modulus	0.41	8.83
	Loss modulus	0.28	0.07
10Hz	Storage modulus	0.35	8.83
	Loss modulus	0.30	0.05

It can be found that there is obvious different in the results obtained by dynamic nanoindentation and creep indentation, especially for the storage modulus under frequency of 10 Hz of both samples. More specifically, the storage modulus is close to 500 MPa obtained by creep method, while compared to the dynamic results ranged from 170 MPa to less than 100 MPa for the results of PTFE. Similarly for the styrene rubber, the results of storage modulus under different frequency is around 8MPa for creep method, however, the dynamic value is only ranged around 1 MPa.

At lower frequency, the results are relative close to each other. especially for the results of loss modulus. This indicates the frequency has an impact on the viscoelastic

properties. In addition, the differences between these results reveal that more complex element existed in the sample, such as plastic deformation during the indentation. Therefore, it is necessary to establish more accurate model includes elastic, viscosity as well as plastic. In addition, for the potential use of this technique in the future of biomaterial, the porosity has to be considered to get more realistic results of nano-indentation.

5.6 Summary

The current study focus on the direct measurement of time-dependent behaviors by ramp loading with a holding period indentation technique based on a viscoelastic hereditary integral model. Numerical values of time-dependent properties were obtained by fitting the creep data to the viscoelastic analytical solution. Compared to other techniques designated at eliminating the viscosity element by fast unloading, this method is capable of deriving both instantaneous and infinite modulus as well as viscosity time-constant. It was found that the experiment results are independent of the peak load level. Based on TPM facility, the creep indentation after ramp loading technique works well for characterizing time-dependent properties. This analytical method demonstrated that its promising ability of examination of biological tissue, which is a kind of extremely sensitive time-dependent material. To sum up, this study revealed the capability of TPM system characterizing viscoelastic properties in time domain. The comparison between creep method and dynamic method revealed that more work should be done in the future to bridge the gap between dynamic indentation

and creep method.

Chapter 6 Correlation analysis of surface tilt effect on its mechanical properties by nano-indentation

6.1 Introduction

In the last decade, we have witnessed that there was an increasing requirement in the capability of precise measuring surface which include not only surface geometry parameters, but also surface metallurgy such as stiffness, hardness, elastic modulus, adhesion etc. [94-96]. During the same period, more efforts have been exerted in the area which would enhance the surface properties to a desirable surface function [97]. For instance, a large variety of unique functionalized surface techniques were applied in industrial areas such as self-cleaning, anti-bacterial, anti-reflection and low friction surfaces [98-101]. It is generally believed that the surface topography is known to affect the surface properties of a bulk material in the macro scale. Furthermore, the surface texture plays an important role in its nature or designated functionalized surface. The influence of a surface geometry on its function is well understood at the macro level [102, 103]. Nevertheless, there are still some ambiguities existing in the relationship between the surface topography and mechanical properties in sub-macro level.

Nano-indentation is an effective approach for exploring the material's mechanical properties in micro/nanometre level. For example, being capable of measuring the

penetration depth in nanometre and the contact force in micro- or nano-Newton, nano-indentation is essential technique in the characterisation of thin film's mechanical properties [104]. However, there are many factors affecting the measured nano-indentation results [105]. The surface topography of a test specimen has a direct impact on the measured nano-hardness values. In addition, very few materials can have an atomically flat surface. Generally, the majority of used materials have an unflatten surface which is formed by undulations and irregularities. Therefore, the surface waviness would influence the nano-indentation results significantly. In some cases, the sample surface has to be polished prior to nano-indentation experiment. However, for some materials, which might be vulnerable to damages by polishing or the mechanical properties would exhibit alteration resulting from work hardening [106], this may lead to unreliable measurements.

Another influencing factor is sample tilt if assuming the surface is perfectly flat [107]. While in an actual experiment, it is difficult to perfectly orientate the sample surface perpendicular to the indentation tip. Moreover, some kinds of surfaces are designated to be made up of special topography for certain function, which cannot be further polished to give a flat/smooth surface. Therefore, it is worthwhile to explore the tilt effect of a surface being tested on the nano-indentation results and assess the errors associated with the surface topography.

In this chapter, the general sources of error in nanoindentation are review follow by geometry study of tilt effect of Berkovich tip. Then, we present our study on the tilt effect situation by applying both finite element analysis simulation and the actual

nano-indentation experiments on fused silica. The testing system is home-made facility TPM (tribological probe microscope), which was designed for localized surface property measurements, including topography, hardness, friction coefficient and elastic modulus. It has successfully measured variety types of material in previous studies [89,107]. To explore the relationship between the topography and mechanical properties, a standard sinusoidal surface has been used for nano-indentation by both finite element analysis and TPM measurements. Based on the finite element analysis simulation, the true contact area at each measurement point of the sinusoidal surface can be obtained and thus a correction can be applied to the raw data of the measured hardness values by TPM. Finally, the correlation between surface topography and its mechanical properties was carried out after eliminating the potential contact error in the measurements.

6.2 Error sources of nano-indentation

The nano-indentation facility is able to provide the results of mechanical properties, such as hardness, elastic modulus at micrometer or sub-micrometer scale. The errors in these results are mainly from three different sources, which include the measurement of force, depth and misalignment between the indenter and the sample surface. For example, the function of hardness when measured through nano-indentation method is:

$$H = \frac{F}{kD^2} \quad (6-1)$$

Where F is the value of peak force, D is the depth of indentation, k is a

constant factor of area function (Berkovich is 24.5). These three parameters are able to contribute to the total uncertainty in hardness. Consequently, it is necessary to examine the main source of the errors resulted from the force and depth uncertainties as well as the misalignment between the tip and the sample surface. This work would contribute to better understand the measurement of mechanical properties at nano scale.

The uncertainty in applied force influences the hardness result directly. Generally, the force resolution is between 1 μ N to 1nN in nano-indentation method. Nevertheless, according to the traceable force is about 5 μ N. The regulation is similar to the atomic force microscopy, where it specified that the force resolution is smaller than the actual minimum traceable force. This is because in practice there will be surface force (Van de Waals, adhesion, etc.) that would lead to a gap between the force applied to the contact zone and the value measured from the force sensor. In addition, the tilt angle between the applied force and surface normal vector is another contribution of error in force. The misalignment will result in an error of cosine the angle.

The depth error is measured and limited by the displacement sensor in the facility. The uncertainty in depth is determined by a traceable displacement interferometer or capacitive sensor with sub-nanometer resolution. Similarly to force uncertainty, the misalignment between the drive and measurement axis would lead to uncertainty in displacement result.

The errors in force and displacement are considered scrutiny in this research area. However, other factors may exhibit more impact on the result of nanoindentation. The area function of the indenter is one of such uncertainties which own a direct influence

on the nanohardness. This uncertainty is generated from the manufacturing of the ideal geometry for the tips. For instance, the typical errors in Berkovich tip are face and base angle errors as well as tip rounding. For the measurement of the tip shape, the scanning white light microscopy is not feasible due to the steep angle and spatial resolution. While, this error can be investigated by atomic force microscopy to map the profile of the tip shape.

Another important source of error is due to the misalignment between the axis of the tip and the normal vector of the sample surface, which is not dependent on the manufacturing of the tip. It is defined in ISO 14577 [108] that the error in angle on the axis should not be more than 1.0 degrees. It is not mentioned the detail information about the values for different types of indenters (Vicker, spherical or Berkovich). In addition, there is no clearly definition of whether this value is from the central axis in a spherical coordinate system or if the indenter and the tilt angle should be within a degree (larger than 1 degree in spherical coordinates).

Generally, for the tips of indentation, a diamond is adhered onto a stiff shank and polished to an appropriate dimension in order to eliminate the error resulted from manufacturing. The geometry of the tips will be altered due to diamond tip would be wear with the usage of the indenter increased. It is difficult to avoid this type of variation in actual measurement. Moreover, extra error can be produced by the thermal variation in the indenter of sample. The calibration of these misalignments for every measurement is time consuming and not practicable. Therefore, it is important to examine the uncertainties in these parameters, which are directly related to the results

of nanoindentation. The work in this chapter mainly focuses on the misalignment between the tip and sample impact on the results of hardness and elastic modulus.

During the process of nano-indentation, the applied force and the depth of penetration are recorded at the same time. The Oliver-Pharr method [31] is widely used in the instrumented indentation test to work out the hardness and elastic modulus. More specifically, the hardness is defined as the ratio between the maximum indented force and the projected contact area.

$$H = \frac{P_{\max}}{A_c} \quad (6-2)$$

The elastic modulus can also be derived based on the elastic contact theory of Sneddon's analysis [38], which is shown in Equation (6-3):

$$E_r = \frac{\sqrt{\pi}}{2\beta} \frac{S}{\sqrt{A_c}} \quad (6-3)$$

Where E_r is the reduced modulus, β is a correction factor which is accounted for the tip geometry. S is contact stiffness, which is equal to the slope of unloading force-depth curve. In the actual experiment, a Berkovich tip was selected, the value of β is 1.072 in this study. The deformations of the indenter and the sample are considered in the reduced modulus. Therefore, the reduced modulus can be defined as:

$$\frac{1}{E_r} = \frac{1-\nu_s^2}{E_s} + \frac{1-\nu_i^2}{E_i} \quad (6-4)$$

Where E_s and ν_s represent the elastic modulus and Poisson rate of testing sample, respectively. E_i and ν_i represent the elastic modulus and Poisson rate of the Berkovich tip. The project area is the major factor in the determination of the

mechanical properties on the basis of nano-indentation method. The projected area is calculated based on an analytic function of the contact depth, $A = f(h_c)$. For a Berkovich tip, $A = 24.5h_c^2$. The contact depth is derived by Sneddon equation below:

$$h_c = h_{\max} - \varepsilon \frac{P_{\max}}{S} \quad (6-5)$$

Where h_{\max} is the depth at the peak load (P_{\max}). ε is another correction factor which depends on the indenter geometry as well. The value of ε is set to be 0.75 according to the Oliver-Pharr method [31].

6.3 Geometry study of related Berkovich tip

Before the simulation and actual experiment, it is necessary to investigate the tilt effect on the projected area of Berkovich tip under geometry study. In this method, the tip is model under Cartesian coordinate system. The ideal Berkovich tip is a three-sided pyramid with triangle base at angle β for 65.27° . It is assumed that all three faces meet at a single point, which is the original point of coordinate system. The geometry model is shown in Figure 6.1.

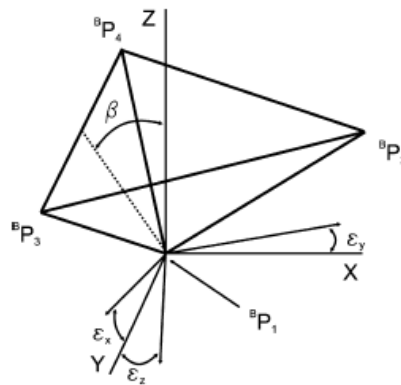


Figure 6.1 Geometry model of Berkovich tip

Under this model, with a given depth d , the project area of Berkovich tip can be derived as follows. For a perfectly mounted Berkovich tip, the vectors of three edges are:

$${}^B\mathbf{P}_2 = \{2d \tan \beta, 0, d\}^T \quad (6-6)$$

$${}^B\mathbf{P}_3 = \{-d \tan \beta, d\sqrt{3} \tan \beta, d\}^T \quad (6-7)$$

$${}^B\mathbf{P}_4 = \{-d \tan \beta, -d\sqrt{3} \tan \beta, d\}^T \quad (6-8)$$

When the tip is not perfectly mounted, the rotated unit vectors, scale factor and rotated edge vectors are

$${}^B\mathbf{e}_n = \mathbf{R} \frac{{}^B\mathbf{P}_n}{|{}^B\mathbf{P}_n|} \quad n = 2, 3, 4 \quad (6-9)$$

$$C_n = \frac{d}{{}^B e_n k} \quad n = 2, 3, 4 \quad (6-10)$$

$${}^B\mathbf{P}_{Rn} = {}^B C_n {}^B\mathbf{e}_n \quad n = 2, 3, 4 \quad (6-11)$$

Consequently, the contact area is

$${}^B A_s = \frac{1}{2} |{}^B\mathbf{P}_{R2} \times {}^B\mathbf{P}_{R3}| + \frac{1}{2} |{}^B\mathbf{P}_{R4} \times {}^B\mathbf{P}_{R3}| + \frac{1}{2} |{}^B\mathbf{P}_{R2} \times {}^B\mathbf{P}_{R4}| \quad (6-12)$$

The projected area is obtained by the Equation (6-9) to (6-11)

$${}^P B_1 = {}^B P_{R3} - {}^B P_{R2} \quad (6-13)$$

$${}^P B_2 = {}^B P_{R4} - {}^B P_{R2} \quad (6-14)$$

$${}^B A_p = \frac{1}{2} |{}^B B_1 \times {}^B B_2| \quad (6-15)$$

Simulation works were performed with the ε_x and ε_y ranged between 1 to 5 degrees with the twist is constant at 0 degrees. Figure 6.2 to 6.6 illustrate the errors in projected area under different tilt angle. It is obvious that with the increasing angle, the

errors in projected area go up.

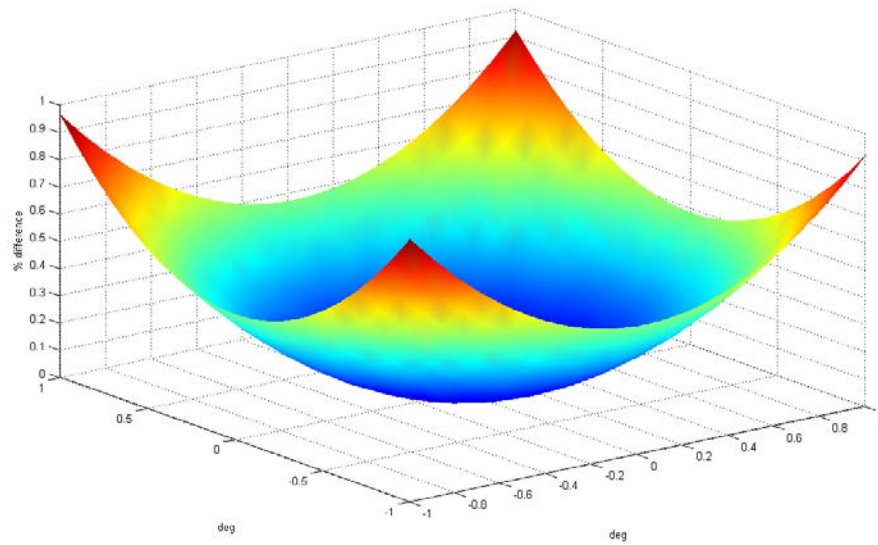


Figure 6.2 Percentage errors of projected area for Berkovich tip as the function of tilt angle range between -1 to 1 degree.

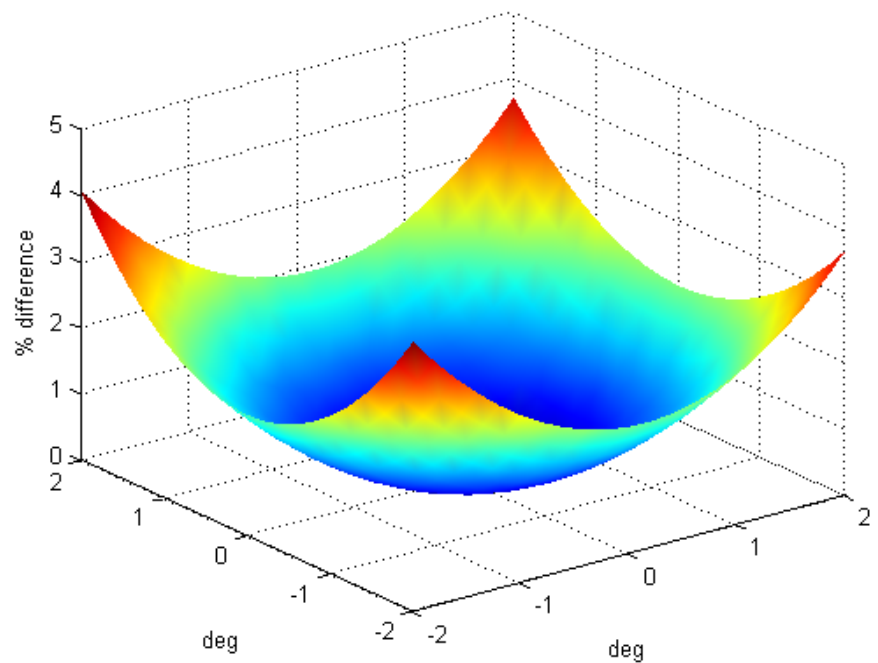


Figure 6.3 Percentage errors of projected area for Berkovich tip as the function of tilt angle range between -2 to 2 degree.

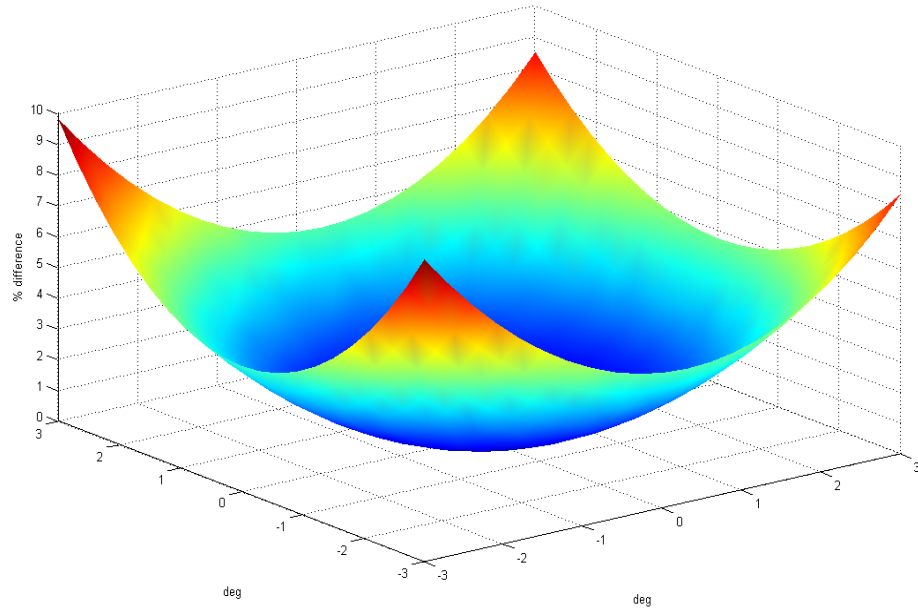


Figure 6.4 Percentage errors of projected area for Berkovich tip as the function of tilt angle range between -3 to 3 degree.

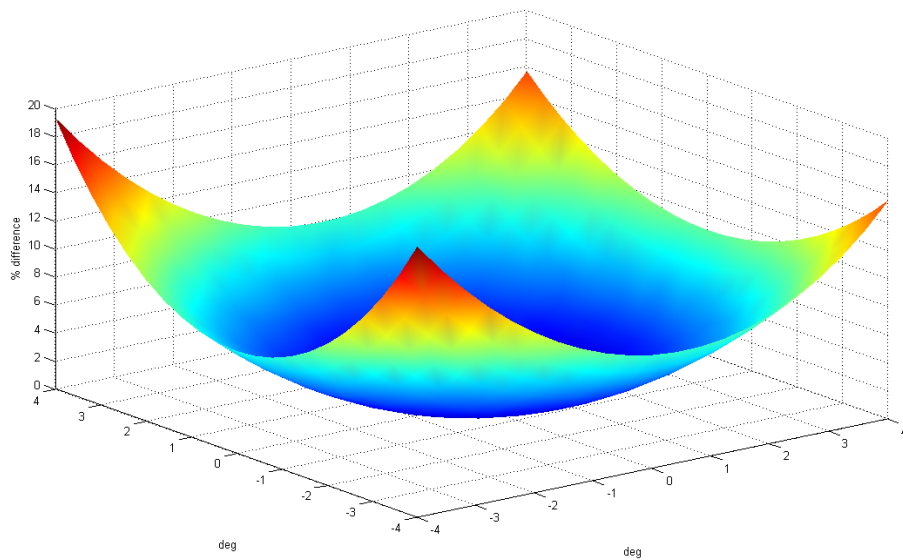


Figure 6.5 Percentage errors of projected area for Berkovich tip as the function of tilt angle range between -4 to 4 degree.

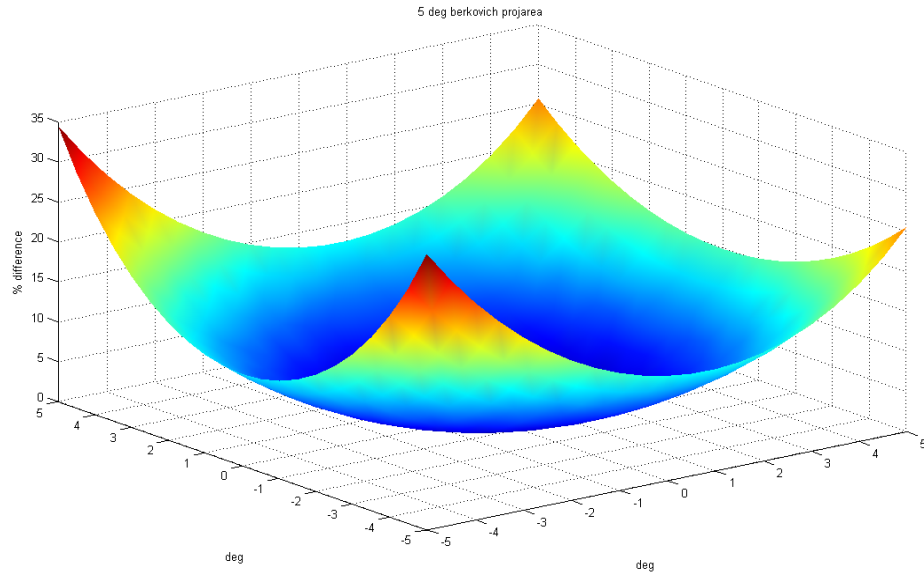


Figure 6.6 Percentage errors of projected area for Berkovich tip as the function of tilt angle range between -5 to 5 degree.

According to Figure 6.2, the errors under 1 degree tilt is less than 1%, which demonstrates that the error in Berkovich tip is allowed by ISO 14577. Under the circumstance of larger tilt angle from 2 to 5 degrees, the errors are much more significant increasing from 4% to about 30%. In addition, there exhibit obviously non-symmetry in error at higher tilt angle.

6.4 Nano-indentation on tilt sample

6.4.1 Finite element simulation

The commercial finite element software ABAQUS 6.11 was used to simulate the tilt situation of nano-indentation. In this study, a two-dimensional model of a rigid

Berkovich tip impressing on a fused silica sample was established in Figure 6.7. The Berkovich tip was defined as an analytical rigid surface which is perfectly sharp in a pyramid style. The indented sample was modelled as a rectangle with the dimension of $2 \times 2 \mu\text{m}^2$. The tilted angle of the sample with respect to the vertical axis of the tip is between 0° and 5° . The sample was modelled as CPE4R element which is suitable for indentation analysis. For this study, there is no friction considered between the rigid tip and the surface of the sample. To be consistent with the actual experiment, the simulation process was under force control which applying 5 mN force on the tip. The material of the testing sample, fused silica, was modelled as an elastic-plastic material with elastic modulus 72 GPa, Poisson ratio 0.17 and yield strength 7.2 GPa.

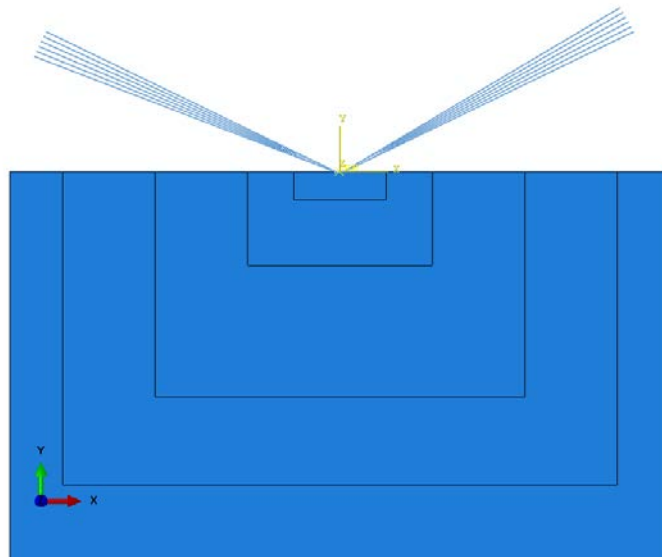


Figure 6.7 Model of tilt indentation on a flat sample in FEA.

In order to get a high efficiency calculation, a progressively coarse mesh was set in the area far from the contact zone. For the sake of obtaining an accurate result, finer

mesh was employed in the contact region in Figure 6.8. The element size in the contact area is between 10 nm and 20 nm. The relationship between the applied force and penetration depth is demonstrated by P-h curve, which was obtained from the reaction force of the tip against the vertical displacement of the contact point of the sample.

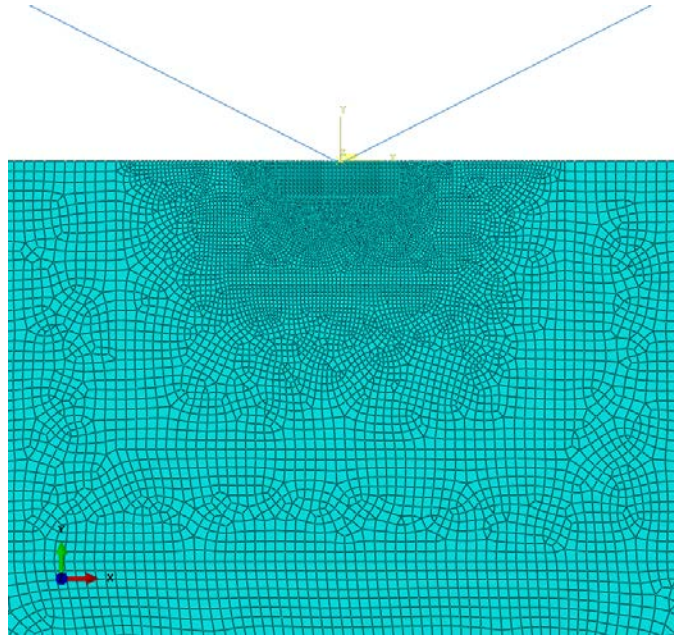


Figure 6.8 Mesh of the indentation sample.

6.4.2 Nano-indentation experiment on fused silica sample

The actual experiment was performed on a fused silica specimen, which was obtained in the form of a round disk with 2 mm thickness. It is generally acknowledged that fused silica is a widely used material in nano-indentation test due to its homogenous and isotropic behaviour in physical properties. There is no further treatment of the sample before the experiment. It is only the roughness of the fused silica that was measured by using a commercial facility WYKO white light interferometry. The average roughness of the sample is $0.105\mu\text{m}$. The facility used for

nano-indentation experiment is unique home-made equipment, Tribological Probe Microscopy (TPM), which has successfully been used to measure the mechanical properties of variety materials in previous studies [89,107]. An exclusive sample holder that can tilt the sample horizontally to maximum 2.5° was made for this test. All the experiments were performed under force control with a diamond Berkovich tip to indent the sample. The testing system, TPM, has been calibrated prior to the tilt indentation. With a careful operation, five indents were conducted at a tilt angle from 0° to 2.5° under a constant peak force of 5 mN.

6.5 Nano-indentation on the sample with sinusoidal surface

6.5.1 Finite element simulation

In this part, a 2D finite element model of nano-indentation on a sinusoidal surface sample was established based on the software ABAQUS 6.11. The indentation tip was also the same as shown in the previous simulation that a sharp Berkovich tip was selected. The surface of the tip was set as an analytical rigid surface. The material of the sample is set as elastic-plastic model with elastic modulus 50 GPa, Poisson ratio 0.31 and yield strength 1 GPa. The local variation of the sinusoidal surface will be used to investigate the tilt effect, thus the nano-indentation was performed at different positions (from P1 to P7) of this sample, as illustrated in Figure 6.9.

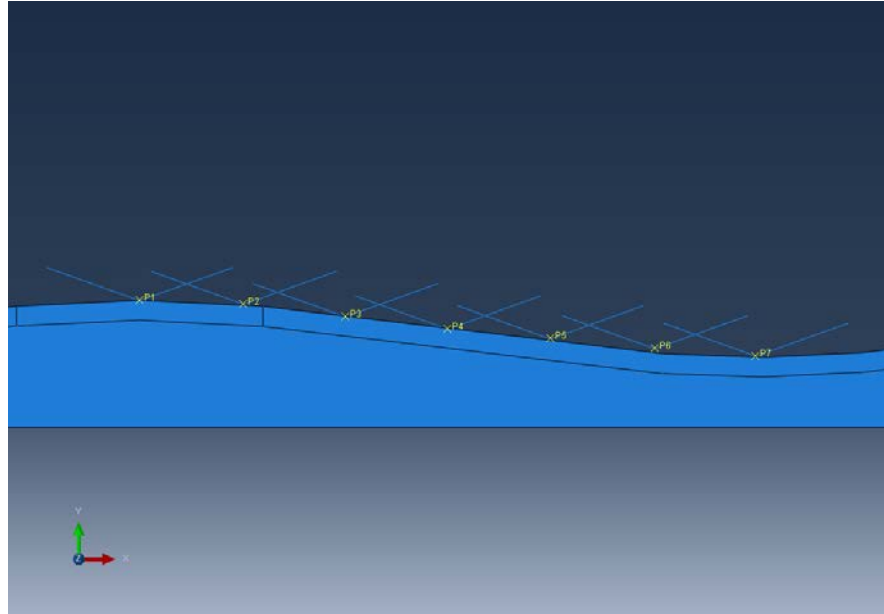


Figure 6.9 FEM simulation of indentation on a sinusoidal surface sample.

Therefore, there is no tilt angle at P1 and P7, as they are either the top or the bottom of the sinusoidal curve, while the tilt degree of P4 is maximal. In addition, to simplify the situation, the friction between the tip and the surface is not considered. The indentation simulation was performed under a peak force of 0.8 mN at each position point. The P-h curve was directly obtained from the applied force and the output of the deformation depth.

6.5.2 Experiment on standard sinusoidal specimen

The specimen used in this actual experiment is made from pure electroformed nickel with a hard top film of nickel-boron (Ruber & Co Ltd). The sinusoidal surface sample was measured under a commercial white light interferometry to obtain the surface topography. After that, the main experiment was performed under the same facility as in section 6.4.2, but without the tilt holder. The multi-function

measurements which include topography and hardness and elastic modulus were carried out by TPM with an initial scanning force of 0.1 mN and a peak force of 5 mN over an area of $100 \times 100 \mu\text{m}^2$. Due to the unique function of TPM, which can measure both the topography and mechanical properties at the same time, it allows us to investigate the correlation between the mechanical properties and topography of the sinusoidal sample.

6.6 Result and discussions

Figure 6.10 demonstrates the P-h curves which were obtained from FEA of the Berkovich indentations between 0° and 5° . It was clearly shown that under the same peak force of 0.8 mN, the penetrated depth decreases with the increase of the tilt angle. In other words, under the same applied force, no tilt indentation produced deeper penetration than tilt indentation.

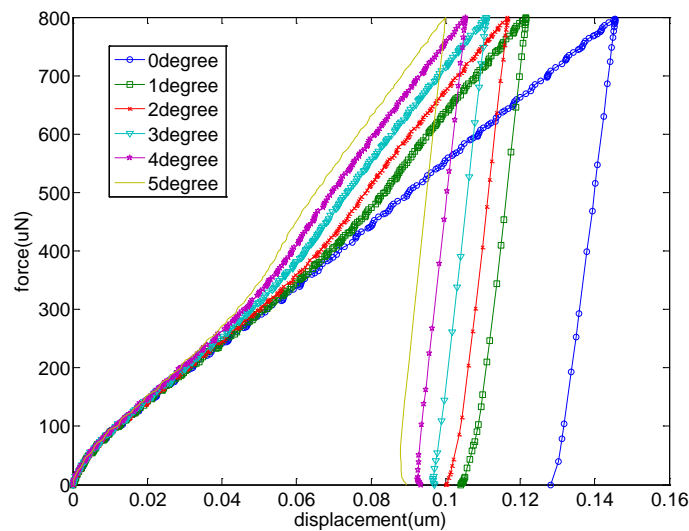


Figure 6.10 FEA simulation result of P-h curves under different tilted degree.

It was obviously in Figure 6.11 that the experimental results from tilt indentation on fused silica had a similar trend compared to the FEA simulation output. The P-h curves obtained from actual experiments showed that the penetration depth decreased with the increase of the tilt angle under the same applied force of 5mN.

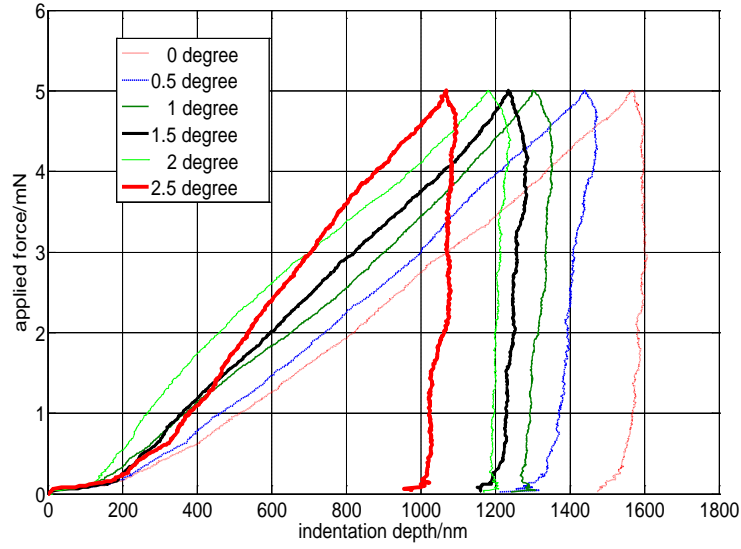


Figure 6.11 P-h curves of nano-indentation experiment on the fused silica sample.

When the series of P-h curves were obtained, the contact area of each indentation can be derived by using the O-P method which is based on the loading-unloading curves. Therefore, the mechanical properties of the testing sample, hardness and elastic modulus can be calculated from Equation (6-2) to Equation (6-5). For each tilting angle, the contact area has also been computed from the finite element simulation. The projected contact area can now be calculated by using the Equation (6-16), which is projected in the plane perpendicular to the vertical axis.

$$A_{cprojected} = A_c^{FEA} \cdot \sin \theta \quad (6-16)$$

Where A_c^{FEA} is the result of contact area in FEA modelling, $\theta = 65.3^\circ$ for a

Berkovich indenter. The relationship between the contact area and tilted angle is shown in Figure 6.12. Although both trends of two curves are similar that the contact area decreased as a function of increased tilt angle from 0° to 5° , it was clearly that O-P method underestimated the contact area compared to the FEA simulation results. For instance, in 5° tilt condition, the contact area was only 2% decreased while O-P method presented it to 10% reduction.

Due to the difference in the contact area as shown in Figure 6.12, the hardness (H) and elastic modulus (E) are thus much varied against the tilt angles. It can be seen from Figure 6.13 that the standard O-P method gives underestimated contact areas which result in overestimating the hardness (H) and elastic modulus (E) values. Based on the actual contact area obtained from FEA output, H and E remain less dependent on the tilt angle. The difference between these two approaches goes up as the tilt angle increases. In the case of maximum tilt of 5° , the standard O-P method overestimated the hardness and elastic modulus for 11% and 4%, respectively.

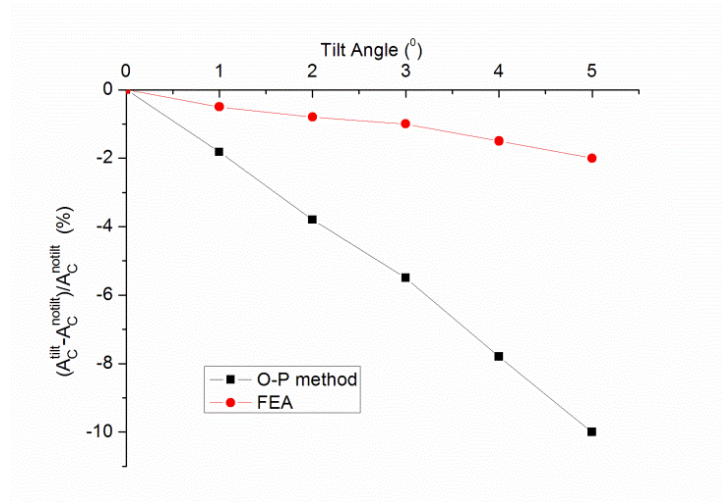


Figure 6.12 The variation of the contact area due to tilting by both O-P method and FEA simulation.

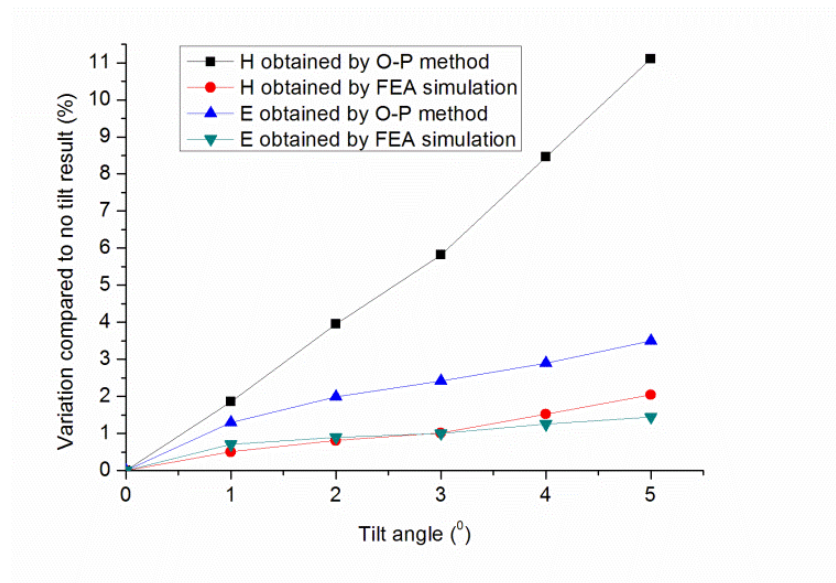
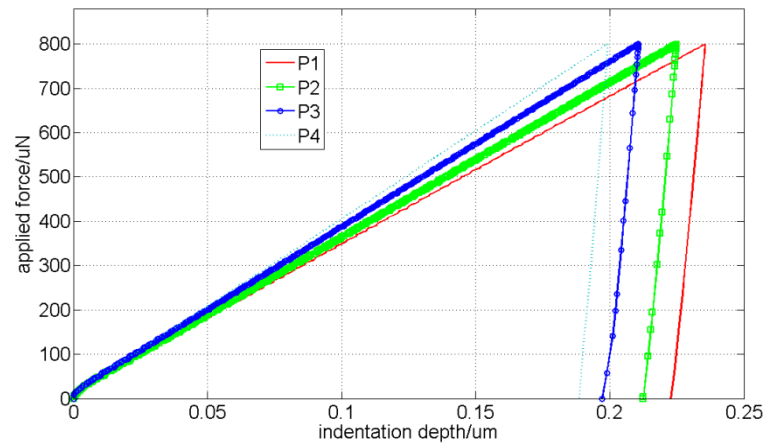


Figure 6.13 Comparison of E and H values from FEA and O-P method at different tilt angles.

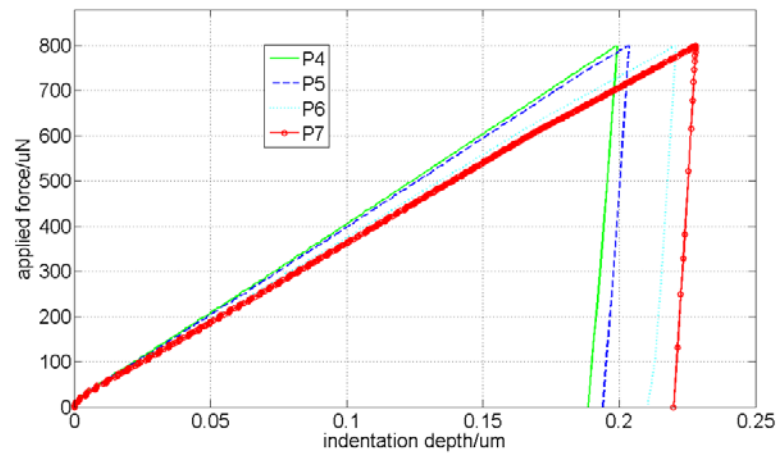
Similar results have also been found in the actual nano-indentation experiments on a fused silica. Based on the standard O-P method, the measured results show a clearly

overestimation of hardness values by 10% and elastic modulus by 5%. By applying the corresponding correction factors which are derived from the FEA method as discussed above, the over values were down to 2% for hardness and 1% for elastic modulus. Therefore, we have demonstrated that by applying the FEA correction for the contact area obtained from the measurements, the errors due to tilt indentation can be minimised.

For the indentation of a sinusoidal surface, which naturally exhibits undulation even if under perfectly perpendicular alignment, the results should have a similar tendency compared to the tilt indentation on flat sample. Firstly, we run the FEA simulation on a sinusoidal surface and the calculated P-h curves of nano-indentation are shown in Figure 6.14. Under the same applied force, the penetration depth varied at different positions of the sample. This variation in P-h curves would indeed result in the variation of nano-indentation results. Figure 6.15 shows the calculated E and H values based on the standard O-P method and FEA correction. At the maximal slope of position P4, both the hardness and Young's modulus values are the largest. By applying the FEA corrections the variation in H and E is much reduced. There is no doubt that the O-P method overestimated the mechanical properties, especially more obviously from Position P2 to P6. Such potential errors from angle indentation could be minimised by the FEA corrections, if the tilt angle is known.



(a)



(b)

Figure 6.14 P-h curves obtained at different position of the sinusoidal surface from FEA as illustrated in Figure 6.9: (a) Positions 1 to 4; (b) Positions 4 to 7.

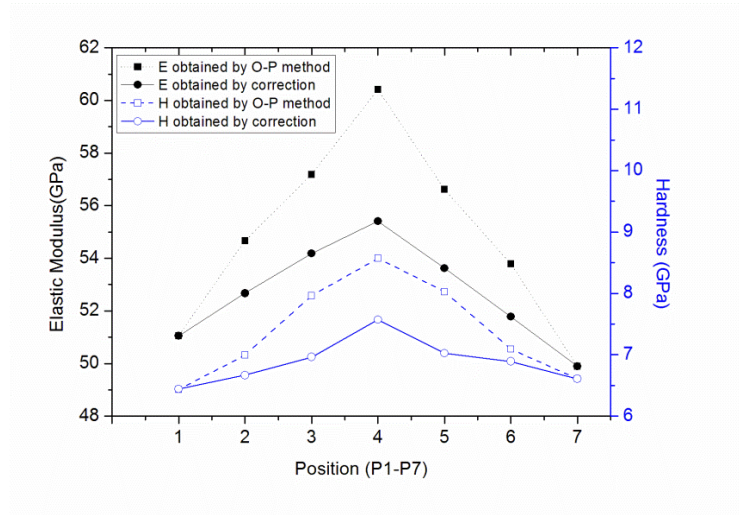
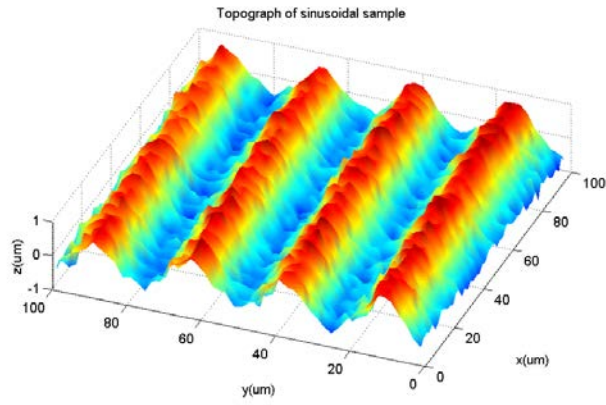


Figure 6.15 Comparison of E and H obtained by the O-P method and FEA correction for indentation at different positions of a sinusoidal surface.

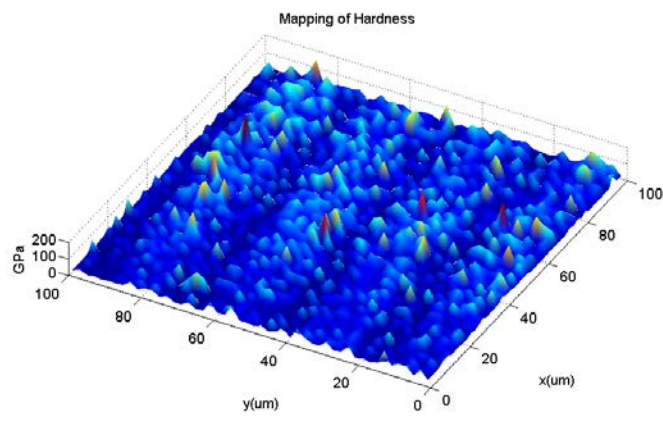
Consequently, it is necessary to modify the results measured by TPM on the nickel specimen with a sinusoidal surface. The sinusoidal surface parameters of the nickel sample are listed in Table 6-1 from the surface measurements carried out by white light interferometry and TPM. In addition, the mapping images of topography, hardness and elastic modulus of the sinusoidal sample are shown in Fig. 6.16.

Table 6-1 Surface parameters of sinusoidal sample measured by WYKO and TPM

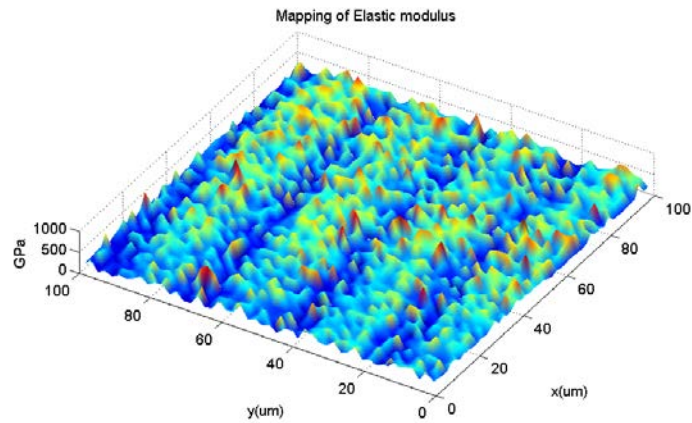
	WYKO NT2000	TPM
R_a (μm)	0.351	0.325
R_q (μm)	0.388	0.370
R_t (μm)	1.50	1.20
S_m (μm)	25.0	25.1
E (GPa)		225.3
H (GPa)		27.3



(a)



(b)



(c)

Figure 6.16 Mapping results of mechanical properties by TPM: (a) topography; (b) hardness; (c) elastic modulus.

The three images were obtained by TPM in one set-up and originally the efforts have been made to see how surface topography affects the mechanical properties. Obviously the local slope of the sinusoidal surface acts like tilting effect on indentation. As the measurements were made point-by-point at more or less the same time, the images thus obtained can be used to show the correlation between the topography and mechanical properties [89]. According to the FEA simulation result of sinusoidal surface, the original results of mechanical properties would be overestimated in some regions of this periodical surface. Consequently, the correction of original result is needed to remove the potential errors resulting from the measurement of undulate surface. Figure 6.17 shows the averaged surface profile, average hardness profile and the corrected hardness profile over an area of $100 \times 100 \mu\text{m}^2$.

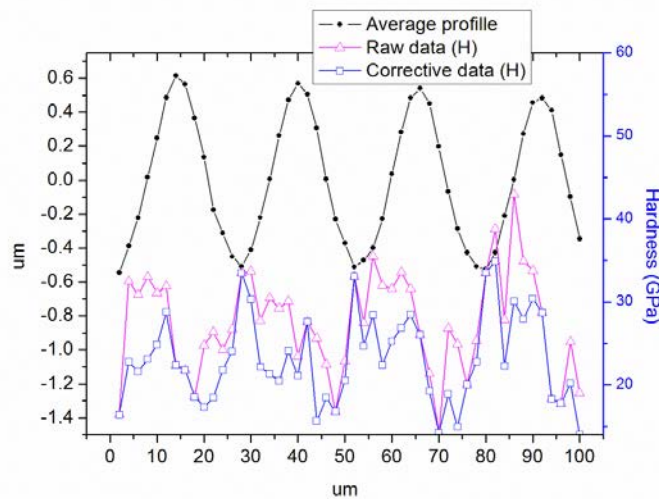


Figure 6.17 Averaged topography, hardness before and after correction for the sinusoidal sample.

It is demonstrated that the effect of topography on its mechanical properties is less than expected. The cross correlation between topography and mechanical properties were calculated. On the basis of the raw data, the correlation value between topography and hardness is -0.38, while after correction, this result was down to -0.25. The negative result of correlation factor was also found on other types of material according to previous work [89]. The original averaged hardness is 27.3 GPa with a standard deviation of 6.3 GPa for the sample. After correction, the mean value was down to 23.1 GPa, moreover, the standard deviation decreased to 4.1 GPa. Similar results were found in the elastic modulus as well. These findings indicate that although there is a negative relationship between the surface topography and hardness, the level of their relations was not as high as expected before. The corrected results reveal that the waviness surface still has an impact on its mechanical properties; the error resulting from the tilting indentation can be reduced by means of FEA corrections.

6.7 Summary

This study has explored the influence of surface tilt on nano-indentation result. FEA simulation and nano-indentation experiments have been conducted to demonstrate that the standard O-P method underestimated the contact area which leads to overestimation of the elastic modulus and hardness of testing samples. The result shows that the errors leading by 5° tilt are 4% in elastic modulus and 11% in hardness. Similar regulation has been found in the study of the standard sinusoidal specimen. Corrections on the preliminary result based on FEA simulation were carried out to

compensate the errors due to tilt impact of the nano-indentation result. By doing so, the correlation factor between the sinusoidal surface and its hardness was altered from -0.38 to -0.25. Moreover, the average and standard deviation of hardness also decreased from 27.3 ± 6.3 GPa to 23.1 ± 4.1 GPa. This conclusion reveals that the degree of surface waviness impact on its mechanical properties is not as great as expected before.

Chapter 7 Conclusions and recommendations for further work

7.1 Conclusions

In summary, this research mainly involves the establishment a cost effective home-made facility to investigate the viscoelastic properties of materials. The key research findings and contributions are presented as follows:

Based on the quasi-static nanoindentation on the viscoelastic material, it is found that there is obvious ‘nose-like’ phenomenon on the P-h curves obtained in the experiment. This will result in large errors in the results of mechanical properties. In addition, the load size effect is significant in the results of viscoelastic samples. The uncertainty is higher at the shallow depth because of the limitation to accurately determine the contact area in smaller depth. Above all, it is proved that quasi-static nanoindentation based on the Oliver Phar method is not suitable for characterizing the viscoelastic material.

Dynamic nanoindentation is an effective approach to characterize the viscoelastic properties rather than quasi-static method. The experiments were performed by using a spherical tip, the viscoelastic properties including storage, loss modulus and loss factor were derived. The results revealed that these three parameters do not independent of the loading frequency. The variation of the loading frequency would result in significant changes in the measured result. Compared to the results obtained from

quasi-static indentation dynamic approach is able to offer more richful viscous information.

Another effective method to explore the time-dependent property is by ramp loading with a holding period (creep) nanoindentation technique. It is calculated by curve fitting the creep data to viscoelastic analytically model to derive numerical values of the viscoelastic analytical model to derive numerical values of viscoelastic properties, including instantaneous and infinite modulus as well as viscosity time-constant. It is found that these three parameters are independent of the value of the peak force. The creep indentation method works well for the study of viscoelastic properties. In addition, instant and infinite modulus can be transferred to the storage and loss modulus under any frequency. The comparison between dynamic and creep method reveals that more effort should be paid in this area to bridge the gap between them.

The study of the tilt effect on the standard nanoindentation result demonstrates that the Oliver-Pharr method would underestimate the contact area, which would lead to underestimate the elastic modulus and hardness. Similar regulations were found in the study of the standard sinusoidal sample. Therefore, it is necessary to correct the errors in the results to eliminate the tilt influence. It is demonstrated that the surface waviness is able to influence the mechanical properties of the material.

To sum up, this study proved the ability of our home made facility to further investigate the viscoelastic materials. The ISO 14577 is the standard for the instrumented indentation test for hardness and materials parameters of metallic materials. However, there is still no standard for any compliant material due to their

complex mechanical properties compared to metallic materials. Consequently, the contribution of this work is a leading edge study for the establishment a standard in this area in the future. More importantly, it will pave a new way for the investigation the relationship between the surface topography and viscous property of soft matter including various biomaterials in the near future.

7.2 Recommendations for future work

According to the results of current works, several recommendations for future works in this area are discussed here.

First of all, it is necessary to establish a more complex model for analysis the soft matter to bridge the gap between dynamic nanoindentation and creep nanoindentation due to plastic deformation may exist during the experiment process. In the second point, the application of nanoindentation technique used for investigating biological material is more and more popular recently. Some of the biomaterials own the similar mechanistic properties as an engineering material. For example, the mineralized biomaterials including teeth and bones are suitable for the traditional nanoindentation method. However, when it comes to more compliant biomaterials, their mechanical properties are more complex than engineering materials.

The range of soft biomaterials is wide, including tissue, organ or even cell. For instance, soft tissue is very compliant sample with hydrated and complex hierarchical microstructure. Therefore, the porosity factor has to be considered in the study of this

type of sample. Efforts to characterize these properties will drive the development of new generation nanoindentation testing procedure and facilities. As a consequence, there is still a need for the developments in this area in order to obtain more reliable, repeatable mechanical properties of these complex materials.

References

- [1] Yoshida, F., Uemori, T., & Fujiwara, K. (2002). Elastic–plastic behavior of steel sheets under in-plane cyclic tension–compression at large strain. *International Journal of Plasticity*, 18(5), 633-659.
- [2] Ilie, N., & Hickel, R. (2009). Macro-, micro-and nano-mechanical investigations on silorane and methacrylate-based composites. *Dental Materials*, 25(6), 810-819.
- [3] Monaghan, J. J. (2000). SPH without a tensile instability. *Journal of Computational Physics*, 159(2), 290-311
- [4] Jämsä, T., Rho, J. Y., Fan, Z., MacKay, C. A., Marks Jr, S. C., & Tuukkanen, J. (2002). Mechanical properties in long bones of rat osteopetrotic mutations. *Journal of Biomechanics*, 35(2), 161-165.
- [5] Cuy, J. L., Mann, A. B., Livi, K. J., Teaford, M. F., & Weihs, T. P. (2002). Nanoindentation mapping of the mechanical properties of human molar tooth enamel. *Archives of Oral Biology*, 47(4), 281-291.
- [6] Mann, A., & Dickinson, M. (2005). Nanomechanics, chemistry and structure at the enamel surface, 19, 105-131.
- [7] Jian, S. R., Chen, G. J., & Lin, T. C. (2010). Berkovich nanoindentation on AlN thin films. *Nanoscale Research Letters*, 5(6), 935-940.
- [8] Rao, M. D. (2003). Recent applications of viscoelastic damping for noise control in automobiles and commercial airplanes. *Journal of Sound and Vibration*, 262(3), 457-474.
- [9] Lewis, G. (2011). Viscoelastic properties of injectable bone cements for orthopaedic

- applications: State-of-the-art review. *Journal of Biomedical Materials Research Part B: Applied Biomaterials*, 98(1), 171-191.
- [10] Mathia, T. G., Pawlus, P., & Wieczorowski, M. (2011). Recent trends in surface metrology. *Wear*, 271(3), 494-508.
- [11] Fischer-Cripps, A. C. (2011). *Nanoindentation* (Vol. 1). Springer.
- [12] Ju, J. W. W., Chaboche, J. L., & Voyiadjis, G. Z. (Eds.). (1998). *Damage Mechanics in Engineering Materials*. Elsevier.
- [13] Guicciardi, S., Shimosono, T., & Pezzotti, G. (2006). Nanoindentation Characterization of Sub Micrometric Y TZP Ceramics. *Advanced Engineering Materials*, 8(10), 994-997.
- [14] Schuh, C. A. (2006). Nanoindentation studies of materials. *Materials Today*, 9(5), 32-40.
- [15] Bedoui, F., Sansoz, F., & Murthy, N. S. (2008). Incidence of nanoscale heterogeneity on the nanoindentation of a semicrystalline polymer: Experiments and modeling. *Acta Materialia*, 56(10), 2296-2306.
- [16] Karapanagiotis, I. (2007). An energetic criterion to compare the evolution of thermally-excited surface disturbances and nanoindentation-induced defects on thin polymer films. *Surface Science*, 601(16), 3426-3430.
- [17] Liao, Q., Huang, J., Zhu, T., Xiong, C., & Fang, J. (2010). A hybrid model to determine mechanical properties of soft polymers by nanoindentation. *Mechanics of Materials*, 42(12), 1043-1047.
- [18] Oyen, M. L., & Cook, R. F. (2009). A practical guide for analysis of nanoindentation data. *Journal of Mechanical Behavior of Biomedical Materials*, 2(4), 396-407.
- [19] Liu, X., & Gao, F. (2004). A novel multi-function tribological probe microscope

- for mapping surface properties. *Measurement Science and Technology*, 15(1), 91.
- [20] Liu, X. (2006). Correlation analysis of topography and its mechanical properties at micro and nanometre scales. *Tribology International*, (0301-679X).
- [21] Liu, X., Yue, Z., Cai, Z., Chetwynd, D. G., & Smith, S. T. (2008). Quantifying touch–feel perception: tribological aspects. *Measurement Science and Technology*, 19(8), 084007.
- [22] Mohs, F., *Grundriss der Mineralogie*. 1822, Dresden
- [23] Furuse, A. Y., Gordon, K., Rodrigues, F. P., Silikas, N., & Watts, D. C. (2008). Colour-stability and gloss-retention of silorane and dimethacrylate composites with accelerated aging. *Journal of Dentistry*, 36(11), 945-952.
- [24] Roylance, D. (2001). *Stress-strain curves*. Massachusetts Institute of Technology study, Cambridge.
- [25] *Handbook of nanoindentation with biological applications*[M]. Singapore: Pan Stanford, 2011
- [26] Fischer-Cripps, A. C. (2006). Critical review of analysis and interpretation of nanoindentation test data. *Surface and Coatings Technology*, 200(14), 4153-4165.
- [27] Bull, S. J. (2005). Nanoindentation of coatings. *Journal of Physics D: Applied Physics*, 38(24), R393.
- [28] Minor, A. M., Asif, S. S., Shan, Z., Stach, E. A., Cyrankowski, E., Wyrobek, T. J., & Warren, O. L. (2006). A new view of the onset of plasticity during the nanoindentation of aluminium. *Nature Materials*, 5(9), 697-702.
- [29] Domnich, V., Gogotsi, Y., & Dub, S. (2000). Effect of phase transformations on the shape of the unloading curve in the nanoindentation of silicon. *Applied*

Physics Letters, 76(16), 2214-2216.

- [30] Field, J. S., & Swain, M. V. (1993). A simple predictive model for spherical indentation. *Journal of Materials Research*, 8(02), 297-306.
- [31] Oliver, W. C., & Pharr, G. M. (1992). An improved technique for determining hardness and elastic modulus using load and displacement sensing indentation experiments. *Journal of Materials Research*, 7(06), 1564-1583.
- [32] Baxelevani, E. A., & Giannakopoulos, A. E. (2009). The modified Rockwell test: a new probe for mechanical properties of metals. *Experimental Mechanics*, 49(3), 371-382.
- [33] Oliver, W. C., & Pharr, G. M. (2004). Measurement of hardness and elastic modulus by instrumented indentation: Advances in understanding and refinements to methodology. *Journal of Materials Research*, 19(01), 3-20.
- [34] Cheng, L., Xia, X., Yu, W., Scriven, L. E., & Gerberich, W. W. (2000). Flat - punch indentation of viscoelastic material. *Journal of Polymer Science Part B: Polymer Physics*, 38(1), 10-22.
- [35] Cao, Y. P., & Lu, J. (2004). A new scheme for computational modeling of conical indentation in plastically graded materials. *Journal of Materials Research*, 19(06), 1703-1716.
- [36] Cheng, Y. T. (1999). Scaling relationships in conical indentation of elastic-perfectly plastic solids. *International Journal of Solids and Structures*, 36(8), 1231-1243.
- [37] Fischer-Cripps, A. C. (2006). Critical review of analysis and interpretation of nanoindentation test data. *Surface and Coatings Technology*, 200(14), 4153-4165.
- [38] Sneddon, I. N. (1965). The relation between load and penetration in the

- axisymmetric Boussinesq problem for a punch of arbitrary profile. *International Journal of Engineering Science*, 3(1), 47-57.
- [39] Van Vliet, K. J., Prchlik, L., & Smith, J. F. (2004). Direct measurement of indentation frame compliance. *Journal of Materials Research*, 19(01), 325-331.
- [40] Bolshakov, A., & Pharr, G. M. (1998). Influences of pileup on the measurement of mechanical properties by load and depth sensing indentation techniques. *Journal of Materials Research*, 13(04), 1049-1058.
- [41] Rabe, R., Breguet, J. M., Schwaller, P., Stauss, S., Haug, F. J., Patscheider, J., & Michler, J. (2004). Observation of fracture and plastic deformation during indentation and scratching inside the scanning electron microscope. *Thin Solid Films*, 469, 206-213.
- [42] Cheng, Y. T., & Cheng, C. M. (1998). Relationships between hardness, elastic modulus, and the work of indentation. *Applied Physics Letters*, 73(5), 614-616.
- [43] Pharr, G. M., Oliver, W. C., & Brotzen, F. R. (1992). On the generality of the relationship among contact stiffness, contact area, and elastic modulus during indentation. *Journal of Materials Research*, 7(03), 613-617.
- [44] Mittra, E., Akella, S., & Qin, Y. X. (2006). The effects of embedding material, loading rate and magnitude, and penetration depth in nanoindentation of trabecular bone. *Journal of Biomedical Materials Research Part A*, 79(1), 86-93.
- [45] Johnson, K. L. (1982). One hundred years of Hertz contact. *Proceedings of the Institution of Mechanical Engineers*, 196(1), 363-378.
- [46] Tymiak, N. I., Kramer, D. E., Bahr, D. F., Wyrobek, T. J., & Gerberich, W. W. (2001). Plastic strain and strain gradients at very small indentation depths. *Acta Materialia*, 49(6), 1021-1034.
- [47] Khademhosseini, A., Langer, R., Borenstein, J., & Vacanti, J. P. (2006).

- Microscale technologies for tissue engineering and biology. Proceedings of the National Academy of Sciences of the United States of America, 103(8), 2480-2487.
- [48] Choi, Y., Lee, H. S., & Kwon, D. (2004). Analysis of sharp-tip-indentation load–depth curve for contact area determination taking into account pile-up and sink-in effects. *Journal of Materials Research*, 19(11), 3307-3315.
- [49] Blau, P. J., & Shives, T. R. (1985). Microindentation Hardness Testing. ASTM (American Society for Testing Materials) Standardization News, 13(1), 47-51.
- [50] Oyen, M. L. (2006). Nanoindentation hardness of mineralized tissues. *Journal of Biomechanics*, 39(14), 2699-2702.
- [51] Doerner, M. F., & Nix, W. D. (1986). A method for interpreting the data from depth-sensing indentation instruments. *Journal of Materials Research*, 1(04), 601-609.
- [52] Asif, S. S., Colton, R. J., & Wahl, K. J. (2001,). Nanoscale surface mechanical property measurements: force modulation techniques applied to nanoindentation. In *ACS SYMPOSIUM SERIES* (Vol. 781, pp. 198-215). Washington, DC; American Chemical Society; 1999.
- [53] Sun, Y., Zheng, S., Bell, T., & Smith, J. (1999). Indenter tip radius and load frame compliance calibration using nanoindentation loading curves. *Philosophical Magazine Letters*, 79(9), 649-658.
- [54] VanLandingham, M. R. (2003). Review of instrumented indentation. *Journal of Research of the National Institute of Standards and Technology*, 108(4), 249-265.
- [55] Neuman, K. C., & Nagy, A. (2008). Single-molecule force spectroscopy: optical tweezers, magnetic tweezers and atomic force microscopy. *Nature Methods*, 5(6), 491.

- [56] Ushiki, T., Hitomi, J., Ogura, S., Umemoto, T., & Shigeno, M. (1996). Atomic force microscopy in histology and cytology. *Archives of Histology and Cytology*, 59(5), 421-431.
- [57] Ukraintsev, V. A., Baum, C., Zhang, G., & Hall, C. L. (2005, May). The role of AFM in semiconductor technology development: the 65 nm technology node and beyond. In *Metrology, Inspection, and Process Control for Microlithography*, (5752), 127-139.
- [58] Kranz, C., Friedbacher, G., Mizaikoff, B., Lugstein, A., Smoliner, J., & Bertagnolli, E. (2001). Integrating an ultramicroelectrode in an AFM cantilever: combined technology for enhanced information. *Analytical Chemistry*, 73(11), 2491-2500.
- [59] Silva, E. C. C. M., & Van Vliet, K. J. (2006). Robust approach to maximize the range and accuracy of force application in atomic force microscopes with nonlinear position-sensitive detectors. *Nanotechnology*, 17(21), 5525.
- [60] Ting, T. C. T. (1966). The contact stresses between a rigid indenter and a viscoelastic half-space. *Journal of Applied Mechanics*, 33(4), 845-854.
- [61] Golovin, Y. I. (2008). Nanoindentation and mechanical properties of solids in submicrovolumes, thin near-surface layers, and films: a review. *Physics of the Solid State*, 50(12), 2205-2236.
- [62] Hong, Y., Huber, A., Takanari, K., Amoroso, N. J., Hashizume, R., Badylak, S. F., & Wagner, W. R. (2011). Mechanical properties and in vivo behavior of a biodegradable synthetic polymer microfiber–extracellular matrix hydrogel biohybrid scaffold. *Biomaterials*, 32(13), 3387-3394.
- [63] Oyen, M. L., & Cook, R. F. (2003). Load–displacement behavior during sharp indentation of viscous–elastic–plastic materials. *Journal of Materials Research*, 18(01), 139-150.

- [64] Herbert, E. G., Oliver, W. C., & Pharr, G. M. (2008). Nanoindentation and the dynamic characterization of viscoelastic solids. *Journal of Physics D: Applied Physics*, 41(7), 074021.
- [65] Cohen, S. R., & Kalfon-Cohen, E. (2013). Dynamic nanoindentation by instrumented nanoindentation and force microscopy: a comparative review. *Beilstein Journal of Nanotechnology*, 4(1), 815-833.
- [66] Tweedie, C. A., & Van Vliet, K. J. (2006). Contact creep compliance of viscoelastic materials via nanoindentation. *Journal of Materials Research*, 21(06), 1576-1589.
- [67] Fang, T. H., & Chang, W. J. (2003). Nanomechanical properties of copper thin films on different substrates using the nanoindentation technique. *Microelectronic Engineering*, 65(1), 231-238.
- [68] Johnson, K. L. (1995). Contact mechanics and the wear of metals. *Wear*, 190(2), 162-170.
- [69] Fischer-Cripps, A. C. (2004). A simple phenomenological approach to nanoindentation creep. *Materials Science and Engineering: A*, 385(1), 74-82.
- [70] Fischer-Cripps, A. C. (2011). Time-dependent Nanoindentation. In *Nanoindentation*. Springer New York.
- [71] Cao, Y., Qian, X., & Huber, N. (2007). Spherical indentation into elastoplastic materials: Indentation-response based definitions of the representative strain. *Materials Science and Engineering: A*, 454, 1-13.
- [72] Hay, J., Agee, P., & Herbert, E. (2010). Continuous stiffness measurement during instrumented indentation testing. *Experimental Techniques*, 34(3), 86-94.
- [73] Fan, Z., & Rho, J. Y. (2003). Effects of viscoelasticity and time - dependent plasticity on nanoindentation measurements of human cortical bone. *Journal of*

Biomedical Materials Research Part A, 67(1), 208-214.

- [74] Shaw, M. T., & MacKnight, W. J. (2005). Introduction to polymer viscoelasticity. John Wiley & Sons.
- [75] Haj - Ali, R. M., & Muliana, A. H. (2004). Numerical finite element formulation of the Schapery non - linear viscoelastic material model. International Journal for Numerical Methods in Engineering, 59(1), 25-45.
- [76] Fischer-Cripps, A. C. (2006). Critical review of analysis and interpretation of nanoindentation test data. Surface and Coatings Technology, 200(14), 4153-4165.
- [77] Kim, J. J., Choi, Y., Suresh, S., & Argon, A. S. (2002). Nanocrystallization during nanoindentation of a bulk amorphous metal alloy at room temperature. Science, 295(5555), 654-657.
- [78] Hay, J., Agee, P., & Herbert, E. (2010). Continuous stiffness measurement during instrumented indentation testing. Experimental Techniques, 34, 86-94.
- [79] Menčík, J., He, L. H., & Němeček, J. (2011). Characterization of viscoelastic-plastic properties of solid polymers by instrumented indentation. Polymer Testing, 30(1), 101-109.
- [80] Cheng, Y. T., & Cheng, C. M. (2004). Scaling, dimensional analysis, and indentation measurements. Materials Science and Engineering: R: Reports, 44(4), 91-149.
- [81] Vandamme, M., & Ulm, F. J. (2006). Viscoelastic solutions for conical indentation. International Journal of Solids and Structures, 43(10), 3142-3165.
- [82] Odegard, G. M., Gates, T. S., & Herring, H. M. (2005). Characterization of viscoelastic properties of polymeric materials through nanoindentation. Experimental Mechanics, 45(2), 130-136.

- [83] Ebenstein, D. M., & Wahl, K. J. (2006). A comparison of JKR-based methods to analyze quasi-static and dynamic indentation force curves. *Journal of Colloid and Interface Science*, 298(2), 652-662.
- [84] Haney, E. J., & Subhash, G. (2011). Static and dynamic indentation response of basal and prism plane sapphire. *Journal of the European Ceramic Society*, 31(9), 1713-1721.
- [85] Jones, C. A., & Grasley, Z. C. (2011). Short-term creep of cement paste during nanoindentation. *Cement and Concrete Composites*, 33(1), 12-18.
- [86] Lee, E. H., & Radok, J. R. M. (1960). The contact problem for viscoelastic bodies. *Journal of Applied Mechanics*, 27(3), 438-444.
- [87] Wu, Z., Baker, T. A., Ovaert, T. C., & Niebur, G. L. (2011). The effect of holding time on nanoindentation measurements of creep in bone. *Journal of Biomechanics*, 44(6), 1066-1072.
- [88] Liu, X., Bell, T., Chetwynd, D. G., & Li, X. Y. (2003). Characterisation of engineered surfaces by a novel four-in-one tribological probe microscope. *Wear*, 255(1), 385-394.
- [89] Liu, X. (2013). Correlation analysis of surface topography and its mechanical properties at micro and nanometre scales. *Wear*, 305(1), 305-311.
- [90] Wang, L., & Liu, X. (2014). Characterization of viscoelastic materials by quasi-static and dynamic indentation. *Measurement Science and Technology*, 25(6), 064017.
- [91] Cheng, L., Xia, X., Scriven, L. E., & Gerberich, W. W. (2005). Spherical-tip indentation of viscoelastic material. *Mechanics of Materials*, 37(1), 213-226.
- [92] Chudoba, T., & Richter, F. (2001). Investigation of creep behaviour under load during indentation experiments and its influence on hardness and modulus

- results. *Surface and Coatings Technology*, 148(2), 191-198
- [93] Cheng, Y. T., & Cheng, C. M. (2005). Relationships between initial unloading slope, contact depth, and mechanical properties for conical indentation in linear viscoelastic solids. *Journal of Materials Research*, 20(04), 1046-1053.
- [94] Monserrat, O., & Crosetto, M. (2008). Deformation measurement using terrestrial laser scanning data and least squares 3D surface matching. *ISPRS Journal of Photogrammetry and Remote Sensing*, 63(1), 142-154.
- [95] Ralston, J., Larson, I., Rutland, M. W., Feiler, A. A., & Kleijn, M. (2005). Atomic force microscopy and direct surface force measurements (IUPAC technical report). *Pure and Applied Chemistry*, 77(12), 2149-2170.
- [96] Goddard, J. M., & Hotchkiss, J. H. (2007). Polymer surface modification for the attachment of bioactive compounds. *Progress in Polymer Science*, 32(7), 698-725.
- [97] Spori, D. M., Drobek, T., Zürcher, S., Ochsner, M., Sprecher, C., Mühlebach, A., & Spencer, N. D. (2008). Beyond the lotus effect: roughness influences on wetting over a wide surface-energy range. *Langmuir*, 24(10), 5411-5417.
- [98] Heidenau, F., Mittelmeier, W., Detsch, R., Haenle, M., Stenzel, F., Ziegler, G., & Gollwitzer, H. (2005). A novel antibacterial titania coating: metal ion toxicity and in vitro surface colonization. *Journal of Materials Science: Materials in Medicine*, 16(10), 883-888.
- [99] Krogman, K. C., Druffel, T., & Sunkara, M. K. (2005). Anti-reflective optical coatings incorporating nanoparticles. *Nanotechnology*, 16(7), S338.
- [100] Chawla, K., Lee, S., Lee, B. P., Dalsin, J. L., Messersmith, P. B., & Spencer, N. D. (2009). A novel low - friction surface for biomedical applications: Modification of poly (dimethylsiloxane) (PDMS) with polyethylene glycol

- (PEG)–DOPA–lysine. *Journal of Biomedical Materials Research Part A*, 90(3), 742-749.
- [101] Whitehouse, D. J. (2012). *Handbook of surface and nanometrology*. CRC press.
- [102] Assender, H., Bliznyuk, V., & Porfyrakis, K. (2002). How surface topography relates to materials' properties. *Science*, 297(5583), 973-976.
- [103] Bahr, D. F., & Vasquez, G. (2005). Effect of solid solution impurities on dislocation nucleation during nanoindentation. *Journal of Materials Research*, 20(08), 1947-1951.
- [104] Ellis, J. D., Smith, S. T., & Hocken, R. J. (2008). Alignment uncertainties in ideal indentation styli. *Precision Engineering*, 32(3), 207-214.
- [105] Xu, Z. H., & Li, X. (2007). Effect of sample tilt on nanoindentation behaviour of materials. *Philosophical Magazine*, 87(16), 2299-2312.
- [106] Kashani, M. S., & Madhavan, V. (2011). Analysis and correction of the effect of sample tilt on results of nanoindentation. *Acta Materialia*, 59(3), 883-895.
- [107] Liu, X., & Piotter, V. (2007). Mapping micro-mechanical properties of carbon-filled polymer composites by TPM. *Precision Engineering*, 31(2), 162-168.
- [108] ISO 14577-1. (2002). *Metallic materials-instrumented indentation test for hardness and materials parameters-Part 1: test method*.

Appendices

Appendix A Matlab program

A1 Hardness calculation

```
function hard2(xx);
%Plot the evaluated hardness measured by TPM(1000 points)for a series measurement.
%PID controll: hold the DPT steady and push the spring beam
%input the file name and the number of files

clear;
states=1;
filenum=0;
ccall=[];
ddall=[];
youngss=[];
hardnesss=[];

while states==1;
    k=menu('Please select from the following menu','Load Data','Plot All','3D images','Clear
all','save the data','Exit');

    if k==1;
        name=input('input file name','s');
        fid = fopen(name,'r');
        aname = fscanf(fid,'%g %g',[1 inf]); % It has two rows now.
        len=length(aname)
        number=len/2000
        base=1;
        for mm=1:number
            a=aname(base:base+999);    %Applied force
            b=aname(base+1000:base+1999);    %sensor output
            base=base+2000;
            b=-(b-max(b))*1000*1.5; %displacement in nanometer, if there is a amplifier used,
divided by its value
            a=(a-min(a))*20.1894; %change to force mN, -0.0 is the zero position voltage
            %stif=(mean(a(520:560))-mean(a(600:640)))/(mean(b(520:560))-mean(b(600:640)));
```



```

fmax=a(500);
hmax=mean(b(500:505));
jj=1;
    c(1)=0; %sensor output
    c(12)=mean(b(500:510));
    c(23)=mean(b(990:1000));
    d(1)=0; %force
    d(12)=a(500);
    d(23)=0;
    for i=2:11
        c(i)=mean(b(jj:jj+49));%displacement
        d(i)=mean(a(jj:jj+49));%force
        jj=jj+50;
    end
    jj=501;
    for i=13:22
        c(i)=mean(b(jj:jj+49));%displacement
        d(i)=mean(a(jj:jj+49));%force
        jj=jj+50;
    end
    if c(13)>c(12);
        c(12)=c(13);
    end
    %if c(14)>c(13);
    %    c(14)=c(13);
    %end

    %stifness calculation
    %differential method

    % stif=(mean(d(12:13))-mean(d(13:14)))/(mean(c(12:13))-mean(c(13:14)));

    %Lineer curve fitting method

    % stifit=polyfit(b(550:650),a(550:650),1);
    % stif=stifit(1,1);

    %test
AppForce=a;
Disp=b;
Order=3;
Section1 = 1:500;
Section2 = 550:1000;

```

```

M=[];
for i=Order:-1:0
    M=[M;AppForce.^i];
end
p1 = polyfit(AppForce(Section1),Disp(Section1), Order);
DD1 = p1 * M(:, Section1);

%plot(DD1, AppForce(Section1) );

p2 = polyfit( AppForce(Section2),Disp(Section2),Order);
DD2 = p2 * M(:, Section2);
plot(DD1, AppForce(Section1), DD2, AppForce(Section2) );
dp = p2(Order +1) - p1(Order +1);
%plot(DD1, AppForce(Section1), Disp(1:500), AppForce(1:500), '*',DD2, AppForce(Section2),
Disp(501:1000), AppForce(501:1000), '*' );
%plot(Disp(Section2), AppForce(Section2), '*', DD2, AppForce(Section2));
%plot(DD1, AppForce(Section1), Disp(Section1), AppForce(Section1),'.');
%pause
%stif1=1/p1(1,3)
f1=AppForce(Section1);
f2=AppForce(Section2);
%save temp a b c d DD1 DD2 f1 f2;
stif=(f2(30)-f2(180))/(DD2(30)-DD2(180))

plot(c,d,DD1,f1,DD2(30:180),f2(30:180))

pause
% keyboard
%Power fit method

%fa=a(501:1000);
%hb=b(501:1000);
%aa=fa/(hb-hb(500))^1.5;
%aa=sort(aa);
%aa=aa(10:490);
%aaf=mean(aa);
%stif=1.5*aaf*(ha(1)-hb(500))^0.5;

hc=hmax-0.75*fmax/stif;

area=25.4*hc*hc;
er=((sqrt(pi)*stif)/(sqrt(area)*2))*10^6;
%youngs=((1141*er)*(1-0.4*0.4))/((1141-(er*(1-0.07*0.07))))
youngs=er

```

```

hardness=(fmax/area)*10^6
youngss=[youngss youngs];
hardnesss=[hardnesss hardness];
ccall=[ccall c];
ddall=[ddall d];
clf

figure(2)

save 'h_file' c d;
%axes('FontSize',18);
plot(c,d,c,d,'*');
grid
ylabel('Applied Force (mN)');
xlabel('Indentation depth (nm)');
pause

%text(max(c)/4,3*max(a)/4,['Youngs Moddulus=',num2str(youngs),'GPa']);
%text(max(c)/4,2.7*max(a)/4,['Nano-hardness=',num2str(hardness),'GPa']);
%figure(2)
%axes('FontSize',18);
%plot(b,a);
%ylabel('Applied Force (mN)');
%xlabel('Indentation depth (nm)');
%text(max(c)/4,3*max(a)/4,['Youngs Moddulus=',num2str(youngs),'GPa']);
%text(max(c)/4,2.7*max(a)/4,['Nano-hardness=',num2str(hardness),'GPa']);
% pause

end
filenum=filenum+1;
fclose(fid)

elseif k==2
plot(ccall,ddall);
ylabel('Applied Force (mN)');
xlabel('Indentation depth (nm)');

elseif k==3
length1=length(hardnesss);
pp=sqrt(length1);
element=1;
for j=1:pp
for i=1:pp
hardnessf(j,i)=hardnesss(element);
youngsf(j,i)=youngss(element);

```

```

        element=element+1;
    end
end
save H_P hardnessf
save E_P youngsf
save displace ccall
save force ddall
figure(2);
surfl(hardnessf);
shading interp;
colormap(copper);
title('Hardness');
figure(3);
surfl(youngsf);
shading interp;
colormap(copper);
title('Youngs modulus');
%hardnessfs=sort(hardnessf);
%youngsfs=sort(youngsf);
average_hardness=mean(mean(hardnessf))
average_Youngs_modulus=mean(mean(youngsf))

elseif k==4
    clear;
    clf;
    states=1;
        filenum=0;
        ccall=[];
        ddall=[];

elseif k==5
length1=length(hardnesss);
pp=sqrt(length1);
element=1;
for j=1:pp
    for i=1:pp
        hardnessf(j,i)=hardnesss(element);
        youngsf(j,i)=youngss(element);
        element=element+1;
    end
end

fname=input('Input file name of Youngs modulus','s');
fwid = fopen(fname,'w');
```

```

count = fprintf(fwid,'%6.5f\t',youngsf);
%count=fwrite(fwid,youngsf,'%6.5f');
fclose(fwid);

fname=input('Input file name of hardness','s');
fwid = fopen(fname,'w');
count = fprintf(fwid,'%6.5f\t',hardnessf);
%count=fwrite(fwid,hardnessf,'%6.5f');
fclose(fwid);
elseif k==6
    %clf;
    states=0;
end
end

```

A2 Lag phase angle calculation

```

chn0=load('1depth0.25v1chn0.txt')
chn1=load('1depth0.25v1chn1.txt')
len=length(chn0)
x=0:1:(len-1)
x=x'
chn0=chn0-mean(chn0)
chn1=chn1-mean(chn1)
func_sin=@(a,t)a(1)*sin(2*pi*t/100+a(2))
A=lsqcurvefit(func_sin,[0,0],x,chn0)
B=lsqcurvefit(func_sin,[0,0],x,chn1)
z=abs(A(1))
ang=(A(2)-B(2))*180/pi

```

A3 Tilt angle effect

```

% tilt geometrical effect on indentation
k=[0 0 -1];
DEG=pi/180;
beta=65.03*DEG; % Berkovich angle or 65.27 modified
% seta_x=1*DEG;
%%%%%%%%%%%%%% ideal normal
indentation
seta_z=0;
d=1

```

```

for i=1:21
    for j=1:21
        seta_x=(i-11)*0.4*DEG;
        seta_y=(j-11)*0.4*DEG;
        % [seta_x,seta_y] = MESHGRID(-1*DEG:0.1*DEG:1*DEG,-1*DEG:0.1*DEG:1*DEG)
        Rz=[cos(seta_z) -sin(seta_z) 0; sin(seta_z) cos(seta_z) 0;0 0 1];
        Ry=[cos(seta_y) 0 sin(seta_y); 0 1 0;-sin(seta_y) 0 cos(seta_y)];
        Rx= [1 0 0;0 cos(seta_x) sin(seta_x); 0 -sin(seta_x) cos(seta_x)];
        R=Rx*Ry*Rz;
        % Borkervich indenter
        % for i=1:10
        %     d=i*0.1;
        P2=[2*d*tan(beta) 0 d]';
        P3=[-d*tan(beta) d*sqrt(3)*tan(beta) d]';
        P4=[-d*tan(beta) -d*sqrt(3)*tan(beta) d]';
        % %%
        e2=R*P2/norm(P2,2);c2=d/dot(e2,k);ep2=c2*e2;
        e3=R*P3/norm(P3,2);c3=d/dot(e3,k);ep3=c3*e3;
        e4=R*P4/norm(P4,2);c4=d/dot(e4,k);ep4=c4*e4;
        % boundary
        PB1=ep3-ep2;
        PB2=ep4-ep2;
        % real contact area
        A_pb(i,j)=0.5*norm(cross(PB1,PB2),2);
        A_cb(i,j)=0.5*(norm(cross(ep2,ep3),2)+norm(cross(ep3,ep4),2)+norm(cross(ep4,ep2),2))
        % A_pb_ideal=0.5*norm(cross(PB1,PB2),2);
    end
end
figure(1)
surf(-4:0.4:4,-4:0.4:4,100*(A_pb./A_pb(11,11)-1));
xlabel('deg');
ylabel('deg');
zlabel('% difference');
shading interp;
figure(2)
surf(-4:0.4:4,-4:0.4:4,100*(A_cb./A_cb(11,11)-1));
xlabel('deg');
ylabel('deg');
zlabel('% difference');
shading interp;

```

A4 Power spectrum density

```
function [f,pyy]=freq(y,fs) % y is the signal and fs is sample frequency
t= 1/fs *(0:41999);
yy1=detrend(y,1);
Fy=fft(yy1,1024);
pyy=Fy.*conj(Fy)/1024;
f=(0:511)/1024*fs;
subplot(221)
plot(t,yy1)
xlabel('Time sec')
ylabel('Signal')
grid
subplot(222)
plot(f(1:10),pyy(1:10));
xlabel('Frequency Hz')
ylabel('PSD')
grid
title('Power spectrum density');
subplot(223)
plot(f(1:100),pyy(1:100));
xlabel('Frequency Hz')
ylabel('PSD')
grid
title('Power spectrum density');
subplot(224)
plot(f(1:512),pyy(1:512));
xlabel('Frequency Hz')
ylabel('PSD')
grid
title('Power spectrum density');
```

Appendix B Abaqus .inp file

B1 Flat surface 0 degree simulation

```
*Heading
** Job name: 0angleconical2D Model name: Model-1
** Generated by: Abaqus/CAE 6.11-1
*Preprint, echo=NO, model=NO, history=NO, contact=NO
**
** PARTS
**
*Part, name=punch
*End Part
**
*Part, name=sample
*Node
    1, -1.67999995, -2.
    2, -1.67999995, 0.
    3, -2., 0.
    4, -2., -4.
    5, 2., -4.
    6, 2., 0.
    7, 1.67999995, 0.
    8, 1.67999995, -2.
    9, -0.280000001, 0.
    10, -0.280000001, -0.180000007
    11, 0.280000001, -0.180000007
    12, 0., 0.
    13, 0.280000001, 0.
    14, 1.12, 0.
    15, 1.12, -1.44000006
    16, -1.12, -1.44000006
    17, -1.12, 0.
    18, -0.560000002, 0.
    19, -0.560000002, -0.600000024
    20, 0.560000002, -0.600000024
    21, 0.560000002, 0.
    22, -1.67999995, -1.95000005
    23, -1.67999995, -1.89999998
    24, -1.67999995, -1.85000002
    ..., ..., ...
```


....,,

11016, 0.159364074, -0.990681767
11017, 0.145441458, -0.977305293
11018, 0.133505076, -0.8888852
11019, 0.301354617, -0.863363206
11020, -0.118643448, -0.977725863
11021, -0.178493574, -0.938807249
11022, 0.245500609, -0.947916985
11023, 0.188722849, -0.960199058
11024, -0.456055015, -0.940612793
11025, -0.387595206, -0.884503007
11026, -0.19762592, -0.924444973
11027, 0.261404127, -0.899779975
11028, -0.028120989, -0.866209388
11029, 0.171795011, -0.970719993
11030, -0.430581957, -0.943232179
11031, 0.308372855, -0.888691902
11032, 0.0922193751, -0.921252608
11033, 0.0350844674, -0.927633882
11034, -0.0810788423, -0.769903541
11035, -0.313560724, -0.827115774
11036, -0.337161481, -0.813385665
11037, -0.164775357, -0.917549074
11038, -0.30638203, -0.852098763
11039, -0.205372423, -0.891995132
11040, -0.117335528, -0.924260199
11041, -0.151282042, -0.895166099
11042, -0.0845969468, -0.798565984
11043, -0.0787216946, -0.884571433
11044, -0.151572973, -0.844696879
11045, -0.192129061, -0.878423154

*Element, type=CPE3

1, 1407, 1317, 1369
2, 2452, 2562, 2585
3, 1641, 810, 1604
4, 1729, 1767, 1697
5, 2579, 1571, 1450
6, 1648, 825, 1618
7, 2591, 2174, 2163
8, 2566, 2469, 2484
9, 991, 59, 60
10, 1119, 1023, 967
11, 1234, 1120, 1141

12, 1400, 1125, 1353
13, 1230, 1110, 1131
14, 1314, 786, 1130
15, 2511, 1318, 1374
16, 1313, 955, 1105
17, 1309, 2523, 778
18, 1645, 1607, 1635
19, 2556, 1749, 1704
20, 1756, 842, 1814
21, 1897, 2755, 1875
22, 1899, 1894, 834

8011, 10155, 8293, 10130
8012, 10131, 10115, 10083
8013, 10154, 10134, 10149
8014, 10077, 10039, 10035
8015, 10129, 8331, 10140
8016, 10422, 10166, 10187
8017, 10560, 10542, 10550
8018, 10648, 10687, 10575
8019, 10826, 10663, 10679
8020, 10716, 10708, 8551
8021, 10720, 8752, 8700
8022, 10723, 9227, 9326
8023, 10725, 10408, 10441
8024, 10511, 10351, 10414
8025, 10824, 9725, 9761
8026, 10855, 9660, 9692
8027, 10896, 10572, 10880
8028, 10914, 9573, 9710
8029, 10910, 10947, 9445
8030, 9867, 9610, 9623
8031, 10987, 9446, 9321
8032, 11029, 10031, 11023
8033, 9851, 9842, 9927

*Element, type=CPE4R

48, 1123, 1004, 1003, 1128
49, 45, 46, 1002, 982
50, 999, 786, 1124, 1000
51, 50, 51, 970, 998
52, 51, 52, 997, 970
53, 994, 985, 1125, 1135
54, 1135, 1125, 1400, 1406

55, 2514, 1314, 1130, 1122
 56, 68, 69, 1359, 1455
 57, 1136, 1310, 2515, 1127
 58, 1216, 1123, 1306, 2516
 59, 38, 39, 983, 1007
 60, 39, 40, 1006, 983
 61, 960, 775, 1106, 1008
 62, 984, 961, 32, 33
 63, 1232, 2519, 1109, 1142
 64, 1356, 2520, 1231, 1360
 65, 1413, 1378, 1227, 2501
 66, 1399, 1371, 1351, 1462
 67, 1298, 1149, 1300, 1350
 68, 1053, 282, 283, 1052
 69, 1386, 1443, 1321, 1346
 70, 1828, 1808, 1820, 1819
 71, 1887, 2717, 1908, 1917
 72, 876, 1986, 1970, 1934
 73, 2677, 2071, 2650, 2088
 74, 888, 2105, 2123, 2139
 75, 2172, 2183, 925, 2153
 76, 2368, 2373, 2377, 2447
 77, 2330, 2256, 2222, 946
 78, 125, 126, 2255, 2222
 79, 946, 2222, 2255, 2338
 80, 2223, 2253, 948, 2359
 81, 128, 129, 2253, 2223
 82, 2382, 2359, 948, 2426
 83, 2548, 922, 2196, 2320
 84, 893, 2146, 2133, 2118
 85, 2052, 858, 2048, 2125
 86, 1945, 2043, 1939, 1955
 87, 2736, 1771, 2730, 839
 88, 1652, 1650, 1617, 2628
 89, 1385, 1435, 1335, 1324
 90, 1083, 238, 239, 1082
 91, 1083, 1082, 1157, 1194
 92, 1079, 243, 244, 1078
 93, 1078, 1077, 1168, 1158
 94, 1238, 1252, 1172, 1167
 ..., ..., ..., ..., ...,
 ..., ..., ..., ..., ...,
 ..., ..., ..., ..., ...,
 10984, 9452, 10959, 10982, 10983

```

10985, 9485, 9417, 8213, 10925
10986, 9300, 10986, 10987, 9321
10987, 10989, 9472, 9387, 9368
10988, 10994, 9732, 9672, 9662
10989, 10995, 9732, 9893, 11018
10990, 10999, 9548, 11012, 9687
10991, 11004, 9983, 11022, 9975
10992, 9556, 9796, 9557, 10989
10993, 11013, 10981, 10094, 10043
10994, 11029, 10051, 11017, 11016
10995, 11019, 9881, 9811, 9860
10996, 9902, 11026, 11021, 11037
10997, 8272, 11005, 11021, 11026
10998, 8270, 9936, 11024, 11030
10999, 11025, 9966, 9971, 9937
11000, 9994, 9954, 9924, 11023
11001, 11009, 11013, 10073, 8290
11002, 11035, 11038, 9816, 11015
11003, 9902, 11037, 11041, 9794
11004, 9803, 11039, 11045, 9758
11005, 9896, 9925, 9892, 9840
11006, 11044, 9775, 9738, 9695
*Nset, nset=_PickedSet2, internal, generate
    1, 11045, 1
*Elset, elset=_PickedSet2, internal, generate
    1, 11006, 1
** Section: Section-1
*Solid Section, elset=_PickedSet2, material=al
,
*End Part
**
**
** ASSEMBLY
**
*Assembly, name=Assembly
**
*Instance, name=punch-1, part=punch
    0., -0.012233, 0.
*Node
    1, -4.29732747e-13, 0.012232624, 0.
*Nset, nset=punch-1-RefPt_, internal
1,
*Surface, type=SEGMENTS, name=Surf-punch
START, 1.7820130483763, 0.907980999479954

```

```

LINE, 0.0453990499735974, 0.023131971345501
CIRCL, -0.0453990499744411, 0.0231319713455669, 0., 0.112232623764338
LINE, -1.78201304837586, 0.907980999482535
*Rigid Body, ref node=punch-1-RefPt_, analytical surface=Surf-punch
*End Instance
**
*Instance, name=sample-1, part=sample
*End Instance
**
*Nset, nset=Set-rf, instance=punch-1
1,
*Nset, nset=_PickedSet9, internal, instance=sample-1
3, 4, 5, 6, 63, 64, 65, 66, 67, 68, 69, 70, 71, 72, 73, 74
75, 76, 77, 78, 79, 80, 81, 82, 83, 84, 85, 86, 87, 88, 89, 90
91, 92, 93, 94, 95, 96, 97, 98, 99, 100, 101, 141, 142, 143, 144, 145
146, 147, 148, 149, 150, 151, 152, 153, 154, 155, 156, 157, 158, 159, 160, 161
162, 163, 164, 165, 166, 167, 168, 169, 170, 171, 172, 173, 174, 175, 176, 177
178, 179
*Elset, elset=_PickedSet9, internal, instance=sample-1
56, 137, 146, 152, 159, 188, 190, 195, 206, 219, 227, 245, 247, 331,
456, 479
480, 482, 483, 484, 490, 492, 493, 498, 499, 520, 522, 527, 532, 533,
535, 537
844, 845, 849, 850, 922, 925, 928, 939, 975, 977, 978, 979, 980, 981,
983, 985
987, 988, 989, 990, 992, 994, 995, 996, 997, 998, 1004, 1031, 1044, 1045, 1046,
1092
1148, 1149, 1242, 1276, 1848, 1849, 1859, 1861, 1867, 1871, 1872, 1884, 1885, 1886, 1889,
1903
*Nset, nset=_PickedSet10, internal, instance=sample-1
4, 5, 102, 103, 104, 105, 106, 107, 108, 109, 110, 111, 112, 113, 114, 115
116, 117, 118, 119, 120, 121, 122, 123, 124, 125, 126, 127, 128, 129, 130, 131
132, 133, 134, 135, 136, 137, 138, 139, 140
*Elset, elset=_PickedSet10, internal, instance=sample-1
78, 81, 123, 125, 135, 147, 161, 163, 174, 176, 205, 429, 435, 452,
480, 499
501, 503, 505, 507, 509, 511, 513, 515, 517, 1852, 1854, 1862, 1865, 1866, 1873,
1874
1875, 1876, 1877, 1878, 1879, 1880, 1881, 1882
*Nset, nset=_PickedSet13, internal, instance=punch-1
1,
*Nset, nset=Set-sample, instance=sample-1
12,
*Elset, elset=_Surf-sample_S1, internal, instance=sample-1

```

457, 479, 3383, 3388, 3858, 4058, 4065, 4067, 5524, 8036, 8074, 8089, 8102, 8487, 8513, 8517

8522, 8569, 8570, 8695

*Elset, elset=_Surf-sample_S2, internal, instance=sample-1

520, 757, 3211, 3463, 3531, 3532, 3535, 4057, 4833, 5044, 5049, 5062, 5065, 5138, 5150, 5151

5156, 5160, 5604, 5656, 5658, 5659, 5661, 5675, 5678, 5720, 5725, 5729, 5731, 8238, 8260, 8263

8486, 8577, 8580, 8657, 8660, 8663, 8710

*Elset, elset=_Surf-sample_S4, internal, instance=sample-1

540, 2145, 2163, 2181, 2199, 2217, 2235, 2253, 2271, 2289, 2307, 2325, 2343, 2361, 2379, 2397

2415, 2433, 2451, 2469, 2487, 2505, 2523, 2541, 2559, 2577, 2595, 2613, 2631, 2649, 2667, 2685

2703, 2721, 2739, 2757, 2775, 2793, 2811, 2829, 2847, 2865, 2883, 2901, 2919, 2937, 2955, 2973

2991, 3009, 3027, 3045, 3063, 3081, 3099, 3117, 3135, 3199, 3534, 3545, 3859, 3860, 3898, 3899

3901, 4888, 5526, 5527, 5529, 5530, 5531, 5533, 5534, 5535, 5536, 5538, 5539, 5540, 5542, 5543

5544, 5545, 5546, 5559, 5616, 5617, 5618, 5620, 5623, 5625, 5626, 5627, 5628, 5629, 5630, 5631

5632, 5733, 8035, 8526, 8571, 8572, 8574, 8575, 8576, 8578, 8579, 8581, 8582, 8584, 8585, 8586

8587, 8588, 8716, 8720, 8725

*Elset, elset=_Surf-sample_S3, internal, instance=sample-1

1042, 3862, 4064, 5525, 8075, 8509, 8511, 8515, 8516, 8518, 8519, 8520, 8521, 8523, 8524, 8525

8653, 8692, 8699, 8703

*Surface, type=ELEMENT, name=Surf-sample

_Surf-sample_S1, S1

_Surf-sample_S2, S2

_Surf-sample_S4, S4

_Surf-sample_S3, S3

*End Assembly

*Amplitude, name=Amp-1

0.02,	0.,	0.,	0.1,	0.01,	0.2,
	0.3,	0.03			
	0.4,	0.04,	0.5,	0.05,	0.6,
0.06,	0.7,	0.07			
	0.8,	0.08,	0.9,	0.09,	1.,
0.1,	1.1,	0.11			
	1.2,	0.12,	1.3,	0.13,	1.4,
0.14,	1.5,	0.15			

	1.6,	0.16,	1.7,	0.17,	1.8,
0.18,	1.9,	0.19			
	2.,	0.2,	2.1,	0.19,	2.2,
0.18,	2.3,	0.17			
	2.4,	0.16,	2.5,	0.15,	2.6,
0.14,	2.7,	0.13			
	2.8,	0.12,	2.9,	0.11,	3.,
0.1,	3.1,	0.09			
	3.2,	0.08,	3.3,	0.07,	3.4,
0.06,	3.5,	0.05			
	3.6,	0.04,	3.7,	0.03,	3.8,
0.02,	3.9,	0.01			
	4.,	0.			

**

** MATERIALS

**

*Material, name=al

*Elastic

70000., 0.33

*Plastic

200.,0.

400.,1.

**

** INTERACTION PROPERTIES

**

*Surface Interaction, name=IntProp-1

1.,

*Friction

0.,

**

** BOUNDARY CONDITIONS

**

** Name: BC-1 Type: Displacement/Rotation

*Boundary

_PickedSet9, 1, 1

** Name: BC-2 Type: Symmetry/Antisymmetry/Encastre

*Boundary

_PickedSet10, ENCASTRE

**

** INTERACTIONS

**

** Interaction: Int-1

*Contact Pair, interaction=IntProp-1

Surf-sample, punch-1.Surf-punch

```

** -----
**
** STEP: load
**
** Step, name=load, nlgeom=YES, inc=1000
** Static
0.1, 4., 1e-06, 4.
**
** BOUNDARY CONDITIONS
**
** Name: BC-mov Type: Displacement/Rotation
** Boundary, amplitude=Amp-1
_PickedSet13, 1, 1
_PickedSet13, 2, 2, -1.
_PickedSet13, 6, 6
**
** OUTPUT REQUESTS
**
** Restart, write, frequency=0
**
** FIELD OUTPUT: F-Output-1
**
** Output, field
** Node Output
CF, RF, U
** Element Output, directions=YES
LE, PE, PEEQ, PEMAG, S
**
** HISTORY OUTPUT: H-Output-1
**
** Output, history
** Node Output, nset=Set-rf
RF2, RT, U2
**
** HISTORY OUTPUT: H-Output-2
**
** Node Output, nset=Set-sample
RF2, RT, U2
** End Step

```

B2 Sinusoidal surface 0 degree simulation

*Heading

** Job name: sinua2d0angle Model name: Model-0angle
 ** Generated by: Abaqus/CAE 6.11-1
 *Preprint, echo=NO, model=NO, history=NO, contact=NO
 **

** PARTS

**

*Part, name=sample

*Node

1,	31.0651569,	-0.503026247
2,	31.0651569,	-3.22112489
3,	31.0651569,	-4.
4,	50.,	-4.
.....,,
.....,,
23889,	17.2883377,	-3.50241446
23890,	18.2026596,	0.324501008
23891,	16.9471874,	-0.654968441
23892,	15.9789486,	-2.68934226
23893,	18.0883636,	-0.055514615
23894,	18.085659,	-1.62828267
23895,	18.3100605,	-3.43036842
23896,	18.1272602,	-3.30829382
23897,	17.8137264,	0.337456465
23898,	17.7648525,	0.0811711475
23899,	18.190279,	-2.92483807
23900,	18.0686646,	-3.15527034
23901,	18.1495953,	-0.99470216
23902,	18.0498161,	-1.24868655
23903,	17.8425865,	-1.3725363
23904,	18.133604,	-0.855044127
23905,	16.7688904,	-2.49462032
23906,	18.2525406,	-2.3034451
23907,	17.6105461,	-2.18623018
23908,	18.2521935,	-2.01639867
23909,	18.0420532,	-2.00241828
23910,	17.9928532,	-2.11745071
23911,	14.8662405,	-1.91968167
23912,	17.0329018,	-2.03987122
23913,	17.7860031,	-1.59779322
23914,	17.2948418,	-2.4234488

*Element, type=CPS3

1,	21, 883,	1
2,	882, 895,	871
3,	884,	1, 883

4, 900, 85, 884
 5, 891, 892, 802
 6, 884, 85, 1
 14147, 7650, 7775, 7774
 15713, 16022, 16029, 16028
 15714, 16185, 595, 596
 15715, 16376, 16409, 16375
 15716, 16440, 16406, 16276
 15717, 16192, 16392, 16369
 15718, 16319, 16318, 16317
 15719, 16427, 16439, 16296
 15720, 16471, 16316, 16476
 15721, 582, 16206, 581
 15722, 16393, 16264, 16387
 15723, 16457, 16279, 16261
 15724, 16473, 16287, 16272
 15725, 16463, 16285, 16448
 23162, 22342, 22379, 22378
 23579, 23769, 729, 728
 23580, 23794, 792, 18
 23581, 23795, 23787, 23788
 23582, 23876, 23874, 23867
 23583, 23782, 705, 704
 23584, 700, 23888, 701

*Element, type=CPS4R

7, 882, 871, 22, 23
 8, 897, 793, 799, 813
 9, 889, 802, 892, 890
 10, 77, 841, 843, 76
 11, 815, 817, 820, 818
 12, 24, 803, 882, 23
 13, 26, 796, 881, 25
 14, 30, 31, 898, 797
 15, 797, 800, 29, 30
 16, 32, 878, 898, 31
 17, 889, 37, 38, 802
 18, 39, 40, 794, 876
 19, 40, 41, 875, 794
 20, 38, 39, 876, 802
 21, 795, 875, 41, 42
 22, 872, 873, 44, 45
 23, 793, 2, 46, 799
 24, 3, 47, 799, 46
 25, 82, 842, 840, 81

26, 856, 855, 823, 824

..., ..., ..., ..., ..., ...

23750, 23810, 23842, 23879, 23892
23751, 23895, 23768, 727, 726
23752, 23896, 23881, 23777, 23900
23753, 23906, 23772, 23910, 23783
23754, 23883, 23775, 716, 715
23755, 754, 23897, 23890, 16
23756, 23801, 23898, 23897, 754
23757, 23786, 23781, 23902, 23903
23758, 23881, 23896, 23895, 23770
23759, 23898, 23792, 23890, 23897
23760, 23904, 23901, 23780, 23886
23761, 23787, 23798, 23901, 23904
23762, 23914, 23912, 23905, 23796
23763, 23772, 23908, 23909, 23910
23764, 23875, 23862, 23866, 23873

*Element, type=CPE4R

16061, 7, 191, 16610, 631
16062, 191, 190, 16611, 16610
16063, 190, 189, 16612, 16611
16064, 189, 188, 16613, 16612
16065, 188, 187, 16614, 16613
16066, 187, 186, 16615, 16614
16067, 186, 185, 16616, 16615
16068, 185, 184, 16617, 16616
16069, 184, 183, 16618, 16617
16070, 183, 182, 16619, 16618
16071, 182, 181, 16620, 16619
16072, 181, 180, 16621, 16620

17956, 16497, 18308, 18319, 16496
17957, 18308, 18309, 18320, 18319
17958, 18309, 18310, 18321, 18320
17959, 18310, 18311, 18322, 18321
17960, 18311, 18312, 18323, 18322
17961, 18312, 18313, 18324, 18323
17962, 18313, 18314, 18325, 18324
17963, 18314, 18315, 18326, 18325
17964, 18315, 18316, 18327, 18326
17965, 18316, 18317, 18328, 18327
17966, 18317, 18318, 18329, 18328
17967, 18318, 16606, 16607, 18329

17968, 16496, 18319, 18330, 16495
 17969, 18319, 18320, 18331, 18330
 17970, 18320, 18321, 18332, 18331
 17971, 18321, 18322, 18333, 18332
 17972, 18322, 18323, 18334, 18333
 17973, 18323, 18324, 18335, 18334
 17974, 18324, 18325, 18336, 18335
 17975, 18325, 18326, 18337, 18336
 17976, 18326, 18327, 18338, 18337
 17977, 18327, 18328, 18339, 18338
 17978, 18328, 18329, 18340, 18339
 17979, 18329, 16607, 16608, 18340
 17980, 16495, 18330, 18341, 16494
 17981, 18330, 18331, 18342, 18341
 17982, 18331, 18332, 18343, 18342
 17983, 18332, 18333, 18344, 18343
 17984, 18333, 18334, 18345, 18344
 17985, 18334, 18335, 18346, 18345
 17986, 18335, 18336, 18347, 18346
 17987, 18336, 18337, 18348, 18347
 17988, 18337, 18338, 18349, 18348
 17989, 18338, 18339, 18350, 18349
 17990, 18339, 18340, 18351, 18350
 17991, 18340, 16608, 16609, 18351
 17992, 16494, 18341, 619, 14
 17993, 18341, 18342, 618, 619
 17994, 18342, 18343, 617, 618
 17995, 18343, 18344, 616, 617
 17996, 18344, 18345, 615, 616
 17997, 18345, 18346, 614, 615
 17998, 18346, 18347, 613, 614
 17999, 18347, 18348, 612, 613
 18000, 18348, 18349, 611, 612
 18001, 18349, 18350, 610, 611
 18002, 18350, 18351, 609, 610
 18003, 18351, 16609, 13, 609
 *Element, type=CPE3
 18004, 18083, 18094, 18093
 *Nset, nset=_PickedSet2, internal, generate
 1, 23914, 1
 *Elset, elset=_PickedSet2, internal, generate
 1, 23764, 1
 ** Section: Section-1
 *Solid Section, elset=_PickedSet2, material=al

```

,
*End Part
**
*Part, name=tip
*End Part
**
**
** ASSEMBLY
**
*Assembly, name=Assembly
**
*Instance, name=sample-1, part=sample
*End Instance
**
*Instance, name=tip-1, part=tip
      25.,      0.,      0.
*Node
      1,      0.,      0.,      0.
*Nset, nset=tip-1-RefPt_, internal
1,
*Surface, type=SEGMENTS, name=Surf-tip
START, 1.88294108962408, 0.674190516846164
LINE,      0.,      0.
LINE, -1.88294108962408, 0.674190516846164
*Rigid Body, ref node=tip-1-RefPt_, analytical surface=Surf-tip
*End Instance
**
*Nset, nset=_PickedSet8, internal, instance=sample-1
4, 5, 19, 20, 65, 66, 67, 772, 773, 774
*Elset, elset=_PickedSet8, internal, instance=sample-1
41, 44, 114, 130, 23599, 23613, 23614, 23699
*Nset, nset=_PickedSet9, internal, instance=sample-1
3, 4, 12, 15, 18, 20, 47, 48, 49, 50, 51, 52, 53, 54, 55, 56
57, 58, 59, 60, 61, 62, 63, 64, 585, 586, 587, 588, 589, 590, 591, 592
593, 594, 595, 596, 663, 664, 665, 666, 667, 668, 669, 670, 671, 672, 673, 674
675, 676, 677, 678, 679, 680, 681, 682, 683, 684, 685, 686, 687, 688, 689, 690
691, 692, 693, 694, 695, 696, 697, 698, 699, 730, 731, 732, 733, 734, 735, 736
737, 738, 739, 740, 741, 775, 776, 777, 778, 779, 780, 781, 782, 783, 784, 785
786, 787, 788, 789, 790, 791, 792
*Elset, elset=_PickedSet9, internal, instance=sample-1
24, 27, 28, 29, 30, 31, 33, 34, 35, 36, 37, 38, 39, 41,
42, 84
100, 103, 112, 15714, 15727, 15732, 15733, 15734, 15736, 15738, 15739, 15762, 15763,
15765, 15807, 15987

```

23124, 23125, 23126, 23127, 23128, 23129, 23130, 23131, 23132, 23133, 23134, 23135, 23136,
 23137, 23138, 23139
 23140, 23141, 23142, 23143, 23144, 23145, 23146, 23147, 23148, 23149, 23150, 23151, 23152,
 23153, 23154, 23155
 23156, 23157, 23158, 23159, 23160, 23161, 23194, 23226, 23258, 23290, 23322, 23354, 23386,
 23418, 23450, 23482
 23514, 23546, 23578, 23580, 23585, 23597, 23598, 23600, 23602, 23604, 23607, 23614, 23615,
 23616, 23619, 23620
 23621, 23623, 23686, 23694, 23695, 23708
 *Nset, nset=_PickedSet10, internal, instance=tip-1
 1,
 *Elset, elset=_Surf-sample_S2, internal, instance=sample-1
 6, 43, 44, 120, 16875, 16923, 16971, 17019, 17067, 17115, 17163, 17211, 17259,
 17307, 17355, 17403
 17451,
 *Elset, elset=_Surf-sample_S4, internal, instance=sample-1
 10, 25, 40, 50, 98, 101, 102, 104, 105, 107, 108, 109, 110,
 111, 146, 149
 155, 161, 167, 173, 179, 185, 191, 197, 203, 209, 215, 221, 227,
 233, 239, 245
 251, 257, 263, 269, 275, 281, 287, 293, 299, 305, 311, 317, 323,
 329, 335, 341
 347, 353, 359, 365, 371, 377, 383, 389, 395, 401, 407, 413, 419,
 425, 431, 437
 443, 449, 455, 461, 467, 473, 479, 485, 491, 497, 503, 509, 515,
 521, 527, 533
 539, 545, 551, 557, 563, 569, 575, 581, 587, 593, 599, 605, 611,
 617, 623, 629
 635, 641, 647, 653, 659, 665, 671, 677, 683, 689, 695, 701, 707,
 713, 719, 725
 731, 737, 743, 749, 755, 761, 767, 773, 779, 785, 791, 797, 803,
 809, 815, 821
 827, 833, 839, 845, 851, 857, 863, 869, 875, 881, 887, 893, 899,
 14148, 14192, 14236
 14280, 14324, 14368, 14412, 14456, 14500, 14544, 14588, 14632, 14676, 15819, 23163, 23195,
 23227, 23259, 23291
 23323, 23355, 23387, 23419, 23451, 23483, 23515, 23547, 23755
 *Elset, elset=_Surf-sample_S1, internal, instance=sample-1
 15728, 15741, 15749, 15750, 15751, 15752, 15753, 15783, 15785, 15814, 15816, 23599, 23685,
 23713, 23721, 23723
 *Elset, elset=_Surf-sample_S3, internal, instance=sample-1
 15784, 23586, 23609, 23612, 23689, 23692, 23693, 23696, 23697, 23698, 23704, 23706, 23707,
 23709
 *Surface, type=ELEMENT, name=Surf-sample

```

_Surf-sample_S2, S2
_Surf-sample_S4, S4
_Surf-sample_S1, S1
_Surf-sample_S3, S3
*End Assembly
*Amplitude, name=Amp-1
    0.,      0.,      0.1,      0.01,      0.2,      0.02,
0.3,      0.03
    0.4,      0.04,      0.5,      0.05,      0.6,
0.06,      0.7,      0.07
    0.8,      0.08,      0.9,      0.09,      1.,      0.1,
1.1,      0.11
    1.2,      0.12,      1.3,      0.13,      1.4,
0.14,      1.5,      0.15
    1.6,      0.16,      1.7,      0.17,      1.8,
0.18,      1.9,      0.19
    2.,      0.2,      2.1,      0.19,      2.2,      0.18,
2.3,      0.17
    2.4,      0.16,      2.5,      0.15,      2.6,
0.14,      2.7,      0.13
    2.8,      0.12,      2.9,      0.11,      3.,      0.1,
3.1,      0.09
    3.2,      0.08,      3.3,      0.07,      3.4,
0.06,      3.5,      0.05
    3.6,      0.04,      3.7,      0.03,      3.8,
0.02,      3.9,      0.01
    4.,      0.
**
** MATERIALS
**
*Material, name=al
*Elastic
70000., 0.33
*Plastic
200.,0.
400.,1.
**
** INTERACTION PROPERTIES
**
*Surface Interaction, name=IntProp-1
1.,
*Friction
0.,
**

```

```

** BOUNDARY CONDITIONS
**
** Name: BC-1 Type: Displacement/Rotation
*Boundary
_PickedSet8, 1, 1
** Name: BC-2 Type: Displacement/Rotation
*Boundary
_PickedSet9, 2, 2
**
** INTERACTIONS
**
** Interaction: Int-1
*Contact Pair, interaction=IntProp-1
Surf-sample, tip-1.Surf-tip
** -----
**
** STEP: load
**
*Step, name=load, nlgeom=YES, inc=10000
*Static
0.1, 4., 4e-07, 4.
**
** BOUNDARY CONDITIONS
**
** Name: BC-3 Type: Displacement/Rotation
*Boundary, amplitude=Amp-1
_PickedSet10, 1, 1
_PickedSet10, 2, 2, -1.
_PickedSet10, 6, 6
**
** OUTPUT REQUESTS
**
*Restart, write, frequency=0
**
** FIELD OUTPUT: F-Output-1
**
*Output, field
*Node Output
RF, U
*Element Output, directions=YES
LE, PEEQ, S
*Contact Output
CNAREA,
*Output, history, frequency=0

```


*End Step

Appendix C Labview Program for creep indentation

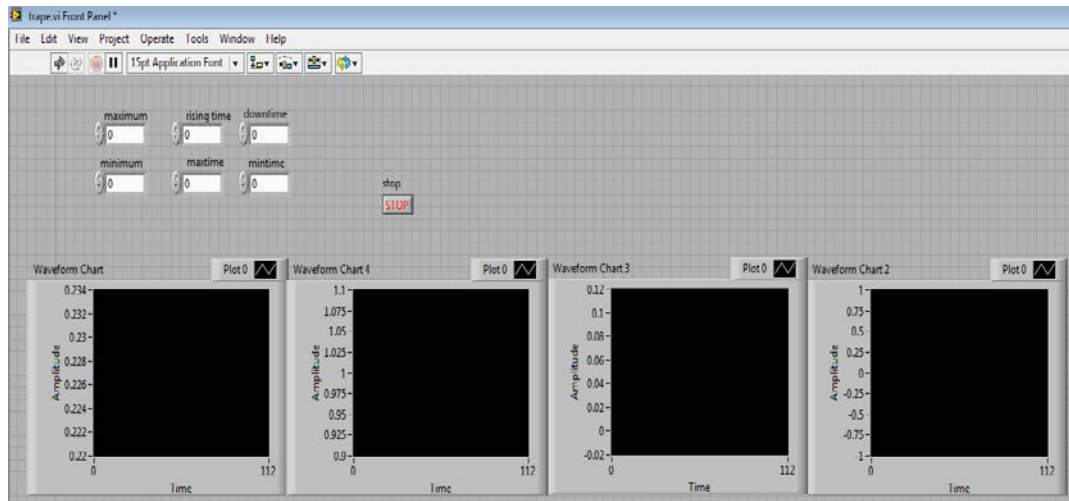


Figure C.1 Front panel of trapezoidal wave generation program

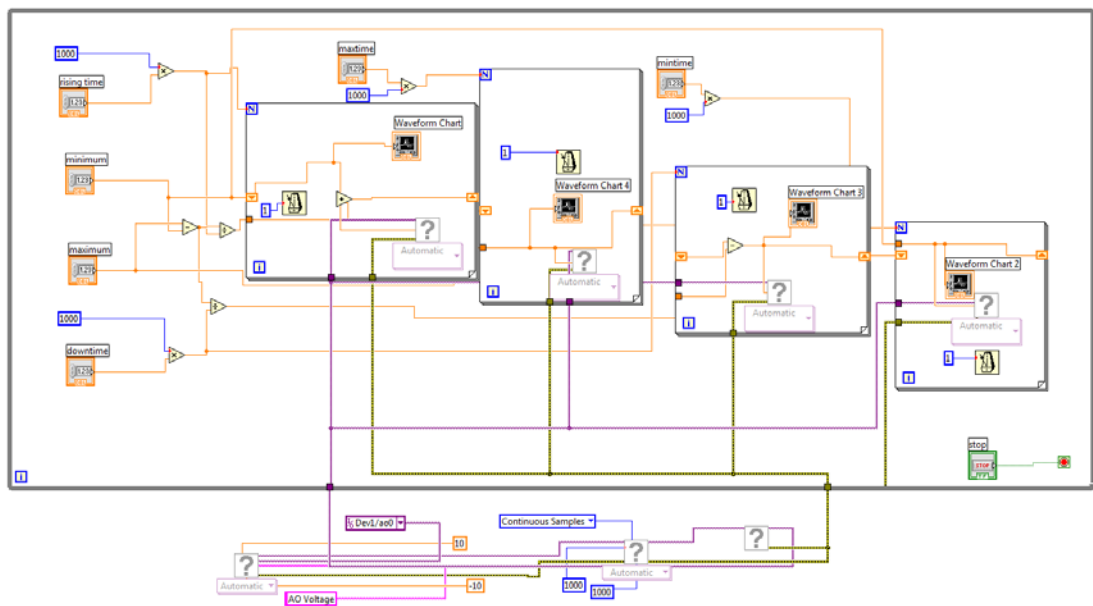


Figure C.2 Block diagram of trapezoidal wave generation program